Vibrationally resolved absorption, emission, resonance Raman and photoelectron spectra of selected organic molecules, associated radicals and cations: A time-dependent approach

von

Tao Xiong

June 2018

Univ.-Dissertation

zur Erlangung des akademischen Grades
"doctor rerum naturalium"
(Dr. rer. nat.)
in der Wissenschaftsdisziplin Theoretische Chemie

eingereicht an der
Mathematisch-Naturwissenschaftlichen Fakultät
Institut für Chemie
der Universität Potsdam

Published online at the
Institutional Repository of the University of Potsdam:
URN urn:nbn:de:kobv:517-opus4- 418105
http://nbn-resolving.de/urn:nbn:de:kobv:517-opus4- 418105

The studies described in this dissertation were conducted from March 2014 to June 2018 at the University of Potsdam under the supervision of Prof. Dr. Peter Saalfrank and Dr. Thomas Körzdörfer.

Abstract

Time-dependent correlation function based methods to study optical spectroscopy involving electronic transitions can be traced back to the work of Heller and coworkers. This intuitive methodology can be expected to be computationally efficient and is applied in the current work to study the vibronic absorption, emission, and resonance Raman spectra of selected organic molecules. Besides, the "non-standard" application of this approach to photoionization processes is also explored. The application section consists of four chapters as described below.

In Chapter 4, the molar absorptivities and vibronic absorption/emission spectra of perylene and several of its N-substituted derivatives are investigated. By systematically varying the number and position of N atoms, it is shown that the presence of nitrogen heteroatoms has a negligible effect on the molecular structure and geometric distortions upon electronic transitions, while spectral properties are more sensitive: In particular the number of N atoms is important while their position is less decisive. Thus, N-substitution can be used to fine-tune the optical properties of perylene-based molecules.

In Chapter 5, the same methods are applied to study the vibronic absorption/emission and resonance Raman spectra of a newly synthesized donor-acceptor type molecule. The simulated absorption/emission spectra agree fairly well with experimental data, with discrepancies being attributed to solvent effects. Possible modes which may dominate the fine-structure in the vibronic spectra are proposed by analyzing the correlation function with the aid of Raman and resonance Raman spectra.

In the next two chapters, besides the above types of spectra, the methods are extended to study photoelectron spectra of several small diamondoid-related systems (molecules, radicals, and cations). Comparison of the photoelectron spectra with available experimental data suggests that the correlation function based approach can describe ionization processes reasonably well. Some of these systems, cationic species in particular, exhibit somewhat peculiar optical behavior, which presents them as possible candidates for functional devices.

Correlation function based methods in a more general sense can be very versatile. In fact, besides the above radiative processes, formulas for non-radiative processes such as internal conversion have been derived in literature. Further implementation of the available methods is among our next goals.

Zusammenfassung

Molekülsysteme bestehen aus Kernen und Elektronen, deren viel kleinere Masse sie in die Lage versetzten, sich der Bewegung des ersteren augenblicklich anzupassen. Daher ist die Bewegung der Elektronen und Kerne in einer guten ersten Annäherung "unabhängig", und die Energie der Elektronen kann zuerst berechnet werden, vorausgesetzt, die Kerne sind stationär. Die so gewonnene elektronische Energie wird zur Abstoßungsenergie zwischen den Kernen addiert, um ein Potential zu erhalten, das die Bewegung der Kerne bestimmt.

Quantenmechanisch können sowohl die Elektronen als auch die Kerne nur bestimmte Energieniveaus haben. Die molekulare vibronische (= Schwingung + Elektronik) Absorptionsspektroskopie beinhaltet den Übergang der Elektronen und Kerne von ihrem Anfangs- in ihren Endzustand durch Photonenabsorption. Die größere elektronische Übergangsenergie bestimmt die Position des Absorptionsmaximums, während die kleinere nukleare Schwingungsübergangsenergie (ohne Berücksichtigung von Translation und Rotation) die Position der Teilmaxima innerhalb des Absorptionsbereichs bestimmt, wodurch die vibronische Feinstruktur entsteht. Ähnliche Ideen gelten auch für die vibronische Emissionsspektroskopie.

Die Resonanz-Raman-Spektroskopie untersucht die Energieänderung des einfallenden Photons (dessen Energie ausreichend ist, um die Elektronen in einen höheren elektronischen Zustand anzuregen), nachdem es mit dem Molekül wechselwirkt. Der Energiegewinn oder -verlust des einfallenden Photons bewirkt eine Änderung des Schwingungszustandes.

Die Photoelektronenspektroskopie ist ähnlich wie die vibronische Absorption, benötigt aber in der Regel mehr Energie des einfallenden Photons, da neben der Anregung des Moleküls in einen höheren vibronischen Zustand zusätzliche Energie benötigt wird, um ein Elektron aus dem Molekül zu entfernen.

Diese spektroskopischen Techniken liefern wertvolle Informationen über die elektronische und nukleare Bewegung des Moleküls. Theoretisch können wir eine zeitabhängige Korrelationsfunktion verwenden, um die Spektren zu simulieren. Die Korrelationsfunktion für die Absorption ist beispielsweise eine Funktion der Zeit, deren Entwicklung Informationen über die elektronischen Energien und die nukleare Bewegung enthält. Um das Absorptionsspektrum in Form von Energie zu erhalten, wird ein mathematisches Verfahren, die so genannte Fourier-Transformation, auf die zeitabhängige Korrelationsfunktion angewendet, um ein energieabhängiges Spektrum zu erhalten.

Diese Methode wird auf ausgewählte organische Moleküle, darunter einige Radikale und Kationen, angewandt, um deren elektronisches und optisches Verhalten unter dem Einfluss von einfallendem Licht zu untersuchen und Einblicke in das Design neuer optoelektronischer Bauelemente zu gewinnen. Bei einigen Molekülen/Systemen wird die vibronische Feinstruktur durch Faktoren wie molekulare Zusammensetzung und Umgebung wie Lösungsmittel beeinflusst, was darauf hindeutet, dass diese Systeme zur Feinabstimmung der gewünschten Eigenschaften verwendet werden können. Für andere Systeme gibt es fast keine sichtbare vibronische Feinstruktur, was bedeutet, dass sich die nukleare Bewegung solcher Systeme im Allgemeinen von derjenigen der vorherigen Kategorie unterscheidet.

Contents

Chapter 1

Introduction

1.1 Vibrationally resolved spectroscopy involving two electronic states

Vibrationally resolved electronic absorption, emission, and resonance Raman (rR) spectra provide important information on the structure and dynamics of molecules. Methods to simulate them are available in both the time-independent and the time-dependent approaches. The former is based on Fermi's golden rule (for absorption and emission) and the Kramers-Heisenberg-Dirac (KHD) equation [1, 2] (for resonance Raman spectra), and boils down to the calculation of Franck-Condon (FC) factors (for absorption and emission spectra), and coupling matrix elements (for components of the transition dipole moment) between relevant vibrational states (for resonance Raman spectra). This approach is straightforward, but suffers from the problem of computational scaling with respect to molecular size. In the latter, developed by Heller and co-workers [3, 4] and referred to as the Heller formalism, the computation of the Franck-Condon factors is performed in the time domain by projecting the initial wave-packet to the final electronic state, propagating it with the final state nuclear Hamiltonian, and evaluating the overlap of the new wave-packet as a function of time with the initial wave-packet. This overlap, known as the time-dependent correlation function, can be Fourier transformed to generate the vibronic absorption and/or emission spectra. The Heller formalism can be expected to be more efficient for calculations involving medium-large sized molecules like biomolecules. If the potential energy surfaces for both electronic states are assumed to be harmonic, a set of vibrational normal modes for each state can be obtained. The way the two sets of normal modes are related distinguishes three models (Section 2.4.2). Resonance Raman spectroscopy involves the (resonant) excitation of a molecule from the electronic ground to a real electronically excited state and return to the ground state. Thus the signals of resonance Raman spectra can be enhanced by a factor of up to six orders of magnitude, compared with Raman spectra [5]. This allows for measurement of resonance Raman spectra with a much lower sample concentration. One such example is the detection and analysis of environmental pollutants using resonance Raman techniques [6].

Besides, resonance Raman spectroscopy usually selectively enhances Raman signals associated with chromophores in the analyte, and is thus particularly useful for the analysis of large biomolecules [7]. Photoelectron spectroscopy (PES) involves ionization of a molecule from its electronic ground state to the electronic ground or an electronically excited state of its cation, depending on the excitation energy. This process is similar to that of the absorption, with the difference being that the final state has one less electron. This leaves open the possibility of extending the Heller formalism for vibronic absorption to vibronic photoelectron spectroscopy.

The optical processes studied in this work are depicted in Fig. 1.1.

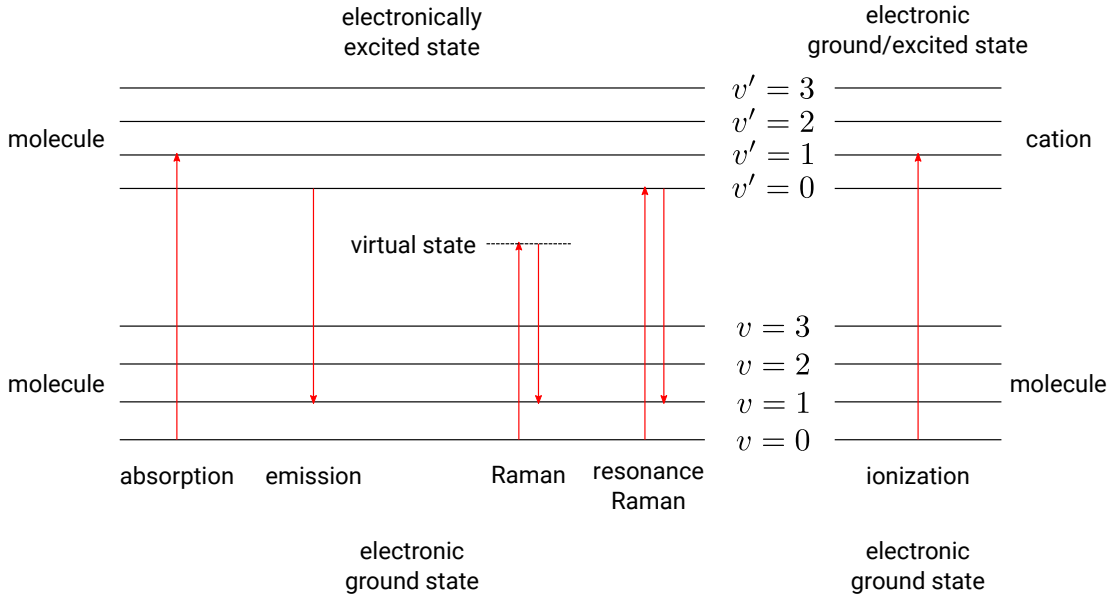

Figure 1.1: A schematic diagram of the vibronic absorption, emission, Raman, resonance Raman, and photoionization processes.

1.2 Objects of study in this work

Here we outline the topics to be covered in later chapters.

Chapter 2 lays the theoretical and computational foundation for each type of the spectroscopy mentioned above.

Chapter 3 explains the implementation of the models covered in Chapter 2 using our home-built program in combination with the quantum chemical package Gaussian 09

(G09) [8].

Chapter 4 focuses on the simulation of molar absorptivities, vibronic absorption and emission spectra of perylene and its N-substituted derivatives (azaperylenes). Spectral trends and features are discussed in reference to experimental data. An explanation of peculiarity for one azaperylene is proposed.

Chapter 5 applies the Heller formalism to simulate the vibronic absorption, emission, and resonance Raman spectra of [2](1,3)adamantano[2](2,7)pyrenophane, a medium-sized molecule consisting of the smallest diamondoid, adamantane, bridged to pyrene. The goal is to provide theoretical support for experimental observations and gain insight into the design of novel diamondoid-containing materials.

Chapter 6 extends the Heller formalism for vibronic absorption to study the photoelectron spectroscopy of a few lower diamondoids. The validity of this methodology will be evaluated by comparison of simulated with experimental spectra.

Chapter 7 studies the vibronic and resonance Raman spectra of two adamantane derivatives: 1-adamantyl and 2-adamantyl cations. Besides, the vibronic photoelectron spectra of the associated 1-adamantyl and 2-adamantyl radicals are calculated. Some spectra do not have experimental counterpart and can be used for predicative purposes.

Chapter 8 summarizes the work and proposes problems for future consideration.

The appendices contain additional formulas and data needed for the theories and discussions in the previous chapters.

Chapter 2

Theoretical and computational foundations

2.1 The molecular Schrödinger equation

In quantum mechanics, the state of a system is described by a wavefunction, which is a complex-valued function of the spatial and spin coordinates of the system and time. The wavefunction contains all the information about the dynamical observables and its absolute square is interpreted as the probability density of finding the system in a particular spatial and spin coordinate at a particular time. The fundamental dynamical equation for the wavefunction is the time-dependent Schrödinger equation [9]. When the potential energy of the system is independent of time, it is possible to factor out the time dependence of the wavefunction, where the time-independent part, the time-independent wavefunction, satisfies the time-independent Schrödinger equation.

From now on, we will work exclusively in atomic units, unless otherwise stated.

The time-independent molecular Schrödinger equation is

$$\hat{H}\Psi(\underline{r},\underline{R}) = E\Psi(\underline{r},\underline{R}), \tag{2.1}$$

where $\Psi(\underline{r},\underline{R})$ is the molecular wavefunction (with spin coordinates neglected for the moment), and E is the total energy of the molecule. The (column) vectors $\underline{r}$ and $\underline{R}$ stand for the spatial coordinates of the electrons and nuclei, respectively. The molecular Hamiltonian $\hat{H}$ can be written as

$$\hat{H} = -\frac{1}{2}\sum_{A=1}^{N}\frac{1}{M_A}\Delta_A + \sum_{A=1}^{N}\sum_{B>A}^{N}\frac{Z_A Z_B}{R_{AB}} - \frac{1}{2}\sum_{i=1}^{n}\Delta_i + \sum_{i=1}^{n}\sum_{j>i}^{n}\frac{1}{r_{ij}} - \sum_{A=1}^{N}\sum_{i=1}^{n}\frac{Z_A}{r_{iA}}, \tag{2.2}$$

where M is for nuclear mass, Z represents nuclear charge, A and B are nuclear indices, i and j label electrons, r and R are distances between particles specified by the associated indices, and n and N are the number of electrons and nuclei of the molecule, respectively. The spatial coordinates of electrons and nuclei will be denoted by lower and upper case letters, respectively. Thus the Laplacians for a nucleus A and an electron i are

$$\Delta_A = \frac{\partial^2}{\partial X_A^2} + \frac{\partial^2}{\partial Y_A^2} + \frac{\partial^2}{\partial Z_A^2} \tag{2.3}$$

and

$$\Delta_i = \frac{\partial^2}{\partial x_i^2} + \frac{\partial^2}{\partial y_i^2} + \frac{\partial^2}{\partial z_i^2}, \tag{2.4}$$

respectively. The five terms on the right hand side of Eq. (2.2) are operators for the kinetic energy of the nuclei ($\hat{T}_{\text{nuc}}$), inter-nuclear repulsion potential energy ($\hat{V}_{\text{NN}}$), kinetic energy of the electrons ($\hat{T}_{\text{el}}$), inter-electronic repulsion potential energy ($\hat{V}_{\text{ee}}$), and electron-nucleus attraction potential energy ($\hat{V}_{\text{eN}}$), respectively. The terms $\hat{T}_{\text{el}}$, $\hat{V}_{\text{ee}}$, and $\hat{V}_{\text{eN}}$ constitute the purely electronic Hamiltonian:

$$\hat{H}_{\text{el}} = -\frac{1}{2}\sum_{i=1}^{n}\Delta_i + \sum_{i=1}^{n}\sum_{j>i}^{n}\frac{1}{r_{ij}} - \sum_{A=1}^{N}\sum_{i=1}^{n}\frac{Z_A}{r_{iA}}. \tag{2.5}$$

Usually, the inter-nuclear repulsion term $\hat{V}_{\text{NN}}$ is added to $\hat{H}_{\text{el}}$, giving rise to the operator for the electronic Hamiltonian including nuclear repulsion:

$$\hat{H}_{\text{elec}} = \hat{H}_{\text{el}} + \hat{V}_{\text{NN}}. \tag{2.6}$$

The solution to Eq. (2.1) is greatly simplified by taking into account the fact that nuclei move much slower than electrons due to the much larger masses of the former. Thus the motion of electrons can be thought of as being in the field of a stationary nuclear frame, and the molecular wavefunction can be separated into a nuclear part and an electronic part. This is the basic idea of the Born-Oppenheimer approximation [10] and it will be used throughout this work.

Within the above approximation, Eq. (2.1) separates into the electronic Schrödinger equation

$$\hat{H}_{\text{elec}}\Psi_{\text{el}}(\underline{r};\underline{R}) = E_{\text{elec}}(\underline{R})\Psi_{\text{el}}(\underline{r};\underline{R}) \tag{2.7}$$

and the nuclear Schrödinger equation

$$[\hat{T}_{\text{nuc}} + E_{\text{elec}}(\underline{R})]\Psi_{\text{nuc}}(\underline{R}) = E\Psi_{\text{nuc}}(\underline{R}). \tag{2.8}$$

The electronic wavefunction $\Psi_{\text{el}}(\underline{r};\underline{R})$ depends parametrically on the nuclear coordinates, and the energy $E_{\text{elec}}(\underline{R})$ is the sum of the nuclear repulsion energy $V_{\text{NN}} = \hat{V}_{\text{NN}}$ and the purely electronic energy $E_{\text{el}}(\underline{R})$ which satisfies the purely electronic Schrödinger equation

$$\hat{H}_{\text{el}}\Psi_{\text{el}}(\underline{r};\underline{R}) = E_{\text{el}}(\underline{R})\Psi_{\text{el}}(\underline{r};\underline{R}). \tag{2.9}$$

Note that Eqs. (2.7) and (2.9) are equivalent in the sense that their solutions are the same, only that the corresponding eigenvalues differ by a constant V_{NN}. Since the nuclei move in the potential described by the function $E_{\mathrm{elec}}(\underline{R})$, it is known as the potential energy surface and will also be denoted $U(\underline{R})$. For each electronic state, there is a potential energy surface.

The solution of Eqs. (2.7) and (2.8) will be discussed in Sections 2.2 and 2.4, respectively.

2.2 Electronic structure theories [11]

2.2.1 Wavefunction based methods

The variational principle

Due to the complexity of the purely electronic Hamiltonian (Eq. (2.5)), the electronic Schrödinger equation can not be solved exactly in most problems of chemical interest. However, methods of finding approximate solutions in a systematic way exist. One such category is based on the variational principle, which states that the expectation value of energy for a system with a time-independent Hamiltonian $\hat{H}$ calculated from any well-behaved trial wavefunction Ψ_{trial} of spatial and spin coordinates is always greater than or equal to the true ground state energy E_0:

$$E_0 \leq E[\Psi_{\mathrm{trial}}] = \langle \Psi_{\mathrm{trial}} | \hat{H} | \Psi_{\mathrm{trial}} \rangle, \tag{2.10}$$

where $E[\Psi_{\mathrm{trial}}]$ is the variational energy calculated from the normalized trial wavefunction. An approximate wavefunction is typically found by devising a trial wavefunction dependent on some parameters and minimizing the variational energy functional with respect to the parameters.

Hartree-Fock theory

The starting point of almost all modern quantum chemical calculations based on the variational principle is the Hartree-Fock (HF) method [12, 13]. The trial ground state wavefunction is built as an (antisymmetrized) Slater determinant Ψ_{SD} from a set of n orthonormal one-electron spin-orbitals χ_i, each of which is a product of a spatial orbital ψ_i and a spin function (α or β):

$$\Psi_{\mathrm{trial}} = \Psi_{\mathrm{SD}} = \frac{1}{\sqrt{n!}} \begin{vmatrix} \chi_1(\underline{x}_1) & \chi_2(\underline{x}_1) & \cdots & \chi_n(\underline{x}_1) \\ \chi_1(\underline{x}_2) & \chi_2(\underline{x}_2) & \cdots & \chi_n(\underline{x}_2) \\ \vdots & \vdots & & \vdots \\ \chi_1(\underline{x}_n) & \chi_2(\underline{x}_n) & \cdots & \chi_n(\underline{x}_n) \end{vmatrix}. \tag{2.11}$$

Taking the spatial orbitals as the variational parameters, minimizing the energy leads to a set of one-electron equations known as the Hartree-Fock equations:

$$\hat{f}(1)\chi_i(1) = \varepsilon_i\chi_i(1), \tag{2.12}$$

where $\hat{f}(1)$ is the one-electron Fock operator, $\chi_i(1)$ is the i^{th} occupied HF orbital with orbital energy ε_i. The Fock operator is given as

$$\hat{f}(1) = \hat{h}^{\text{core}}(1) + \sum_{j=1}^{n}[\hat{J}_j(1) - \hat{K}_j(1)], \tag{2.13}$$

where the effective one-electron core Hamiltonian operator $\hat{h}^{\text{core}}(1)$ accounts for the kinetic energy and attraction of an electron to all the nuclei:

$$\hat{h}^{\text{core}}(1) = -\frac{1}{2}\Delta_1 - \sum_{A=1}^{N}\frac{Z_A}{r_{1A}}, \tag{2.14}$$

the Coulomb operator $\hat{J}_j(1)$ represents the classical Coulomb interaction energy of an electron with a charge distribution described by the spin-orbital $\chi_j(2)$:

$$\hat{J}_j(1) = \langle\chi_j(2)|\frac{1}{r_{12}}|\chi_j(2)\rangle, \tag{2.15}$$

and the exchange operator arising from the antisymmetry requirement of the electronic wavefunction is defined as

$$\hat{K}_j(1)\chi_i(1) = \langle\chi_j(2)|\frac{1}{r_{12}}|\chi_i(2)\rangle\chi_j(1). \tag{2.16}$$

The HF electronic energy is

$$E_{\text{el}}^{\text{HF}} = \langle\Psi_{\text{SD}}|\hat{H}_{\text{el}}|\Psi_{\text{SD}}\rangle = T_{\text{el}} + V_{\text{eN}} + J + E_{\text{x}}^{\text{HF}}, \tag{2.17}$$

where T_{el} and V_{eN} are the electronic kinetic energy and the potential energy of interaction between the electrons and the nuclei, respectively, and are related to the one-electron core Hamiltonian operators by

$$T_{\text{el}} + V_{\text{eN}} = \langle\Psi_{\text{SD}}|\sum_{i=1}^{n}\hat{h}^{\text{core}}(i)|\Psi_{\text{SD}}\rangle = \sum_{i=1}^{n}\langle\chi_i(1)|\hat{h}^{\text{core}}(1)|\chi_i(1)\rangle, \tag{2.18}$$

J is the classical Coulomb repulsion energy between the electrons:

$$J = \frac{1}{2}\sum_{i,j=1}^{n}\langle\chi_i(1)\chi_j(2)|\frac{1}{r_{12}}|\chi_i(1)\chi_j(2)\rangle, \tag{2.19}$$

and E_{x}^{HF} is the HF exchange energy:

$$E_{\text{x}}^{\text{HF}} = -\frac{1}{2}\sum_{i,j=1}^{n}\langle\chi_i(1)\chi_j(2)|\frac{1}{r_{12}}|\chi_j(1)\chi_i(2)\rangle. \tag{2.20}$$

Since the Fock operator depends on all the occupied orbitals to be solved for, the HF equations must be solved by a self-consistent field (SCF) method. Briefly, an initial guess of the set of orbitals is used to calculate the Fock operator and a new set of orbitals, which in turn are used in the next iteration to find a set of improved orbitals, and so on, until two consecutive sets of orbitals differ by less than a given threshold. In practice, the analytical HF equations are usually transformed to the so-called Roothaan equations that can be written in a matrix form, through introduction of a (finite) basis set (to be discussed below), and solved in the context of matrix algebra.

The HF theory is an independent-particle model. The inter-electronic interactions are considered only in an average way. In reality, motion of electrons is correlated in the sense that each electron's motion is affected by the instantaneous position of each other electron. The correlation energy, defined as the difference between the exact solution of the non-relativistic Schrödinger equation and the HF limit, can be recovered (at least partially) from various approaches collectively known as post-HF methods. These include [14]

1. Møller-Plesset perturbation (MP) theory: a non-variational method treating the correlation energy as a perturbation to the HF energy;

2. Configuration interaction (CI) method: a variational method in which the wavefunction is expressed as a linear combination of two or more Slater determinants ("configurations"), the coefficients being determined variationally;

3. Coupled-cluster (CC) theory: a non-variational method in which excited determinants are generated by a cluster operator, usually from the HF determinant.

Besides, the non-wavefunction based density functional theory (DFT) (Section 2.2.2) can handle the problem of correlation energy.

Basis sets

The spatial molecular orbitals used in the Slater determinant as well as in other contexts can conveniently be expressed as a linear combination of a chosen set of basis functions conventionally known as atomic orbitals (AOs), although they are not necessarily solutions to an atomic Schrödinger equation. A minimal basis set consists of one basis function for each core and valence AO of each atom. The size of a minimal basis set can be extended by replacing each basis function by two or three basis functions, leading to a double-zeta (DZ) or triple-zeta (TZ) basis set, respectively [15]. Even larger basis sets can be obtained similarly. The number of basis functions for each AO need not be the same. A split-valence (SV) basis set differs from a minimal basis set only in the number of basis functions used for valence AOs. In other words, an SV basis set is minimal for core AOs and double zeta or triple zeta (and so on) for valence AOs. Higher angular momentum functions known

as polarization functions can be added to the basis set to account for bonding more properly. Moreover, basis sets can be augmented with functions with small exponents known as diffuse functions to account for loosely bonded electrons in such systems as anions or excited states.

For electronic structure calculations, two types of basis functions are commonly used, namely Slater-type orbitals (STOs) [16] and Gaussian-type orbitals (GTOs). STOs have the advantage of bearing a greater resemblance to hydrogen-like orbitals, resulting in a better accuracy, while GTOs are more efficient for the manipulation of required integrals. A balance can be achieved by approximating each STO with a linear combination of k primitive GTOs, k typically being 3, a scheme known as STO-kG. This is an example of a Pople style (minimal) basis set. Another Pople's (split-valence double-zeta) basis set is denoted k-lmG, where the core orbitals are described by k primitive GTOs, and the inner and outer parts of the valence orbitals by l and m primitive GTOs, respectively [17]. Diffuse functions are denoted by + or ++ between m and G, and polarization functions by the number and type of functions added in brackets after G. The group of Ahlrichs have developed their own split-valence basis sets with such straightforward nomenclatures as TZV (Triple Zeta Valence) and TZVP (TZV with Polarization functions) [18].

In this work, the majority of calculations are performed with the TZVP basis set, which produces results of comparable quality to those produced by Pople's split valence triple-zeta polarized basis set 6-311G(d,p).

2.2.2 Density functional theory

The electronic wavefunction is a function of $3n$ spatial and n spin coordinates. Attempts have been made to replace it with a simpler quantity, the electron density, defined as

$$\rho(\underline{r}) = n \int |\Psi(\underline{x}, \underline{x}_2, ..., \underline{x}_n)|^2 \, d\sigma d\underline{x}_2 \cdots d\underline{x}_n, \tag{2.21}$$

where σ denotes the spin coordinate. The electron density is positive and normalized to n:

$$\rho(\underline{r}) \geq 0, \quad \int \rho(\underline{r}) \, d\underline{r} = n. \tag{2.22}$$

If the n-electron wavefunction is represented by a single Slater determinant constructed from a set of n orbitals ψ_i, the electron density is given by

$$\rho(\underline{r}) = \sum_{i=1}^{n} |\psi_i(\underline{r})|^2. \tag{2.23}$$

In density functional theory, the potential resulting from the nuclei is known as the external potential:

$$v_{\text{ext}}(\underline{r}) = -\sum_{A=1}^{N} \frac{Z_A}{|\underline{r} - \underline{R}_A|}. \tag{2.24}$$

The foundation of DFT is two theorems from Hohenberg and Kohn (HK) [19]. The first HK theorem states that the external potential is uniquely determined by the ground state electron density ρ_0. The ground state electronic energy E_0, therefore, is a functional of the ground state density:

$$E_0 = E[\rho_0]. \tag{2.25}$$

The second HK theorem guarantees that the energy obtained from a trial density satisfying condition (2.22) can not be lower than the true ground state electronic energy:

$$E_0 \leq E[\rho_{\text{trial}}]. \tag{2.26}$$

The ground state electronic energy functional can be separated into terms as

$$E[\rho] = T[\rho] + V_{\text{eN}}[\rho] + J[\rho] + E_{\text{xc}}[\rho]. \tag{2.27}$$

Although the second (electron-nucleus attraction energy) term $V_{\text{eN}}[\rho]$ and the third (classical Coulomb repulsion energy) term $J[\rho]$ are known to be

$$V_{\text{eN}}[\rho] = \int \rho(\underline{r}) v_{\text{ext}}(\underline{r})\, d\underline{r} \tag{2.28}$$

and

$$J[\rho] = \int \frac{\rho(\underline{r}_1)\rho(\underline{r}_2)}{r_{12}}\, d\underline{r}_1 d\underline{r}_2, \tag{2.29}$$

respectively, the first (kinetic energy) term $T[\rho]$ and the fourth (non-classical exchange-correlation energy) term $E_{\text{xc}}[\rho]$ are unknown, and finding approximate functionals of reasonably good quality for both (especially the kinetic energy) is a major challenge for orbital-free, pure DFT.

To overcome these difficulties, Kohn and Sham (KS) suggested an alternative method in which orbitals are reintroduced. Consider a hypothetical reference system of non-interacting electrons whose external potential $v_{\text{s}}(\underline{r})$ is chosen such that the ground state electron density $\rho_{\text{s}}(\underline{r})$ of the system is the same as the exact ground state electron density $\rho_0(\underline{r})$ of the molecule of interest. The Hamiltonian of the reference system is

$$\hat{H}_{\text{s}} = \sum_{i=1}^{n} \hat{h}_i^{\text{KS}}, \tag{2.30}$$

where the one-electron KS Hamiltonian $\hat{h}_i^{\text{KS}}$ is

$$\hat{h}_i^{\text{KS}} = -\frac{1}{2}\Delta_i + v_s(\underline{r}_i). \tag{2.31}$$

The n-electron KS wavefunction is a Slater determinant Ψ_{s} constructed from the n KS orbitals ψ_i^{KS} satisfying the KS equations:

$$\hat{h}^{\text{KS}}(1)\psi_i^{\text{KS}}(1) = \varepsilon_i^{\text{KS}}\psi_i^{\text{KS}}(1). \tag{2.32}$$

The electronic energy in the KS approach is expressed as

$$E[\rho] = T_{\rm s}[\rho] + V_{\rm eN}[\rho] + J[\rho] + E_{\rm xc}[\rho], \tag{2.33}$$

where the KS kinetic energy is

$$T_{\rm s}[\rho] = -\frac{1}{2}\langle\Psi_{\rm s}|\sum_{i=1}^{n}\Delta_i|\Psi_{\rm s}\rangle = -\frac{1}{2}\sum_{i=1}^{n}\langle\psi_i^{\rm KS}(1)|\Delta_1|\psi_i^{\rm KS}(1)\rangle. \tag{2.34}$$

Note that here the KS exchange-correlation functional $E_{\rm xc}[\rho]$ also includes the difference between the exact kinetic energy and the KS kinetic energy. Also note that the functional $E_{\rm xc}[\rho]$ can be expressed as the sum of an exchange-energy functional $E_{\rm x}[\rho]$ and a correlation-energy functional $E_{\rm c}[\rho]$:

$$E_{\rm xc}[\rho] = E_{\rm x}[\rho] + E_{\rm c}[\rho]. \tag{2.35}$$

In KS theory, the expression for $E_{\rm x}$ is the same as for the exchange energy $E_{\rm x}^{\rm HF}$ in the HF theory, except that the KS orbitals are used instead of the HF orbitals. Minimization of the KS electronic energy with respect to the KS orbitals leads to the following form of the KS potential:

$$v_{\rm s}(\underline{r}) = v_{\rm ext}(\underline{r}) + \frac{\delta J[\rho]}{\delta\rho} + v_{\rm xc}(\underline{r}), \tag{2.36}$$

where the KS exchange-correlation potential $v_{\rm xc}(\underline{r})$ is

$$v_{\rm xc}(\underline{r}) = \frac{\delta E_{\rm xc}[\rho]}{\delta\rho}. \tag{2.37}$$

Similar to the HF equations, the KS equations must be solved self-consistently.

In a sense, KS-DFT is all about making approximations to the unknown exchange-correlation functional. The simplest one in the hierarchy of approximation schemes is the local density approximation (LDA) [20, 21], where the functional $E_{\rm xc}^{\rm LDA}$ is derived from formulas for a uniform electron gas, and is dependent only on the density $\rho(\underline{r})$. Improvements can be obtained by using functionals which also depend on the gradients (the generalized gradient approximation, GGA) [22] and even higher order derivatives (meta-GGA) of $\rho(\underline{r})$.

Alternatively, hybrid exchange-correlation functionals mix HF-like exact exchange energies with DFT functionals. An example that is widely used in quantum chemistry is the B3LYP hybrid GGA functional

$$E_{\rm xc}^{\rm B3LYP} = (1-a)E_{\rm x}^{\rm LDA} + aE_{\rm x}^{\rm HF} + b(E_{\rm x}^{\rm B88} - E_{\rm x}^{\rm LDA}) + (1-c)E_{\rm c}^{\rm VWN} + cE_{\rm c}^{\rm LYP}, \tag{2.38}$$

where $a = 0.20$, $b = 0.72$, and $c = 0.81$. $E_{\rm x}^{\rm LDA}$ is the LDA exchange functional, $E_{\rm x}^{\rm HF}$ is the HF-like exact exchange functional calculated from KS orbitals, $E_{\rm x}^{\rm B88}$ is the Becke 88 exchange functional [23] in the generalized gradient approximation, $E_{\rm c}^{\rm VWN}$ is the VWN correlation functional of Vosko, Wilk, and Nusair [24] in the local density approximation, and $E_{\rm c}^{\rm LYP}$ is the correlation functional of Lee, Yang and Parr [25].

2.2.3 Time-dependent density functional theory

DFT based on the Hohenberg-Kohn theorems is a ground state theory and is generally not suitable for calculations involving excited states. For the purpose of obtaining excitation energies, a time-dependent version of DFT (TD-DFT) is developed, based on the Runge-Gross theorem (a counterpart for the first HK theorem) [26]. Briefly, this theorem states that there is a one-to-one correspondence between the set of all time-dependent external potentials $v_{\text{ext}}(\underline{r}, t)$ (up to a time-dependent function $c(t)$) and the set of time-dependent densities $\rho(\underline{r}, t)$. Moreover, an analogous principle to the second HK theorem exists, with the role played by the energy $E[\rho]$ replaced by the quantum mechanical action

$$A[\Psi] = \int \langle \Psi(t) | i\frac{\partial}{\partial t} - \hat{H}(t) | \Psi(t) \rangle \, dt. \tag{2.39}$$

Using the same technique of introducing a hypothetical reference system of non-interacting electrons as in the stationary KS theory, the time-dependent one-electron KS equations can be derived:

$$\hat{h}^{\text{KS}}(\underline{r}, t)\psi_i^{\text{KS}}(\underline{r}, t) = i\frac{\partial}{\partial t}\psi_i^{\text{KS}}(\underline{r}, t), \tag{2.40}$$

where the time-dependent one-electron KS Hamiltonian $\hat{h}^{\text{KS}}(\underline{r}, t)$ is

$$\hat{h}^{\text{KS}}(\underline{r}, t) = -\frac{1}{2}\Delta + v_{\text{s}}(\underline{r}, t). \tag{2.41}$$

Here, the time-dependent KS potential $v_{\text{s}}(\underline{r}, t)$ is similar to the stationary one (Eq. (2.36)):

$$v_{\text{s}}(\underline{r}, t) = v_{\text{ext}}(\underline{r}, t) + \frac{\delta J[\rho(t)]}{\delta \rho(t)} + v_{\text{xc}}(\underline{r}, t), \tag{2.42}$$

except that now the relevant quantities are time-dependent, and the time-dependent KS exchange-correlation potential $v_{\text{xc}}(\underline{r}, t)$ is

$$v_{\text{xc}}(\underline{r}, t) = \frac{\delta A_{\text{xc}}[\rho(\underline{r}, t)]}{\delta \rho(\underline{r}, t)}, \tag{2.43}$$

with $A_{\text{xc}}[\rho(\underline{r}, t)]$, the unknown exchange-correlation action functional, playing the role of $E_{\text{xc}}[\rho(\underline{r}, t)]$. Formally, $v_{\text{xc}}(\underline{r}, t)$ depends on the density $\rho(\underline{r}, t)$ as well as the initial wavefunction $\Psi_0(\underline{r}) := \Psi(\underline{r}, t_0)$. The latter dependence is usually neglected, however, within the adiabatic approximation, and $E_{\text{xc}}[\rho(\underline{r}, t)]$ is used instead of $A_{\text{xc}}[\rho(\underline{r}, t)]$:

$$v_{\text{xc}}(\underline{r}, t) \doteq \frac{\delta E_{\text{xc}}[\rho(\underline{r}, t)]}{\delta \rho(\underline{r}, t)}. \tag{2.44}$$

The exchange-correlation functionals used in the ground state KS-DFT are applicable in the time-dependent KS-DFT accordingly.

The excitation energies can be obtained in the linear response (LR) theory. The response of the time-dependent density $\rho(\underline{r},t)$ to a small time-dependent perturbation $\delta v(\underline{r},t)$ introduced by a weak time-dependent electric field is

$$\rho(\underline{r},t) = \rho_0(\underline{r}) + \int dt' \int d\underline{r}' \left.\frac{\delta\rho(\underline{r},t)}{\delta v(\underline{r}',t')}\right|_{v=v_0} \delta v(\underline{r}',t') + \cdots, \tag{2.45}$$

where $v_0(\underline{r})$ is the time-independent unperturbed potential, and $\rho_0(\underline{r})$ is the ground state density of the unperturbed system. The quantity

$$\chi(\underline{r},t;\underline{r}',t') := \left.\frac{\delta\rho(\underline{r},t)}{\delta v(\underline{r}',t')}\right|_{v=v_0} \tag{2.46}$$

is known as the time-dependent linear response function. Switching to the frequency space and introducing the dipole polarizability

$$\alpha_{ij}(\omega) = \int r_i \chi(\underline{r},\underline{r}',\omega) r_j \, d\underline{r} d\underline{r}', \tag{2.47}$$

where $r_i, r_j = x, y, z$ and $\chi(\underline{r},\underline{r}',\omega)$ is the frequency dependent linear response function, it can be shown that the poles of the mean polarizability $\bar{\alpha}(\omega)$ are the vertical excitation energies [27]

$$\omega_n = \Delta E_{\mathrm{vert},n} = E_n - E_0 \tag{2.48}$$

from the ground state to the n^{th} excited state with energy E_n, and the residues are the corresponding oscillator strengths

$$f_n = \frac{2}{3}\omega_n \mu_{n0}^2, \tag{2.49}$$

where μ_{n0} is the transition dipole moment (Eq. (2.86)) from the ground state to the n^{th} excited state.

By exploiting a fundamental relation between the linear response function and its Kohn-Sham version (which can be expressed in terms of KS orbitals) known as the Dyson equation of TD-DFT, one can show that the excitation energies are eigenvalues of the Casida's equations:

$$\begin{pmatrix} \underline{\underline{A}} & \underline{\underline{B}} \\ \underline{\underline{B}}^* & \underline{\underline{A}}^* \end{pmatrix} \begin{pmatrix} \underline{X} \\ \underline{Y} \end{pmatrix}_n = \Delta E_{\mathrm{vert},n} \begin{pmatrix} \underline{\underline{1}} & \underline{\underline{0}} \\ \underline{\underline{0}} & -\underline{\underline{1}} \end{pmatrix} \begin{pmatrix} \underline{X} \\ \underline{Y} \end{pmatrix}_n, \tag{2.50}$$

where (for global hybrid functionals)

$$\begin{aligned} A_{ar,bs} &= \delta_{ab}\delta_{rs}(\varepsilon_r - \varepsilon_a) + (ar|bs) - c_{\mathrm{HF}}(ab|rs) + (1 - c_{\mathrm{HF}})(ar|f_{\mathrm{xc}}|bs), \\ B_{ar,bs} &= (ar|sb) - c_{\mathrm{HF}}(as|rb) + (1 - c_{\mathrm{HF}})(ar|f_{\mathrm{xc}}|sb). \end{aligned} \tag{2.51}$$

Here, a, b are indices for occupied and r, s for unoccupied KS orbitals, c_{HF} is the contribution of exact exchange [28], and f_{xc} is the exchange-correlation kernel defined as

$$f_{\mathrm{xc}}(\underline{r},t;\underline{r}',t') = \frac{\delta v_{\mathrm{xc}}(\underline{r},t)}{\delta\rho(\underline{r}',t')}. \tag{2.52}$$

The Mulliken notation has been used for the two-electron integrals:

$$(ij|kl) = \int \psi_i^*(\underline{r})\psi_j(\underline{r})\frac{1}{|\underline{r}-\underline{r}'|}\psi_k(\underline{r}')\psi_l^*(\underline{r}')d\underline{r}d\underline{r}', \tag{2.53}$$

$$(ij|f_{\mathrm{xc}}|kl) = \int \psi_i^*(\underline{r})\psi_j(\underline{r})f_{\mathrm{xc}}(\underline{r},\underline{r}',\omega)\psi_k(\underline{r}')\psi_l^*(\underline{r}')d\underline{r}d\underline{r}', \tag{2.54}$$

where $f_{\mathrm{xc}}(\underline{r},\underline{r}',\omega)$ is the Fourier transform of the exchange-correlation kernel and is frequency-independent in the adiabatic approximation.

2.2.4 Solvent effects

In some cases, calculations for molecules are performed in solvents. Ideally, solvent effects should be dealt with by carrying out quantum-mechanical calculations on a solute molecule surrounded by a number of solvent molecules. This explicit solvent model, however, is usually impractical. A more popular way to include solvent effects is to use the polarizable continuum model (PCM), where the solvent is modeled as a polarizable continuous dielectric surrounding a cavity holding the solute, with the value of the dielectric constant determined by experiment [29]. The interaction of the solute molecule with the surrounding dielectric continuum, when treated quantum mechanically, serves as a perturbation term to the unperturbed Hamiltonian of the solute in vacuum, and the new Hamiltonian is used for subsequent calculations.

In this work, two variants of the PCM in the framework of TD-DFT are employed: the "ordinary" linear-response PCM (LR-PCM) [30, 31] gives the general order of vertical excitation energies for various excited states, and the state-specific PCM (SS-PCM) [32, 33] yields a more accurate excitation energy for a particular state of interest.

Equilibrium and non-equilibrium solvation

Before elaborating on the individual PCM methods, it is worthwhile to distinguish between two extreme regimes: the equilibrium solvation and the non-equilibrium solvation. In the former case, all the solvent degrees of freedom are in equilibrium with the solute electron density for the state under consideration. The dielectric constant of the solvent is the static dielectric constant ϵ. In the latter, only the fast degree of freedom, i.e. the electronic polarization, of the solvent is in equilibrium with the solute excited state electron density, whereas the slow degrees of freedom such as rotation of the solvent remain in equilibrium with the solute ground state electron density. This corresponds to a "fast" dielectric constant ϵ_f. In the case of photon absorption inducing electronic transitions, it is usually assumed that $\epsilon_f = \epsilon_{\mathrm{opt}} = n^2$, where ϵ_{opt} is called the dielectric constant at optical frequency, defined as the square of the solvent refractive index n [31].

Linear-response PCM [30, 31]

The electrostatic potential $\phi(\underline{r})$ generated by the solute polarizes the solvent dielectric outside the cavity. To a good approximation, the solvent reaction field can be modeled by an effective surface charge density $\sigma'(\underline{s})$, which can be expressed as

$$\sigma'(\underline{s}) = \int_\Gamma \tilde{\mathcal{Q}}(\underline{s}, \underline{s}')\phi(\underline{s}')\, d\underline{s}', \tag{2.55}$$

where $\underline{s}$ and $\underline{s}'$ are coordinate vectors of points on the surface Γ of the cavity, $\tilde{\mathcal{Q}}(\underline{s}, \underline{s}')$ is a response operator which is dependent on the solvent dielectric constant and the shape of the cavity. The solute-solvent interaction free energy can subsequently be computed as

$$G = \frac{1}{2}\int_\Gamma \int_\Gamma \phi(\underline{s})\mathcal{Q}(\underline{s}, \underline{s}')\phi(\underline{s}')\, d\underline{s}d\underline{s}', \tag{2.56}$$

where the operator $\mathcal{Q}(\underline{s}, \underline{s}')$ is related to $\tilde{\mathcal{Q}}(\underline{s}, \underline{s}')$ by

$$\mathcal{Q}(\underline{s}, \underline{s}') = \frac{1}{2}[\tilde{\mathcal{Q}}(\underline{s}, \underline{s}') + \tilde{\mathcal{Q}}(\underline{s}', \underline{s})]. \tag{2.57}$$

The solvation introduces a new term in the Kohn-Sham operator:

$$\hat{h}_{\mathrm{KS}} = \hat{h}^0_{\mathrm{KS}} + v^{\mathrm{PCM}}, \tag{2.58}$$

where $\hat{h}^0_{\mathrm{KS}}$ is the Kohn-Sham operator for the solute molecule in the gas phase, and the PCM operator v^{PCM} takes the following form:

$$v^{\mathrm{PCM}}(\underline{r}) = \frac{\delta G}{\delta \rho(\underline{r})} = \int_\Gamma \int_\Gamma \phi(\underline{s})\mathcal{Q}(\underline{s}, \underline{s}')\frac{1}{|\underline{s}' - \underline{r}|}\, d\underline{s}d\underline{s}'. \tag{2.59}$$

In the presence of a time-dependent external potential, one needs to solve the time-dependent Kohn-Sham equation (Eq. (2.40)), but now the KS operator has a PCM term as in Eq. (2.58) and all terms involved are time-dependent:

$$\hat{h}_{\mathrm{KS}}(\underline{r}, t) = \hat{h}^0_{\mathrm{KS}}(\underline{r}, t) + v^{\mathrm{PCM}}(\underline{r}, t). \tag{2.60}$$

It turns out that the PCM operator (when switching to the frequency domain) depends on the variation of the electron density:

$$v^{\mathrm{PCM}}[\delta\rho](\underline{r}) = \int_\Gamma \int_\Gamma \delta\phi(\underline{s}', \omega)\mathcal{Q}(\epsilon_{\mathrm{opt}}; \underline{s}', \underline{s})\frac{1}{|\underline{s} - \underline{r}|}\, d\underline{s}d\underline{s}', \tag{2.61}$$

in the regime of non-equilibrium solvation. In the case of equilibrium solvation, $\mathcal{Q}$ depends on the static dielectric constant ϵ instead of ϵ_{opt}. The term $\delta\phi(\underline{s}', \omega)$ in Eq. (2.61) is computed as

$$\delta\phi(\underline{s}', \omega) = \int \frac{\delta\rho(\underline{r}', \omega)}{|\underline{s}' - \underline{r}'|}\, d\underline{r}', \tag{2.62}$$

where the density variation is used instead of the electron density. The coupling matrix $\underline{\underline{K}}$ (used in Eqs. (2.68) and (2.69)) for an isolated solute molecule has elements

$$\begin{aligned}\underline{\underline{K}}^0_{st,uv} &= \iint \psi^*_s(\underline{r})\psi_t(\underline{r})\frac{1}{|\underline{r}-\underline{r}'|}\psi^*_u(\underline{r}')\psi_v(\underline{r}')\,d\underline{r}d\underline{r}' \\ &\quad + \iint \psi^*_s(\underline{r})\psi_t(\underline{r})\frac{\delta^2 E_{\rm xc}}{\delta\rho(\underline{r})\delta\rho(\underline{r}')}\psi^*_u(\underline{r}')\psi_v(\underline{r}')\,d\underline{r}d\underline{r}', \end{aligned} \tag{2.63}$$

where the ψ's are KS orbitals. For non-equilibrium solvation, the coupling matrix becomes

$$\underline{\underline{K}}_{st,uv} = \underline{\underline{K}}^0_{st,uv} + \int_\Gamma\int_\Gamma \phi_{st}(\underline{s}')\mathcal{Q}(\epsilon_{\rm opt};\underline{s}',\underline{s})\phi_{uv}(\underline{s})\,d\underline{s}'d\underline{s}, \tag{2.64}$$

where

$$\phi_{st}(\underline{s}) = -\int \psi^*_s(\underline{r})\frac{1}{|\underline{s}-\underline{r}|}\psi_t(\underline{r})\,d\underline{r}. \tag{2.65}$$

In the case of equilibrium solvation, $\epsilon_{\rm opt}$ in Eq. (2.64) should be replaced by the static dielectric constant ϵ. The electronic excitation energies can be shown to be the values of $\Delta E_{{\rm vert},n}$ which lead to zero eigenvalues of the matrix

$$\left[\begin{pmatrix} \underline{\underline{A}} & \underline{\underline{B}} \\ \underline{\underline{B}}^* & \underline{\underline{A}}^* \end{pmatrix} - \Delta E_{{\rm vert},n}\begin{pmatrix} \underline{\underline{1}} & \underline{\underline{0}} \\ \underline{\underline{0}} & -\underline{\underline{1}} \end{pmatrix}\right]\begin{pmatrix} \delta\underline{\underline{P}} \\ \delta\underline{\underline{P}}^* \end{pmatrix}, \tag{2.66}$$

where the matrix elements of $\delta\underline{\underline{P}}$ are given as coefficients in the following expansion in terms of the time-independent KS orbitals:

$$\delta\rho(\underline{r},\omega) = \sum_{st}\delta P_{st}(\omega)\psi_s(\underline{r})\psi_t(\underline{r}). \tag{2.67}$$

The elements of matrices $\underline{\underline{A}}$ and $\underline{\underline{B}}$ are

$$A_{ai,bj} = \delta_{ab}\delta_{ij}(\varepsilon_a - \varepsilon_i) + K_{ai,bj} \tag{2.68}$$

and

$$B_{ai,bj} = K_{ai,jb}, \tag{2.69}$$

respectively. Here, i,j indicate the occupied and a,b the unoccupied KS orbitals, ε's the orbital energies.

State-specific PCM [32, 33]

The SS-PCM differs from the LR-PCM in how the solvation free energy is computed. In the equilibrium case, the free energy is dependent on the excited state (2) density:

$$G^{(2)}_{\rm eq} = \frac{1}{2}\sum_i q^{(2)}_i V^{(2)}_{i,\rho} = \frac{1}{2}\sum_i q^{(2)}_{i,f} V^{(2)}_{i,\rho} + \frac{1}{2}\sum_i q^{(2)}_{i,s} V^{(2)}_{i,\rho}. \tag{2.70}$$

In the non-equilibrium case, the free energy is dependent on both the excited state (2) and the ground state (1) densities:

$$\begin{aligned} G^{(2)}_{\text{neq}} &= \frac{1}{2}\sum_i q^{(2)}_{i,f} V^{(2)}_{i,\rho} + \left(\sum_i q^{(1)}_{i,s} V^{(2)}_{i,\rho} - \frac{1}{2}\sum_i q^{(1)}_{i,s} V^{(1)}_{i,\rho}\right) \\ &\quad + \frac{1}{2}\left(\sum_i q^{(1)}_{i,s} V^{(2)}_{i,f} - \sum_i q^{(1)}_{i,s} V^{(1)}_{i,f}\right). \end{aligned} \tag{2.71}$$

In Eqs. (2.70) and (2.71), we have used summations instead of integrations. This amounts to treating the polarization charges as point charges located at various surface elements labeled by i, q_f/q_s are the polarization charges relative to the fast/slow degrees of freedom of the solvent, V_f/V_s are the corresponding potentials, and $V^{(n)}_\rho$ are the potentials generated by the electron density of the state (n).

The energies obtained from the above two equations can then be used to make corrections to the excited state energy from the TD-DFT calculation to compute the final equilibrium and non-equilibrium energies.

2.3 Vertical absorption spectra

The oscillator strengths f_n from Eq. (2.49) and vertical excitation energies ω_n from solution of Eq. (2.50) can be used to obtain a stick spectrum, which can further be broadened using a Lorentzian factor γ (half width at half maximum, HWHM) to account for homogeneous broadening according to

$$I = \sum_i \frac{f_i}{\pi} \frac{\gamma}{(\omega - \omega_i)^2 + \gamma^2}, \tag{2.72}$$

where I is the intensity for the broadened spectrum.

2.4 Vibronic spectroscopy

2.4.1 Normal mode analysis

For a bound state of a molecular system, the potential energy $U(\underline{R})$ attains its minimum at a particular (equilibrium) geometry which in the following will usually be denoted symbolically as (the subscript, superscript, etc., as appropriate) 0. Introducing the $3N \times 3N$ diagonal matrix $\sqrt{\underline{\underline{M}}}$ whose diagonal elements are the square roots of nuclear masses $\sqrt{M_1}$, $\sqrt{M_1}$, $\sqrt{M_1}$, $\sqrt{M_2}$, $\cdots$, $\sqrt{M_N}$, and defining the mass-weighted Cartesian displacement vector:

$$\underline{q} = \sqrt{\underline{\underline{M}}}(\underline{R} - \underline{R}_0), \tag{2.73}$$

the potential $U(\underline{R})$ becomes a function $U(\underline{q})$ of $\underline{q}$, where the same letter U has been used for simplicity. Expanding $U(\underline{q})$ in a Taylor series

$$U(\underline{q}) = U(\underline{0}) + \sum_{i=1}^{3N} \left(\frac{\partial U}{\partial q_i} \right)_{\underline{0}} q_i + \frac{1}{2} \sum_{i=1}^{3N} \sum_{j=1}^{3N} \left(\frac{\partial^2 U}{\partial q_i \partial q_j} \right)_{\underline{0}} q_i q_j + \cdots \tag{2.74}$$

at the equilibrium geometry $\underline{0} = \underline{q}_0$, setting the first partial derivatives to zero, and neglecting terms after the second partial derivatives, we obtain a potential with only quadratic terms (the harmonic oscillator approximation). The coefficients of the quadratic terms in Eq. (2.74) constitute the symmetric Hessian matrix $\underline{\underline{k}}$, whose eigenvectors (chosen to be orthogonal) are known as the normal modes and the corresponding eigenvalues λ_i satisfy $\sqrt{\lambda_i} = \omega_i$, where ω_i is the angular frequency with which the molecule oscillates in the i^{th} normal mode. Six (five for linear molecules, similar considerations apply hereafter) of the eigenvalues λ_i can be shown to be zero, corresponding to translation and rotation. Denote as $\underline{\underline{L}}$ the matrix consisting of the normal mode column vectors, the normal coordinate vector $\underline{Q}$ is defined as

$$\underline{Q} = \underline{\underline{L}}^{\mathrm{T}} \underline{q}, \tag{2.75}$$

where the superscript T means matrix transposition. In the following, however, we will use the symbol $\underline{\underline{L}}$ to refer to the $3N \times (3N-6)$ matrix with the six column vectors of $\underline{\underline{L}}$ for translation and rotation deleted. Correspondingly, the symbol $\underline{Q}$ will be a $3N-6$ dimensional vector for the vibrational normal coordinates.

The classical mechanical Hamiltonian for vibrations in normal coordinates takes the decoupled form:

$$H_{\mathrm{vib}} = \frac{1}{2} \sum_{m=1}^{3N-6} \left(\frac{dQ_m}{dt} \right)^2 + \frac{1}{2} \sum_{m=1}^{3N-6} \lambda_m Q_m^2, \tag{2.76}$$

where the potential reference has been chosen to be at the equilibrium geometry, i.e. $U(\underline{0})$ has been set to zero. The quantum mechanical Hamiltonian can therefore be constructed as

$$\hat{H}_{\mathrm{vib}} = \sum_{m=1}^{3N-6} \hat{H}_{\mathrm{vib}}^m, \tag{2.77}$$

where each one-dimensional operator $\hat{H}_{\mathrm{vib}}^m$ is

$$\hat{H}_{\mathrm{vib}}^m = -\frac{1}{2} \frac{\partial^2}{\partial Q_m^2} + \frac{1}{2} \omega_m^2 Q_m^2. \tag{2.78}$$

The eigenfunctions $\Phi_{\mathrm{vib}}(\underline{Q})$ of $\hat{H}_{\mathrm{vib}}$ are products of the form

$$\Phi_{\mathrm{vib}}(\underline{Q}) = \prod_{m=1}^{3N-6} \phi_v^m(Q_m), \tag{2.79}$$

where each one-dimensional wavefunction $\phi_v^m(Q_m)$ is an eigenfunction of the operator $\hat{H}_{\text{vib}}^m$ with eigenvalue

$$E_v^m = (v + \frac{1}{2})\omega_m, \quad v = 0, 1, 2, \ldots. \tag{2.80}$$

When the vibrational quantum number v for all modes are zero, the molecule has the lowest vibrational energy, the zero-point energy (ZPE).

2.4.2 Electronic absorption spectroscopy

Vibronic spectroscopy deals with transitions between two vibronic states, for which both the electronic and vibrational quantum numbers are involved. In the following, we will use upright letters i and f to refer to initial and final states, respectively. The subscripts el for Ψ_{el} and vib for Φ_{vib} will be dropped in this section for clarity.

The Duschinsky rotation

Since the normal coordinates $\underline{Q}^{\text{i}}$ and $\underline{Q}^{\text{f}}$ for the initial and final vibrational states (with their respective electronic states) are defined with respect to their respective equilibrium geometries $\underline{Q}_0^{\text{i}}$ and $\underline{Q}_0^{\text{f}}$ and in the context of their respective harmonic potentials, the way $\underline{Q}^{\text{i}}$ and $\underline{Q}^{\text{f}}$ are related is crucial in the further development of the theory of vibronic spectroscopy and gives rise to the following three models in increasing completeness.

In the independent mode displaced harmonic oscillator (IMDHO) model, it is assumed that the harmonic potential energy functions of the two electronic states take the same form, the only difference being the equilibrium geometries. Thus the normal modes and vibrational frequencies for both electronic states are the same, and the normal coordinates differ by a constant vector, corresponding to the two sets of normal coordinate axes being parallel.

In the IMDHOFA (IMDHO with frequency alteration) model, the normal mode analysis is performed for both electronic states, thus the vibrational frequencies of the initial and final electronic states are calculated explicitly, but the normal coordinate axes are still being assumed to be parallel.

In the IMDHOFAD (IMDHOFA with Duschinsky rotation) model, the above parallel axes assumption is dropped. The general expression for the relation between $\underline{Q}^{\text{i}}$ and $\underline{Q}^{\text{f}}$ is given by

$$\underline{Q}^{\text{f}} = \underline{\underline{J}}_{\text{f}\leftarrow\text{i}}\underline{Q}^{\text{i}} + \underline{\Delta}_{\text{f}\leftarrow\text{i}}, \tag{2.81}$$

where the $(3N-6)\times(3N-6)$ Duschinsky matrix $\underline{\underline{J}}_{\text{f}\leftarrow\text{i}}$ accounts for the rotation between the normal coordinate axes of the initial and final electronic states, and $\underline{\Delta}_{\text{f}\leftarrow\text{i}}$ represents

the shift between the coordinate origins. The subscript f ← i will usually be omitted if no confusion arises. The Duschinsky matrix $\underline{\underline{J}}_{\mathrm{f}\leftarrow\mathrm{i}}$ can be calculated as

$$\underline{\underline{J}}_{\mathrm{f}\leftarrow\mathrm{i}} = \underline{\underline{L}}_{\mathrm{f}}^{\mathrm{T}}\underline{\underline{L}}_{\mathrm{i}}, \tag{2.82}$$

and the origin shift vector $\underline{\Delta}_{\mathrm{f}\leftarrow\mathrm{i}}$ is expressed as

$$\underline{\Delta}_{\mathrm{f}\leftarrow\mathrm{i}} = \underline{\underline{L}}_{\mathrm{f}}^{\mathrm{T}}\sqrt{\underline{\underline{M}}}(\underline{R}_0^{\mathrm{i}} - \underline{R}_0^{\mathrm{f}}). \tag{2.83}$$

In some applications, we need to use the frequency-adapted dimensionless form of $\underline{\Delta}_{\mathrm{f}\leftarrow\mathrm{i}}$ defined as

$$\underline{\Delta}_{\mathrm{f}\leftarrow\mathrm{i}} = \frac{1}{\sqrt{\hbar}}\sqrt{\underline{\underline{\omega}}_{\mathrm{f}}}\underline{\underline{L}}_{\mathrm{f}}^{\mathrm{T}}\sqrt{\underline{\underline{M}}}(\underline{R}_0^{\mathrm{i}} - \underline{R}_0^{\mathrm{f}}), \tag{2.84}$$

where $\sqrt{\underline{\underline{\omega}}_{\mathrm{f}}}$ is a $(3N-6)\times(3N-6)$ diagonal matrix whose diagonal elements are the square roots of vibrational frequencies of the final electronic state. In this work the dimensionless form of the origin shift is used.

The time-independent approach

The transition probability between two vibronic states $\Psi_{\mathrm{i}}\Phi_{\mathrm{i}}$ and $\Psi_{\mathrm{f}}\Phi_{\mathrm{f}}$ induced by a photon is proportional to the absolute square of the transition moment

$$\underline{\mu}_{\mathrm{fi}} = \langle\Psi_{\mathrm{f}}\Phi_{\mathrm{f}}|\underline{\hat{\mu}}|\Psi_{\mathrm{i}}\Phi_{\mathrm{i}}\rangle = \langle\Phi_{\mathrm{f}}|\underline{\mu}_{\mathrm{el}}(\underline{Q})|\Phi_{\mathrm{i}}\rangle, \tag{2.85}$$

where $\underline{\hat{\mu}}$ is the electric dipole moment operator for the *molecule*, and the coordinate-dependent quantity

$$\underline{\mu}_{\mathrm{el}}(\underline{Q}) = \langle\Psi_{\mathrm{f}}|\underline{\hat{\mu}}_{\mathrm{el}}|\Psi_{\mathrm{i}}\rangle \tag{2.86}$$

will be referred to as the electric transition dipole moment. Note that $\underline{\hat{\mu}}_{\mathrm{el}}$ is the electric dipole moment operator for the *electrons*. To a first approximation, the coordinate dependence of the electric transition dipole moment $\underline{\mu}_{\mathrm{el}}(\underline{Q})$ can be ignored (the Condon approximation). Therefore, we can use its value at the initial state equilibrium geometry for relevant calculations. When this is done, Eq. (2.85) reduces to

$$\underline{\mu}_{\mathrm{fi}} = \underline{\mu}_{\mathrm{el}}(\underline{Q}_0^{\mathrm{i}})\langle\Phi_{\mathrm{f}}|\Phi_{\mathrm{i}}\rangle. \tag{2.87}$$

Note that Φ_{f} and Φ_{i} depend on normal coordinates of the initial and final states, respectively. Thus we can use any of the models, IMDHO, IMDHOFA, or IMDHOFAD as discussed before, to calculate the Franck-Condon factors $|\langle\Phi_{\mathrm{f}}|\Phi_{\mathrm{i}}\rangle|^2$.

In a one-dimensional case, Fermi's golden rule gives the absorption cross-section at $T = 0\,\mathrm{K}$ as

$$\sigma_{\mathrm{abs}} \propto \omega_{\mathrm{I}}|\underline{\mu}_{\mathrm{el}}(Q_0^{\mathrm{i}})|^2\sum_v |\langle\phi_v^{\mathrm{f}}(Q)|\phi_0^{\mathrm{i}}(Q)\rangle|^2\delta(\omega_{\mathrm{I}} - \omega_v), \tag{2.88}$$

where ω_{I} is the frequency of the incident photon.

The time-dependent approach

Now we need to transform Eq. (2.88) to a time-dependent form. This can be achieved by expressing the Dirac delta function as an integral and making use of the relation

$$\langle \phi_v^{\mathrm{f}}| \exp(-i\hat{H}_{\mathrm{f}}t) = \langle \phi_v^{\mathrm{f}}| \exp(-i\omega_v t), \tag{2.89}$$

where $\hat{H}_{\mathrm{f}}$ is the field-free nuclear Hamiltonian for the final electronic state. The final expression for the absorption cross-section is [4, 34]

$$\sigma_{\mathrm{abs}} = \frac{4\pi\omega_{\mathrm{I}}}{3c}|\underline{\mu}_{\mathrm{el}}(Q_0^{\mathrm{i}})|^2 \int_{-\infty}^{\infty} \langle \phi_0^{\mathrm{i}}|\phi_0^{\mathrm{i}}(t)\rangle \exp(i\omega_{\mathrm{I}}t)\, dt, \tag{2.90}$$

where c is the speed of light, and the quantity

$$\langle \phi_0^{\mathrm{i}}|\phi_0^{\mathrm{i}}(t)\rangle = \langle \phi_0^{\mathrm{i}}| \exp(-i\hat{H}_{\mathrm{f}}t)|\phi_0^{\mathrm{i}}\rangle \tag{2.91}$$

is known as the time-dependent absorption auto-correlation function. Taking the adiabatic minimum separation energy ΔE_{ad} and the zero-point energy $\omega_{\mathrm{Z}}^{\mathrm{i}}$ of the initial state into account, and also introducing a Lorentzian broadening factor Γ to simulate homogeneous spectral broadening, the expression for the absorption cross-section reads

$$\sigma_{\mathrm{abs}} = \frac{4\pi\omega_{\mathrm{I}}}{3c}|\underline{\mu}_{\mathrm{el}}(Q_0^{\mathrm{i}})|^2 \int_{-\infty}^{\infty} \langle \phi_0^{\mathrm{i}}|\phi_0^{\mathrm{i}}(t)\rangle \exp[i(\omega_{\mathrm{I}} - \Delta E_{\mathrm{ad}} + \omega_{\mathrm{Z}}^{\mathrm{i}})t] \exp(-\Gamma t)\, dt. \tag{2.92}$$

Relevant excitation energies, and different types of ionization potentials (IPs) for later reference, are defined in Fig. 2.1.

The generalization of the above expression to multidimensional, polyatomic cases is summarized in Appendix A.

2.4.3 Fluorescence emission spectroscopy

The treatment of fluorescence emission spectroscopy is similar to that of absorption, bearing in mind that the initial and final states have opposite orders of energy compared to those for absorption.

The time-independent approach

Making the same approximations as in the case of absorption, we have in a one-dimensional case, according to Fermi's golden rule, the emission cross-section

$$\sigma_{\mathrm{emi}} \propto \omega_{\mathrm{E}}^3 |\underline{\mu}_{\mathrm{el}}(Q_0^{\mathrm{i}})|^2 \sum_v |\langle \phi_v^{\mathrm{f}}(Q)|\phi_0^{\mathrm{i}}(Q)\rangle|^2 \delta(\omega_{\mathrm{E}} - \omega_v), \tag{2.93}$$

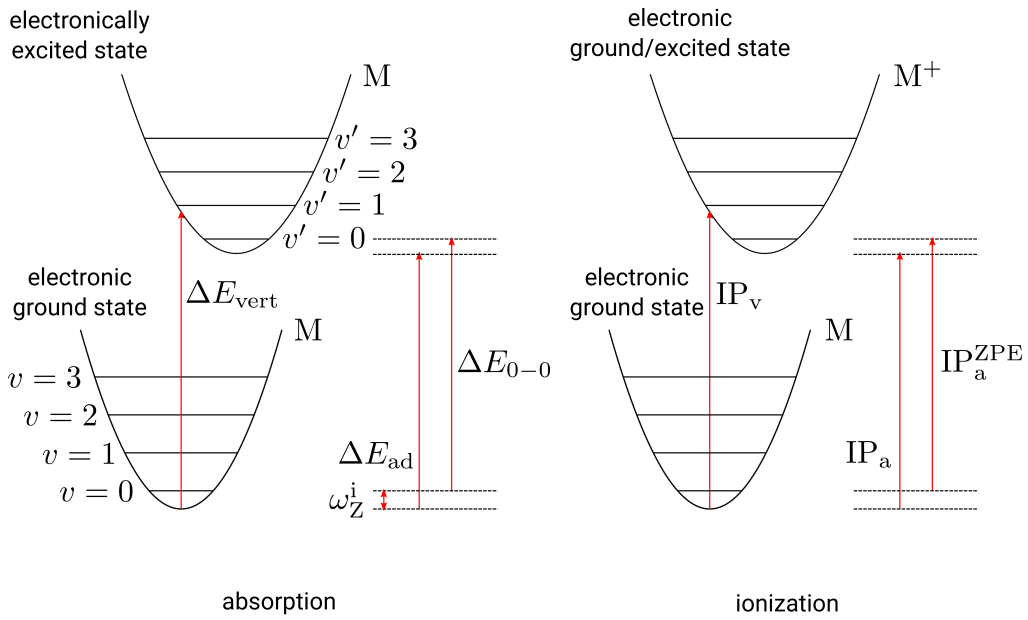

Figure 2.1: A schematic diagram of (left) the vibronic absorption process with definitions of relevant excitation energies and (right) the photoionization process with definitions of different types of ionization potentials. M stands for molecule, while M^+ means the corresponding cation.

where ω_{E} is the frequency of the emitted photon. It should be noted that, contrary to absorption, now the initial state i is the electronically excited state, and the final state f is the electronic ground state. Thus, ϕ_0^{i} is the vibrational ground state of the electronically excited state, and ϕ_v^{f} a vibrational state of the electronic ground state. The IMDHO, IMDHOFA, and IMDHOFAD models are also applicable in the evaluation of Frank-Condon factors in multidimensional cases.

The time-dependent approach

Following the same procedure as described in the time-dependent approach for absorption, an analogous equation to Eq. (2.92) for the emission cross-section in a one-dimensional case can be obtained:

$$\sigma_{\mathrm{emi}} = \frac{4\pi\omega_{\mathrm{E}}^3}{3c}|\underline{\mu}_{\mathrm{el}}(Q_0^{\mathrm{i}})|^2 \int_{-\infty}^{\infty} \langle\phi_0^{\mathrm{i}}|\phi_0^{\mathrm{i}}(t)\rangle \exp[i(\omega_{\mathrm{E}} + \Delta E_{\mathrm{ad}} + \omega_{\mathrm{Z}}^{\mathrm{i}})t] \exp(-\Gamma t)\, dt. \qquad (2.94)$$

Relevant quantities have similar meanings to those for absorption (Fig. 2.1), bearing in mind that now $\omega_{\mathrm{Z}}^{\mathrm{i}}$ is the ZPE of the electronically excited state.

The generalization of the above expression to multidimensional, polyatomic cases is summarized in Appendix A.

2.4.4 Resonance Raman spectroscopy

The time-independent approach

The discussion of Raman scattering is based on the KHD equation, which consists of a resonance term and a non-resonance term. Under resonance conditions, the resonance term dominates and the KHD equation for the polarizability components in a one-dimensional case at $T = 0\,\mathrm{K}$ is simplified to

$$\alpha^{qq'}_{f\leftarrow 0}(\omega_\mathrm{I}) = \sum_v \frac{\langle \phi^\mathrm{g}_f(Q)|\mu^q_\mathrm{el}(Q)|\phi^\mathrm{e}_v(Q)\rangle\langle\phi^\mathrm{e}_v(Q)|\mu^{q'}_\mathrm{el}(Q)|\phi^\mathrm{g}_0(Q)\rangle}{\omega_\mathrm{I} - \omega_v}, \tag{2.95}$$

where q and q' denote x, y, or z, ϕ^e_v is an (intermediary) vibrational state (with quantum number v) in the electronically excited state e to which the molecule may be excited, ϕ^g_f is the final vibrational state (with quantum number f) and ϕ^g_0 is the initial vibrational state (with quantum number $i = 0$ for $T = 0$ K) in the electronic ground state g. The resonance Raman cross-section $\sigma^\mathrm{rR}_{f\leftarrow 0}(\omega_\mathrm{I}, \omega_\mathrm{S})$ is obtained from the polarizability components:

$$\sigma^\mathrm{rR}_{f\leftarrow 0}(\omega_\mathrm{I}, \omega_\mathrm{S}) = \frac{8\pi\omega_\mathrm{I}\omega_\mathrm{S}^3}{9c^4} \sum_{q,q'} |\alpha^{qq'}_{f\leftarrow 0}(\omega_\mathrm{I})|^2, \tag{2.96}$$

where ω_S is the frequency of the scattered photon.

In this work, we will only consider the $1 \leftarrow 0$ resonance Raman scattering, i.e. $f = 1$.

The time-dependent approach

To obtain a time-dependent equation for the resonance Raman cross-section in a one-dimensional case, we proceed similarly as in Section 2.4.2. We apply the Condon approximation, rewrite Eq. (2.95) as an integral and use a similar relation to Eq. (2.89), then arrive at the desired equation

$$\alpha^{qq'}_{f\leftarrow 0}(\omega_\mathrm{I}) = \mu^q_\mathrm{el}(Q^\mathrm{i}_0)\mu^{q'}_\mathrm{el}(Q^\mathrm{i}_0) \int_0^\infty \langle \phi^\mathrm{g}_f|\phi^\mathrm{g}_0(t)\rangle \exp(i\omega_\mathrm{I}t)\, dt, \tag{2.97}$$

where the quantity

$$\langle \phi^\mathrm{g}_f|\phi^\mathrm{g}_0(t)\rangle = \langle \phi^\mathrm{g}_f| \exp(-i\hat{H}_\mathrm{e}t)|\phi^\mathrm{g}_0\rangle \tag{2.98}$$

is the time-dependent resonance Raman cross-correlation function. The operator $\hat{H}_\mathrm{e}$ is the field-free nuclear Hamiltonian for the electronically excited state. When the adiabatic minimum separation energy, zero-point energy of the initial state, and spectral broadening are taken into account, Eq. (2.97) becomes analogous to Eq. (2.92):

$$\alpha^{qq'}_{f\leftarrow 0}(\omega_\mathrm{I}) = \mu^q_\mathrm{el}(Q^\mathrm{i}_0)\mu^{q'}_\mathrm{el}(Q^\mathrm{i}_0) \int_0^\infty \langle \phi^\mathrm{g}_f|\phi^\mathrm{g}_0(t)\rangle \exp[i(\omega_\mathrm{I} - \Delta E_\mathrm{ad} + \omega^\mathrm{g}_\mathrm{Z})t] \exp(-\Gamma t)\, dt. \tag{2.99}$$

The generalization of the above expression to multidimensional, polyatomic cases is summarized in Appendix A.

In the multidimensional case, the resonance Raman cross-section depends on two variables, ω_I and ω_S (or effectively, ω_I and $\omega_\mathrm{I} - \omega_\mathrm{S}$), thus there are two ways to visualize it in a two-dimensional plot. We can plot $\sigma^{\mathrm{rR}}_{\mathrm{f}\leftarrow\mathrm{i}}(\omega_\mathrm{I}, \omega_\mathrm{S})$ as a function of the Raman shift $\omega_\mathrm{I} - \omega_\mathrm{S}$, keeping ω_I fixed. This gives a stick spectrum (which can be broadened using a different parameter $\tilde{\Gamma}$ from the one in Eq. (2.99)) of the resonance Raman intensities versus vibrational frequencies for the modes in the initial electronic state, i.e. the electronic ground state. Alternatively, we can fix $\omega_\mathrm{I} - \omega_\mathrm{S}$ corresponding to a particular mode and obtain a plot of resonance Raman intensities versus excitation frequencies ω_I, the so-called Raman excitaton profile (REP).

2.4.5 Photoelectron spectroscopy

Vibrationally resolved photoelectron spectroscopy can be treated in a similar fashion to vibronic absorption spectroscopy in the Heller formalism. For a neutral molecule ionized to the lowest electronic state of its cation, the initial state is the electronic ground state of the molecule, the final state is the electronic ground state of the cation, and the excitation energy is the corresponding ionization energy. The spectrum obtained corresponds to the lowest-energy PES band of the molecule. This approach neglects the kinetic-energy continuum of the emitted electron. It is further based on the harmonic and Born-Oppenheimer approximations. Higher bands can be treated similarly by taking relevant electronically excited states as the final states.

2.4.6 Calculation of accurate vertical ionization potentials

Related to the PES simulations, it is desirable to directly compare the simulated vertical ionization potential ($\mathrm{IP_v}$), which we calculate as the difference between the electronic SCF energies of cationic and neutral states at the optimized geometry of the neutral species, without ZPE corrections, with experimental data. The latter, however, is usually determined from the position of the 0-0 peak maximum in the experimental spectrum and should be interpreted as the ZPE-corrected adiabatic ionization potential ($\mathrm{IP_a^{ZPE}}$). For this purpose, we note that the adiabatic energy separation ΔE_ad between the neutral and cationic molecules can be used to determine the ZPE-corrected adiabatic ionization potential $\mathrm{IP_a^{ZPE}}$:

$$\mathrm{IP_a^{ZPE}} = \Delta E_\mathrm{ad} + \Delta\mathrm{ZPE} \quad . \tag{2.100}$$

Here, $\Delta\mathrm{ZPE} = \mathrm{ZPE}_+ - \mathrm{ZPE}_n$ is the difference between ZPEs of cationic (+) and neutral (n) molecules. The vertical ionization potential $\mathrm{IP_v}$, on the other hand, can be written as

$$\mathrm{IP_v} = \Delta E_\mathrm{ad} + E_\mathrm{rel} \tag{2.101}$$

where E_{rel} is the relaxation energy, obtained from the SCF energy difference between cationic state at the optimized geometry of the neutral species, and of the cation. Therefore, the following relation holds:

$$\mathrm{IP}_{\mathrm{a}}^{\mathrm{ZPE}} = \mathrm{IP}_{\mathrm{v}} - E_{\mathrm{rel}} + \Delta\mathrm{ZPE} \quad . \tag{2.102}$$

Depending on the approximation used for the exchange-correlation functional, Δ Kohn-Sham calculations of IPs can be prone to significant errors. Semilocal and standard global hybrid functionals, for example, typically underestimate vertical IPs by several tenths of an eV [35]. An alternative and supposedly more accurate approach to predict vertical IPs is provided by many-body perturbation theory (MBPT) in the GW approximation [36], where the self-energy Σ is approximated by the first term in its formal Taylor expansion in terms of the screened Coulomb interaction W, or symbolically,

$$\Sigma \doteq iGW, \tag{2.103}$$

where G is the one-particle Green's function. In principle, Σ should be computed iteratively until self-consistency is reached. However, owing to the high computational cost of fully or partially self-consistent GW, one mostly employs a non-self-consistent implementation, hereafter referred to as G_0W_0 [37], where the Green's function G and the screened interaction W are constructed from orbitals and eigenvalues obtained from Kohn-Sham DFT, and the quasiparticle energies $\varepsilon_i^{\mathrm{QP}}$ are obtained from a "one-shot" first-order correction to the KS eigenvalues $\varepsilon_i^{\mathrm{KS}}$:

$$\varepsilon_i^{\mathrm{QP}} = \varepsilon_i^{\mathrm{KS}} + \langle \psi_i^{\mathrm{KS}} | \Sigma(\varepsilon_i^{\mathrm{QP}}) - v_{\mathrm{xc}} | \psi_i^{\mathrm{KS}} \rangle, \tag{2.104}$$

where ψ_i^{KS} are the KS orbitals, Σ is the self-energy in the GW approximation calculated from the KS orbitals and eigenvalues, and v_{xc} is the exchange-correlation potential. Consequently, the quality of the G_0W_0 results depends on the starting point, i.e., functional and/or basis set, used. A G_0W_0 calculation using a specific starting point will be denoted as G_0W_0@method where necessary. For example, G_0W_0 used in combination with B3LYP/TZVP will be referred to as G_0W_0@(B3LYP/TZVP), or G_0W_0@B3LYP if the basis set is not the primary consideration.

To find a favorable hybrid functional as the starting point for G_0W_0 calculation, one can use an IP-tuning procedure for long-range corrected (LC) hybrid functionals as described in Ref. [38]. The basic idea is to separate the Coulomb operator into short-range (SR) and long-range (LR) components via the standard error function:

$$\frac{1}{r} = \underbrace{\frac{1 - \mathrm{erf}(\omega r)}{r}}_{\mathrm{SR}} + \underbrace{\frac{\mathrm{erf}(\omega r)}{r}}_{\mathrm{LR}}, \tag{2.105}$$

where ω is a range separation parameter. This makes it possible to combine the short-range interactions in the hybrid description with the correct asymptotics of full HF exchange in

the long range. Take the LC-hybrid functional LC-ωPBE as an example, where PBE is the semilocal functional of Perdew, Burke, and Ernzerhof [39]. The exchange-correlation functional takes the following form:

$$E_{\mathrm{xc}}^{\mathrm{LC}-\omega\mathrm{PBE}} = E_{\mathrm{x}}^{\omega\mathrm{PBE,SR}} + E_{\mathrm{x}}^{\mathrm{HF,LR}} + E_{\mathrm{c}}^{\mathrm{PBE}}, \tag{2.106}$$

where $E_{\mathrm{x}}^{\omega\mathrm{PBE,SR}}$ is the short-range ωPBE functional [40, 41], $E_{\mathrm{x}}^{\mathrm{HF,LR}}$ is the long-range HF exchange and $E_{\mathrm{c}}^{\mathrm{PBE}}$ is the semilocal PBE correlation [39]. According to the IP theorem [42, 43], the negative of the HOMO eigenvalue of exact KS theory equals the first vertical IP. However, this theorem is not obeyed by standard hybrid functionals. The best possible value for ω can thus be found by tuning such that the IP theorem is obeyed.

In this work, we will focus on the error introduced by the insufficiency of the basis set known as the basis set incompleteness error (BSIE). In practice, a complete basis set calculation can never be achieved. However, the correlation-consistent basis sets, denoted as cc-pVXZ where"cc-p" means "correlation-consistent polarized" and X is the number of linear combinations of primitive GTOs to describe each valence orbital [44, 45, 46, 47, 48], are designed to achieve smooth convergence to the complete basis set (CBS) limit. Various CBS extrapolations have been proposed, and no single one is found to be the best in all cases [49, 50]. However, it appears that any extrapolation produces higher quality results than the unextrapolated counterpart.

Chapter 3

Use of Programs

This work is centered around the calculation of vibronic absorption, emission, resonance Raman, and photoelectron spectra of the molecules of interest. Current codes exist for such purposes: FCclasses [51] and VIBES [52] for the calculation of vibronic absorption and emission spectra, in the time-independent and time-dependent regimes, respectively; ORCA [34] for resonance Raman spectra (limited to the IMDHOFA model). To calculate all these kinds of spectra in all models (IMDHO, IMDHOFA, and IMDHOFAD), the home-built Zzzap package has been developed, evolving from a prototype written in FORTRAN 77. It has been rewritten in FORTRAN 90 and Python 2.7 with known bugs fixed and efficiency improved.

The program Zzzap works in the following way:

1. Reading in the optimized geometries of the ground and excited state in Cartesian coordinates from G09 output files;
2. Reading in the normal modes and vibrational frequencies for both states;
3. Calculating the Duschinsky matrix and the dimensionless origin shift;
4. Calculating the auto/cross-correlation function in the Heller formalism;
5. Invoking the Fast Fourier Transform (FFT) package for Fourier transformation of the correlation function to generate the spectra.

The above procedure is automated, provided that the user specifies the following key parameters when running the program:

1. The type of spectrum (absorption, emission, resonance Raman or REP);
2. Models for the harmonic oscillator approximation (IMDHO, IMDHOFA, or IMDHOFAD);

3. Time step and grid size for the correlation function;

4. Broadening factor(s);

5. Files from which data should be input from.

The above procedure is depicted in Fig. 3.1.

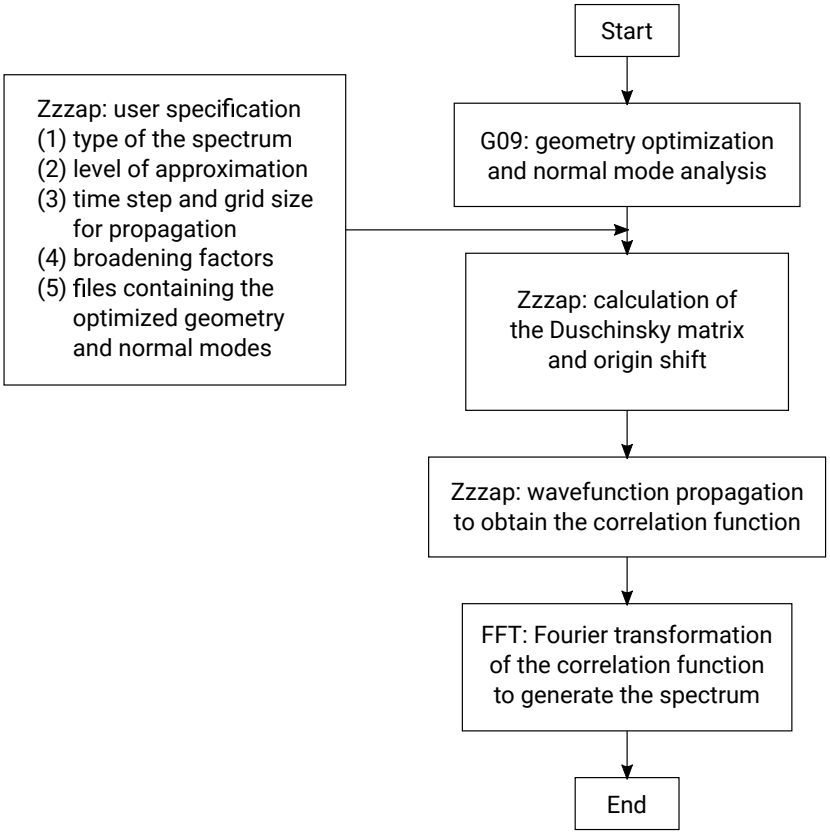

Figure 3.1: A flowchart of the way Zzzap works in combination with the external program Gaussian 09.

The program has been tested against VIBES and ORCA for *trans*-1,2,3-hexatriene and a few other molecules.

Chapter 4

Vibrationally resolved absorption and fluorescence spectra of perylene and N-substituted derivatives [53]

4.1 Overview

Carbon based materials are promising future materials for electronics, optoelectronics and other applications [54]. In this respect, poly(*peri*-naphthalene) (PPN, Fig. 4.1, upper panel), a graphene nanoribbon, is one of the materials of particular interest [55, 56, 57]. PPN has high thermal and chemical stability, relatively high electrical conductivity, and a narrow bandgap which is tunable by the preparation conditions [57].

As the basic "building block" of PPN, perylene (Fig. 4.1) serves as an excellent object of study for a better understanding of PPN itself. In particular, the relatively small size of perylene makes it a perfect system for theoretical investigations. In recent years, nitrogen analogues of perylene have attracted considerable attention. Various azaperylenes have been synthesized and characterized [58, 59, 60, 61]. A systematic experimental study of the nitrogen dependence of the optical and photophysical properties of azaperylenes in a solvent, acetonitrile (MeCN), is currently underway [62, 63]. In this chapter we investigate the optical absorption and emission spectra of perylene (**P**) and selected N-derivatives as shown in Fig. 4.1 (lower panel), namely 1-azaperylene (**1-A**), 1,6-diazaperylene (**1,6-**

A), 1,7-diazaperylene (**1,7-A**), 1,12-diazaperylene (**1,12-A**), 1,6,7-triazaperylene (**1,6,7-A**), and 1,6,7,12-tetraazaperylene (**1,6,7,12-A**). This series is the same as the one being studied in the mentioned forthcoming work [63]. Here we explore by quantum chemistry trends in optical spectra of these species with respect to the number and position of N atoms. Further, our studies could also be of relevance for other promising, unsaturated, C and N containing materials for photocatalysis, such as graphitic carbon nitride [64, 65].

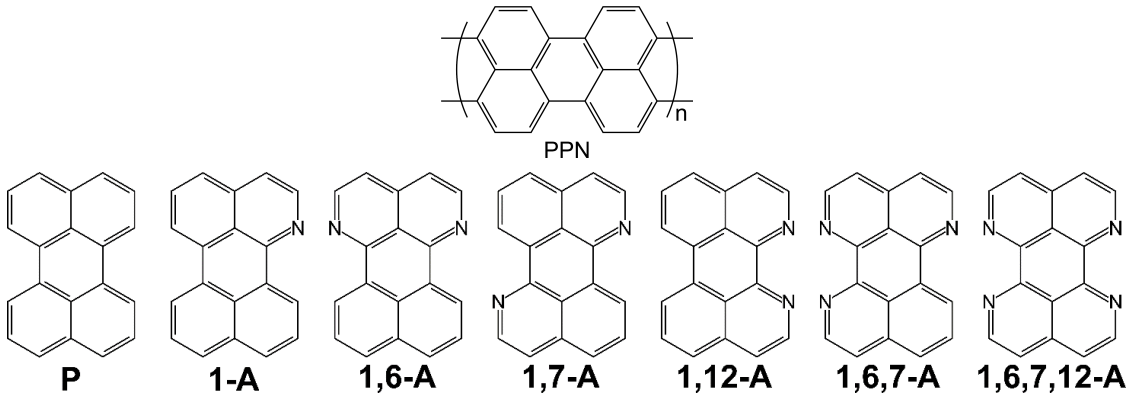

Figure 4.1: Upper panel: Chemical structure of poly(*peri*-naphthalene) (PPN). Lower panel: Chemical structures of molecules studied here (left to right): perylene (**P**); 1-azaperylene (**1-A**); 1,6-diazaperylene (**1,6-A**); 1,7-diazaperylene (**1,7-A**); 1,12-diazaperylene (**1,12-A**); 1,6,7-triazaperylene (**1,6,7-A**); 1,6,7,12-tetraazaperylene (**1,6,7,12-A**).

4.2 Methods

The following calculations were done with the quantum chemical package Gaussian 09 within DFT (for ground states) and linear-response TD-DFT (for excited states). The B3LYP functional and the TZVP basis set were adopted in all cases. Atomic positions in the ground and excited states of interest of the respective molecules were relaxed until the forces were smaller than $4.5 \times 10^{-4}\, E_\mathrm{h}/a_0$ and the maximum density matrix change was smaller than 10^{-6}. Harmonic vibrational frequencies and normal modes for the ground state were obtained by using analytic second derivatives for the Hessian, while for the excited states the central finite difference method with 0.1 pm displacement of atoms in each Cartesian direction was applied.

In a first step, we calculated vertical, broadened absorption spectra in the form of

molecular absorptivities from

$$\varepsilon(\omega) = \sum_i \frac{f_i}{\kappa} \frac{1}{\pi} \frac{\gamma}{(\omega - \omega_i)^2 + \gamma^2}. \tag{4.1}$$

Here, the sum goes over all considered excited singlet states with oscillator strength f_i and *vertical* excitation energy ω_i, $\kappa = \frac{4m_e c^2 \varepsilon_0 \ln 10}{N_A e^2} = 4.319 \times 10^{-10}\,\mathrm{mol \cdot m^{-1}}$, and γ is a Lorentzian broadening factor [66]. In this study, $\gamma = 1000\,\mathrm{cm^{-1}}$ is chosen. These calculations were performed in the gas phase as well as in the PCM using the solvent MeCN (dielectric constant = 36.6) to simulate the effects of the solvent studied in experiments [62, 63]. Besides the "ordinary" LR-PCM, the SS-PCM solvation method was used as well, for vertical transitions to the lowest bright singlet states of each molecule. In most cases single molecules with or without embedding environment were considered. For one example (**1,6-A**), also the effects of a possible dimer formation were studied, by considering various π-stacked dimer models. In this case we added a semiempirical correction to include the dispersion forces (B3LYP+D3) for the ground state optimization [67].

For allowed, lowest-energy transitions we also calculated the vibrationally resolved absorption and emission spectra. For this purpose, we applied the time-dependent correlation function method together with the IMDHOFAD model as mentioned in Section 2.4. For the calculations reported here, we applied a $\Delta t = 0.1\,\mathrm{fs}$ time grid spacing for the evaluation of the time-integrals, a total propagation time of about 1 ps, and a Lorentzian damping factor of $\Gamma = 250\,\mathrm{cm^{-1}}$.

4.3 Results and discussion

4.3.1 Structure

For (aza)perylene molecules in Fig. 4.1, ground state geometry optimizations were performed on the level of theory outlined above. Our gas phase calculations yield perfectly planar ground state structures. For perylene, the C-C bond lengths are in the range of $1.37 \sim 1.47$ Å, and the C-C-C bond angles are between 118° and 122°, in agreement with X-ray diffraction data [68]. Substitution of carbon atoms with nitrogen has only small and local effects on the structural parameters, limited to the respective subrings. For the azaperylenes, typical C-N bond lengths are between 1.32 and 1.35 Å, and C-N-C angles around 119°. Application of implicit solvent models (PCM) has virtually no effect on the geometries.

4.3.2 Vertical absorption spectra

For all gas phase simulations, the first bright transition is dominated, in an orbital picture, by the highest occupied molecular orbital (HOMO) to lowest unoccupied molecular orbital

(LUMO) contribution (Fig. 4.2), an optically allowed $\pi \rightarrow \pi^*$ transition. In the case of

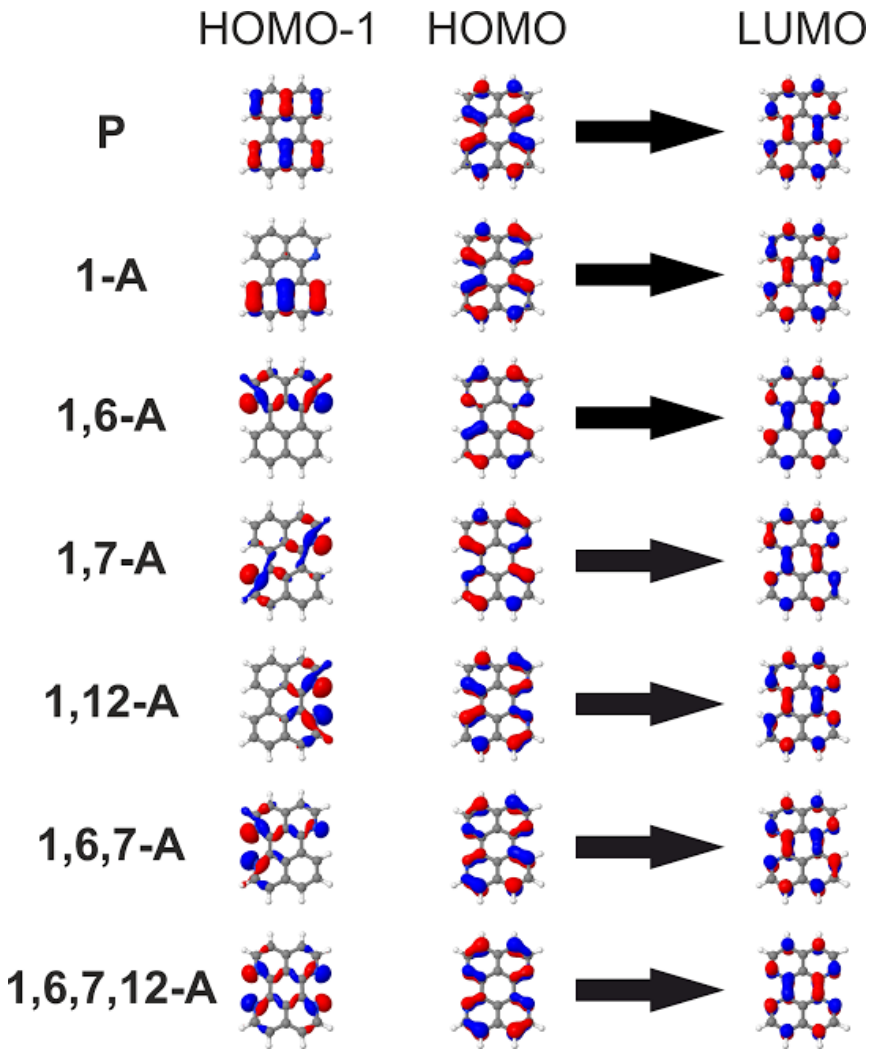

Figure 4.2: HOMO-1, HOMO and LUMO orbitals of the molecules studied in this work, calculated in the gas phase. Grey balls = C, white balls = H, blue balls = N. HOMO $\rightarrow$ LUMO transitions dominate the lowest-energy absorption bands in these molecules.

perylene, for example, with point group symmetry D_{2h}, the HOMO is of a_u symmetry and the LUMO is of b_{3g} symmetry. In state (rather than orbital) notation, this corresponds to a $X^1A_g \rightarrow^1 B_{3u}$ transition. The transition dipole moment is oriented along the long molecular axis $x \sim b_{3u}$. The direct product of initial and final states/orbitals and the transition dipole is totally symmetric, A_g. This transition changes the bonding/antibonding character of several C-C (or C-N) interactions in particular in the vicinity of the central aryl ring. For example, for perylene the two central C-C bonds are 1.47 Å long

on the B3LYP/TZVP level of theory in the ground state. Upon excitation to S_1, the non-bonding interaction of the HOMO between two center C atoms converts into a C-C bonding character. Similarly, the four nearby C-C bonds which are bonding in the HOMO are antibonding in the LUMO, resulting in a bond lengthening (from 1.39 to 1.42 Å) for these upon electronic excitation. In other words, in the excited state the bond alternation in neighboring C-C (or C-N) bonds reduces, a well-known effect for conjugated polyenes [69]. As a consequence, vibrational motion will set in upon absorption (and conversely also after fluorescence), which will show up in vibrational fine-structure (see below). Our calculations show that the presence of nitrogen heteroatoms has only a small effect on the characters of the HOMO and LUMO orbitals, both of which have π-character. In contrast the HOMO-1 orbitals strongly depend on the number and spatial distribution of nitrogen atoms (Fig. 4.2). For **P** the HOMO-1 orbital is of π-character delocalized over the whole molecule. Although for **1-A**, which contains one nitrogen atom, the HOMO-1 orbital is still of π-character, it is spatially localized on only half of the molecule. The HOMO-1 orbitals obtained for all molecules that contain at least two nitrogen atoms are of n-character and are located in the vicinity of nitrogen atoms. These orbitals are involved in low-lying $n \rightarrow \pi^*$ transitions which are usually dark but may play a role in photophysics through non-radiative transitions.

In the gas phase, the first bright state for all investigated molecules is the first excited state S_1, except for the molecule with the largest number of nitrogen atoms, namely **1,6,7,12-A**. For this particular molecule, the first bright state is the second excited state, S_2. The vertical excitation energies for the first bright state together with the respective oscillator strengths are presented in Table 4.1 (left part). The vertical excitation energies are between 440 nm (for **P**) and 406 nm (for **1,6,7,12-A**). Higher excited states, many of which are dark, are tabulated in Appendix B, Table B.1.

Analogous calculations were performed for the molecules in a MeCN solvent using PCM in two variants: LR-PCM and SS-PCM. Resulting vertical excitation energies for the first bright state and corresponding oscillator strengths are also given in Table 4.1 (right part). Higher excited states are tabulated in Appendix A, Table B.2. Also in PCM, the first bright state is dominated by a HOMO-LUMO transition. The solvent has little effect on the shape and character of HOMO and LUMO within the PCM models. The first bright state for all molecules, now also including **1,6,7,12-A**, is the first excited state S_1. For the LR-PCM model, we note that the solvent is predicted to red-shift the lowest bright excitation, by between 11 nm (for **P**) and 19 nm (for **1,12-A**). Also, oscillator strengths become larger. The LR-PCM seems to overestimate the solvent-induced red-shift, as the improved, non-equilibrium SS-PCM model partially reduces this shift again. However, an overall red-shift induced by the solvent remains for all molecules except perylene, for which almost no solvent effect is found within that model.

Simulated, broadened vertical absorption spectra are shown for the LR-PCM model in Fig. 4.3. They have been calculated from Eq. (4.1) by taking 20 excited states into

Table 4.1: The vertical excitation energy ΔE_{vert} and oscillator strength f for the first bright state of each molecule of the perylene series. Left: Gas phase calculations. Right: In MeCN solvent, treated by the LR-PCM (left part of right half), or by a non-equilibrium, SS-PCM (right part of right half). For the LR-PCM calculation, also the adiabatic energy separation ΔE_{ad} and the 0-0 transition energy ΔE_{0-0} are shown, obtained from geometry optimization in the excited state and normal mode analysis. The energies are in eV (nm in brackets).

	Gas phase		In MeCN solvent					
			Linear-response PCM				State-specific PCM	
Molecule	ΔE_{vert}	f	ΔE_{vert}	f	ΔE_{ad}	ΔE_{0-0}	ΔE_{vert}	f
P	2.82 (440)	0.35	2.75 (451)	0.45	2.39 (519)	2.35 (528)	2.83 (438)	0.35
1-A	2.86 (434)	0.36	2.77 (447)	0.45	2.41 (514)	2.37 (523)	2.83 (438)	0.35
1,6-A	2.93 (423)	0.36	2.84 (436)	0.46	2.48 (500)	2.42 (512)	2.90 (428)	0.36
1,7-A	2.89 (429)	0.36	2.80 (443)	0.46	2.42 (512)	2.36 (525)	2.85 (435)	0.36
1,12-A	2.91 (426)	0.36	2.78 (445)	0.44	2.41 (514)	2.35 (528)	2.78 (446)	0.34
1,6,7-A	2.97 (417)	0.37	2.86 (434)	0.45	2.47 (502)	2.41 (514)	2.88 (431)	0.36
1,6,7,12-A	3.05 (406)	0.37	2.93 (423)	0.46	2.52 (492)	2.45 (506)	2.95 (420)	0.36

account for each molecule. All simulated molar absorptivities reveal two main features, one at $\sim$ 420-450 nm, and one below $\sim$ 280 nm. The latter contains two main subfeatures, one at longer wavelengths than $\sim$ 240 nm, one at shorter ones. From Fig. 4.3 and Table 4.1, the following general trends emerge:

(i) Upon increasing the number of nitrogen atoms, the low-energy peak gradually blue-shifts from $\sim$ 450 nm for **P** to $\sim$ 420 nm for **1,6,7,12-A**.

(ii) Upon increasing the number of nitrogen atoms, the separation between the subfeatures of the higher energy peak decreases.

(iii) Also the relative intensity of the higher energy peak subfeatures and the lower energy peak subfeatures are influenced by the degree of substitution. Namely, the increase in the number of N atoms causes the higher energy peak subfeatures to become relatively more intense compared to the lower energy peak subfeatures.

(iv) Molar absorptivities of low-energy peaks are virtually identical for all molecules.

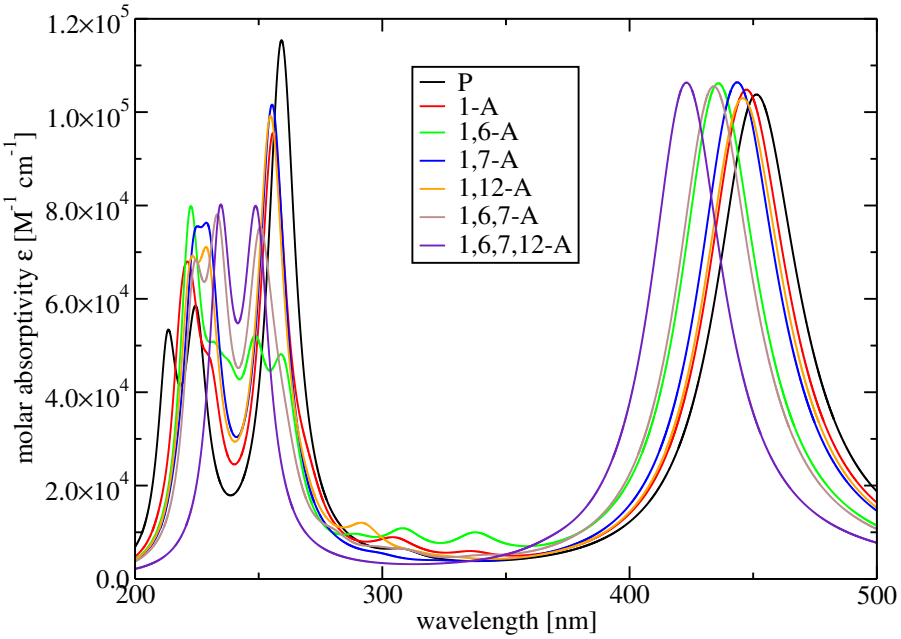

Figure 4.3: The molar absorptivity for the perylene series simulated for vertical excitation and with an implicit MeCN solvent, modelled by LR-PCM.

At this point it is worthwhile to compare to experimental data as far as available to us. Hasobe and coworkers have measured absorption and emission spectra of the (aza)perylene series of Fig. 4.1 in MeCN, showing the following main features [62, 63]:

(i) The experimental absorption spectra show a strong signal around $\sim$ 400-440 nm, ca. 100 nm wide, corresponding to the lowest-energy $S_0 \rightarrow S_1$ transitions. This band is separated by a gap $\sim$ 100 nm wide from higher-energy absorptions at $\leq$ 270 nm.

(ii) The lower-energy absorption bands exhibit a clear vibrational fine-structure, with at least two, sometimes three or more resolved peaks.

(iii) Both the $S_0 \rightarrow S_1$ and $S_0 \rightarrow S_n$ transitions ($n > 1$) show a rough trend comparable to theory: Higher *nitrogen content* shifts the bands to the blue. The shift is particularly large for **1,6,7,12-A** and comparable to what we find here. No clear trends, however, emerge regarding the *position* of the N atoms.

(iv) Also, the fluorescence (emission) spectra for the band corresponding to $S_1 \rightarrow S_0$ show a clear vibronic fine-structure. The emission bands are centered around $\sim$ 440-470 nm and are again, $\sim$ 100 nm wide.

(v) A special case seems to be **1,6-A**, for which absorption and emission spectra are qualitatively different from all other species of Fig. 4.1: The experimental spectra

[62, 63] are broader and strongly red-shifted. These latter features are characteristic for formation of an excimer state and have already been reported for perylene [70, 71] and derivatives of it [72]. They will also be investigated for **1,6-A** further below.

Apart from the last observation and also apart from the missing vibrational fine-structure, the vertical absorption spectra roughly resemble the absorption spectra found in experiment [62, 63]. The missing fine-structure and also the emission spectra will be addressed in Section 4.3.4.

4.3.3 Possible dimer formation

To study effects of dimer formation and excitonic effects on vertical (absorption) spectra, we considered, for **1,6-A** as an example, also dimer models. Specifically, we optimized the ground state structures for three different dimer arrangements as shown in Fig. 4.4. The three structures resulted from three different starting geometries in which the second monomer was either (a) slipped parallel or (c) anti-parallel along the long molecular axis, or (b) rotated relative to the first one. Note that at the B3LYP level, the interaction potential between two monomers is found to be repulsive, which is in agreement with simulations performed, e.g. for **P** in Ref. [73]. Thus, for the optimizations of stable dimeric species, we applied the B3LYP+D3 methodology that allows us to account for the dispersion interaction. Test calculations performed for the **1,6-A** monomer show virtually no influence of this semiempirical correction scheme on the chemical structure of the monomer.

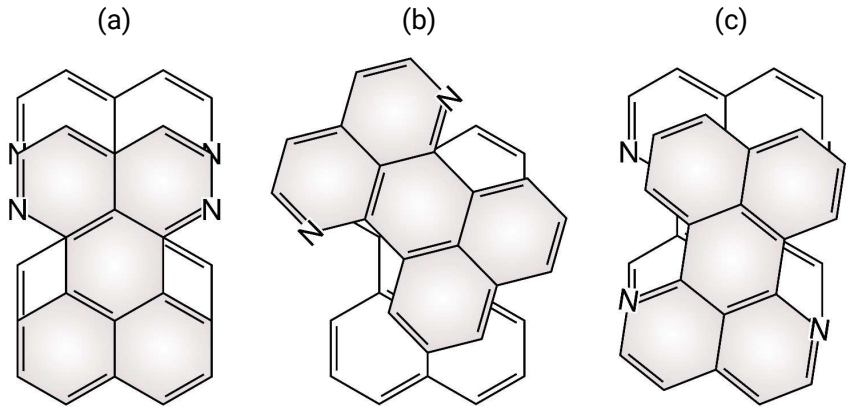

Figure 4.4: A schematic diagram of the three conformers of the **1,6-A** dimer obtained from B3LYP+D3/TZVP optimizations (see text).

In all cases presented in Fig. 4.4, the monomers are virtually planar and parallel, and the geometrical centers of monomers are shifted with respect to each other. In case (a), the monomers are simply slip-stacked (with the angle between dipole moments of the

monomers being only 1.7°), and the perpendicular distance between the two molecules is 3.45 Å; In case (b), the monomers form an angle of 44.2° with a distance of 3.40 Å; In case (c), the monomers are arranged almost anti-parallel (171.4°) at a distance of 3.46 Å. Apart from the three optimized structures shown, most likely further minima exist. On the B3LYP+D3/TZVP level of theory, dimer (b) is the most stable species, closely followed by dimer (c), which is 0.03 eV higher in energy and (a), at an energy 0.04 eV above (b). Due to the small energy differences, at ambient temperatures most likely all (and probably further) dimers will coexist: the relative Boltzmann populations (evaluated with the above relative electronic energies) at 300 K are 0.21:1.00:0.31 for a:b:c.

Table 4.2: The vertical excitation energy ΔE_{vert} and oscillator strength f (from the ground state S_0) for the four lowest excited states of the three conformers of the **1,6-A** dimer. Energies are in eV (nm in brackets). Also shown are the energies E of the dimers relative to the most stable species, b) (in eV), and the distance between molecular planes in the dimer, R (in Å). All on the (TD-)B3LYP+D3/TZVP level of theory.

Dimer	S_1		S_2		S_3		S_4		S_0	
	ΔE_{vert}	f	ΔE_{vert}	f	ΔE_{vert}	f	ΔE_{vert}	f	E	R
a	2.45 (507)	0.04	2.49 (498)	0.02	2.84 (436)	0.00	3.07 (404)	0.47	0.04	3.45
b	2.54 (489)	0.00	2.56 (485)	0.00	2.81 (441)	0.07	2.93 (422)	0.40	0.00	3.40
c	2.46 (505)	0.06	2.48 (500)	0.00	2.82 (439)	0.00	3.06 (405)	0.47	0.03	3.46

Relevant vertical excitation energies and the corresponding oscillator strengths calculated for the gas phase dimeric species are presented in Table 4.2. Excitation energies to higher excited states are tabulated in Appendix B, Table B.3. For all simulated dimers, the S_4 state is the first bright state with high oscillator strength. The vertical absorption energy for this state is blue-shifted by ~ 0.14 eV (19 nm) for (a), not shifted for (b), and blue-shifted for (c) by 0.13 eV (18 nm), with respect to the first bright state of the **1,6-A** monomer at 423 nm (Table 4.2). In addition for dimers (a) and (c), the first excited state carries a small, nonzero oscillator strength. In both cases, this state is strongly red-shifted by 0.5 eV or 80 nm, with respect to the first bright state of the **1,6-A** monomer. Further, for dimers (a) and (b) also states in between S_1 and S_4 (S_2 or S_3) exhibit small oscillator strengths and are red-shifted with respect to the monomer. Therefore, we have a broader distribution ($\sim$ 400-500 nm) of states for the dimer, compared to a single transition at 423 nm for the monomer. This may be helpful in interpreting the broader, lowest-energy absorption and emission bands in experiment for that molecule [62, 63]. Note that according to a simple point dipole/point dipole coupling model, the so-called Davydov (exciton) splitting of an excited state of a monomer in a dimer is $\delta \sim \mu^2/R^3$ for two monomers with parallel transition dipoles (of magnitude μ) being a distance R apart from each other

[74, 75]. For monomeric **1,6-A**, we find $\mu = 2.242$ ea$_0$ (oriented along the principle axis of the molecule). With a distance $R \sim 3.50$ Å, we then get $\delta \sim 0.5$ eV. This is the order of magnitude obtained for the splitting between various states as shown in Table 4.2.

4.3.4 Vibrationally resolved spectra

For deeper analysis, the vibrational fine-structure of absorption corresponding to the lowest-energy transition for each of the seven (aza)perylene molecules is of interest and computed, with the results shown in Fig. 4.5.

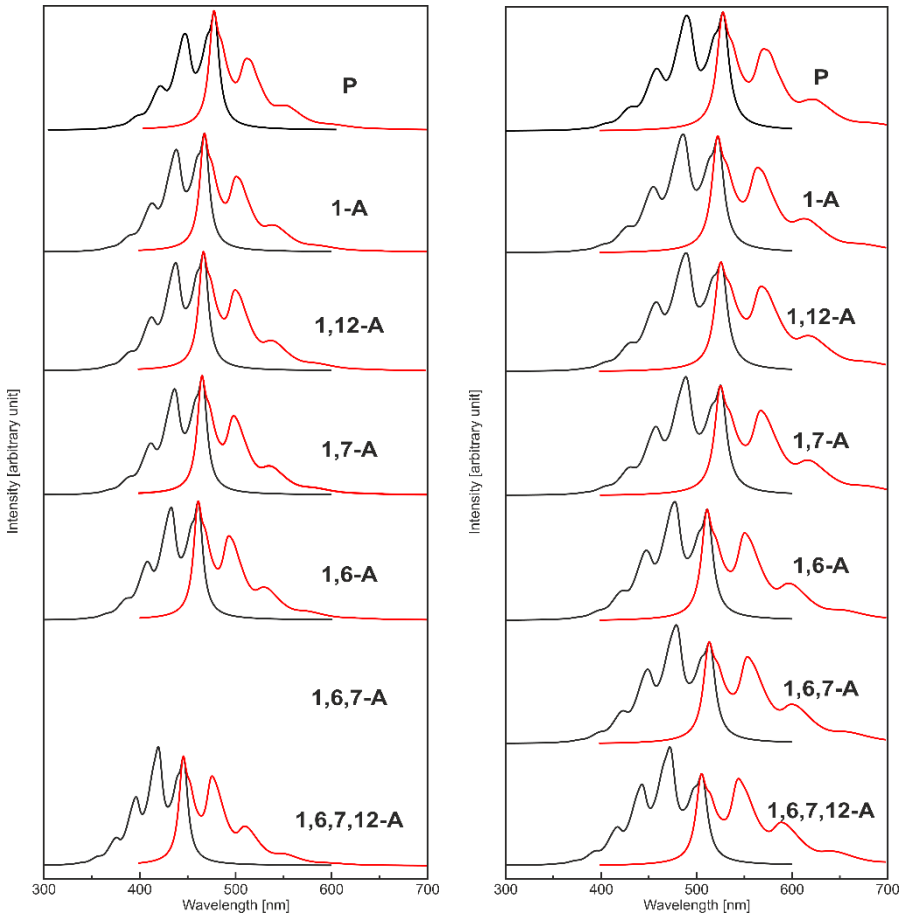

Figure 4.5: The vibronic absorption (black) and emission (red) spectra of the molecules studied in the gas phase (left) and in MeCN solvent (PCM, right) according to calculations. (**1,6,7-A** gas phase spectra are missing, because geometry optimization of the S_1 state failed in this case.)

In the same figure, the corresponding ($S_1 \rightarrow S_0$) vibronically resolved *emission* spectra are also presented. Both the vibronic absorption and emission spectra are computed using the IMDHOFAD model, in the gas phase and the LR-PCM (MeCN) solvent environment. For all molecules simulated in the gas phase, we obtain four distinctive peaks characterized by a vibrational progression of ~ 0.18 eV. The progression is largely independent of molecule but translates into a range of 26-31 nm on the wavelength scale depending on molecule, due to different excitation energies. In experiment, a clear vibronic fine-structure is found for the (aza)perylene molecules [62, 63] as outlined above. The experimental vibrational progression is quite comparable [62, 63]. The energy spacing of 0.18 eV corresponds to autocorrelation functions in Eq. (2.92) with recurrences having a period of 23 fs (not shown). This feature is the fingerprint of the excited state vibrational modes of frequencies around 1450 cm^{-1}. We find typically several excited state normal vibrations around this frequency, among them coupled C-C and C-N stretching modes which reflect the expected geometry changes in the central part of the molecules upon excitation as outlined above. For all molecules, the PCM solvent has no large impact on the general appearance of vibronic spectra, however, there are some quantitative differences: There is a systematic red-shift of between 52 nm (for **1,6-A**) and 60 nm (for **1,7-A** and **1,6,7,12-A**), and a slight increase of the relative intensities of the subpeaks at higher energies (shorter wavelengths). Further, the splitting between the two lowest-energy vibronic peaks, i.e. the vibrational progression Δ, apparently becomes larger in wavelengths, but is essentially unchanged in energy (eV), indicating a negligible effect of the solvent on the bond strengths. We denote the lowest-energy peaks as A and B, respectively, and show them in Table 4.3 together with the splitting parameter Δ, both for the gas phase and for PCM calculations. A similar analysis can be done for emission spectra. On the energy

Table 4.3: Lowest two vibronic peaks A and B of the absorption spectra for the perylene series from simulations. Numbers in bold denote the most intense vibronic peaks. Left: gas phase; Right: in MeCN (PCM).

Molecule	Gas phase			In MeCN (PCM)		
	Peak A (nm)	Peak B (nm)	Δ (nm)	Peak A (nm)	Peak B (nm)	Δ (nm)
P	**473**	442	31	**528**	490	38
1-A	**468**	438	30	522	**486**	36
1,6-A	**460**	432	28	512	**477**	35
1,7-A	**465**	436	29	525	**489**	36
1,12-A	**467**	438	29	526	**489**	37
1,6,7-A	–[a]	–[a]	–[a]	513	**479**	34
1,6,7,12-A	445	**419**	26	506	**472**	34

[a] Geometry optimization for the S_1 state was not successful for **1,6,7-A**.

scale, the progression in this case is also 0.18 eV, suggesting that similar vibrations are excited upon return from the excited to the ground state.

From the absorption and emission spectra, we observe two general trends: (i) There is a gradual blue-shift of the spectra with increasing number of N atoms, similar to what was found for vertical spectra. For each molecule, the peak of overlap between the absorption and emission spectra is the 0-0 peak (peak A in Table 4.3). In our PCM simulations, this peak occurs at 2.35 eV (528 nm) for **P**, and at 2.45 eV (506 nm) for **1,6,7,12-A**. For all other molecules, see Table 4.3. In the gas phase the 0-0 peak is at 2.62 eV (473 nm) for **P**, and at 2.78 eV (445 nm) for **1,6,7,12-A**. (ii) With increasing number of N atoms, the intensity of peak B increases with respect to that of peak A.

Chapter 5

Vibrationally resolved absorption, emission and resonance Raman spectra of [2](1,3)adamantano[2](2,7)pyrenophane

5.1 Overview

Diamondoids are saturated hydrocarbons formed from interconnected cyclohexane units (more details in Chapter 6). One of their desirable properties is the flexibility of being functionalized, providing a repertoire of diamondoid building blocks tailored to various needs. In this regard, one such example is the combination of diamondoids (acting as electron-donors) with fullerenes (as electron-acceptors) to produce a hydrocarbon rectifier, 2-(diamantan-4-yl)-1,3-butadiene-C_{60} adduct [76]. The use of this molecule as a self-assembled diode material, however, suffers from the drawback of a small fullerene-metal contact area as well as the unstability due to retro-Diels-Alder reaction. Furthermore, the dipole moment is off the center of the fullerene subunit. Attempts have been made in the search for better hydrocarbon models. Inspired by studies on a simple model, [2](1,3)adamantano[2](1,4)benzenophane [77], consisting primarily of adamantane (the simplest diamondoid) and benzene, Kahl *et al.* recently synthesized a similar but larger molecule, [2](1,3)adamantano-[2](2,7)pyrenophane (abbreviated to Ada-py in the following, Fig. 5.1), by fusion of the sp^3-hybridized adamantane (electron-donor) with the sp^2-hybridized pyrene (electron-acceptor), and measured its electronic and optical prop-

erties [78]. This molecule possesses a large dipole moment resulting predominantly from the bending of the pyrene moiety and the electron-donating nature of adamantane.

In this chapter, we will study the vibronic absorption, emission and resonance Raman spectra of Ada-py, compare theoretical findings with experimental observations, attempting to gain insight into the design of novel diamondoid containing molecules for optoelectronic applications.

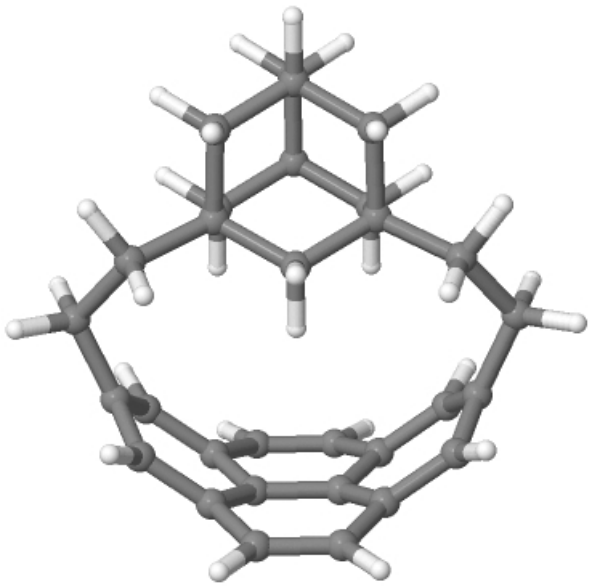

Figure 5.1: The ground state molecular structure of Ada-py, obtained on the B3LYP/TZVP level of theory without symmetry constraints.

5.2 Methods

The procedure used here to optimize the structure and perform normal mode analysis of Ada-py is similar to that in Section 4.2. The calculations were done on the B3LYP/TZVP DFT and TD-DFT level of theory.

First, the vertical absorption spectrum broadened with a Lorentzian factor $\gamma = 2000\,\mathrm{cm}^{-1}$ was computed according to Eq. (2.72). The ground state and first bright excited state were then used to calculate the vibronic absorption, emission and resonance Raman spectra according to the Heller formalism (Section 2.4). Correlation functions are computed on time grids with timesteps $\Delta t = 0.02\,\mathrm{fs}$, for a total propagation time of about 2 ps to make sure that the correlation functions converge to zero. The Lorentzian broadening factor $\Gamma = 200\,\mathrm{cm}^{-1}$ was chosen for absorption and emission, and another factor

$\tilde{\Gamma} = 10\,\mathrm{cm}^{-1}$ for resonance Raman spectra. All spectra were treated in the IMDHOFAD model.

5.3 Results and discussion

The optimized geometry on the B3LYP/TZVP level shows that the symmetry of the molecule is C_s (Fig. 5.1). The vertical excitation energies and oscillator strengths for the first ten excited states are calculated and presented in Table 5.1. The oscillator strength sticks and the broadened vertical absorption spectrum are shown in Fig. 5.2

For Ada-py, the first absorption occurs for the weakly allowed first excited state, at 3.46 eV. This is followed by three states (states 2, 3, and 5) of increasing intensity. At 4.49 eV (state 5), the absorption reaches its maximum. Two higher states (states 7 and 8) are also allowed transitions, with intensity comparable to that of the first excited state. The symmetry of Ada-py (C_s) is significantly reduced with respect to adamantane (T_d), consequently, the degeneracies are completely removed and much less states are transition forbidden by symmetry.

The dipole moments in ea_0 of the electronic ground state S_0 and the lowest three excited states S_1, S_2 and S_3 at the optimized ground state geometry of Ada-py are 0.9453, 1.1176, 1.0101 and 0.9958, respectively. The angles between the three excited state dipole moments and the ground state value are 0.5°, 1.0° and 3.2°, and their relative change in magnitude with respect to the ground state dipole moment are 18.22%, 6.85% and 5.34%, respectively. The nontrivial increase and the little change in direction of the dipole moment when the molecule is excited to S_1 might be of interest in designing new optoelectronic devices.

5.3.1 Vibronic spectra

Now we consider the vibronic effects on absorption and emission for the lowest allowed transition (state 1). We give different measures of transition energies in Table 5.2.

The simulated absorption and emission spectra are roughly mirror images relative to each other (Fig. 5.3). The maximum vibronic peak of each spectrum appears at essentially the same value as ΔE_{0-0}, so we assign this peak to the 0-0 transition. Each spectrum has a pattern of vibrational progressions. For the absorption spectrum, the vibronic peak spacing is about 0.164 eV, which stems from the recurrence time 25.21 fs of the absorption correlation function. Similary, the 0.163 eV vibronic peak spacing of the emission spectrum originates from the emission correlation function recurrence time 25.33 fs.

Table 5.1: Vertical excitation energies ΔE_{vert} in eV and oscillator strengths f of Ada-py, calculated on the B3LYP/TZVP level of theory, for the first ten excited states.

State	ΔE_{vert}	f
1	3.4623	0.0034
2	3.6718	0.0503
3	4.2282	0.1860
4	4.2665	0.0010
5	4.4876	0.5266
6	4.5342	0.0003
7	4.6957	0.0097
8	4.7109	0.0095
9	4.7982	0.0000
10	5.2066	0.0002

Table 5.2: Different measures of transition energies in eV, i.e. the vertical transition energy ΔE_{vert}, adiabatic transition energy ΔE_{ad}, and 0-0 transition energy ΔE_{0-0}, for the first excited state of Ada-py obtained on the B3LYP/TZVP level. The characteristic recurrence time τ in fs and corresponding vibrational frequency ω in cm^{-1} for absorption and emission autocorrelation functions are also given.

ΔE_{vert}	ΔE_{ad}	ΔE_{0-0}	τ_{abs}	ω_{abs}	τ_{emi}	ω_{emi}
3.46	3.22	3.23	25.21	1323	25.33	1317

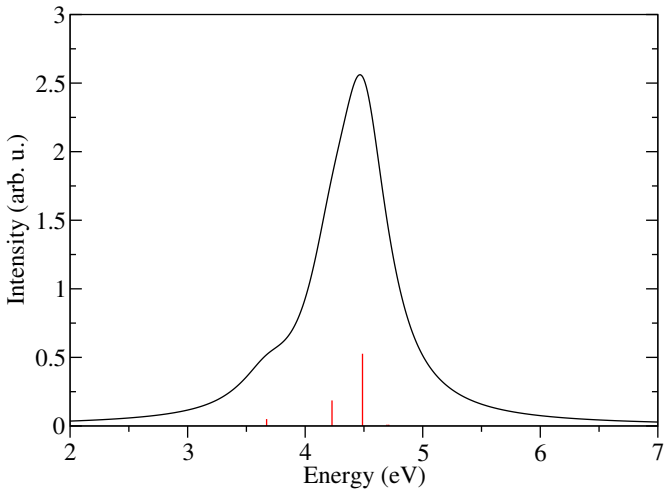

Figure 5.2: The vertical excitation spectrum (broadened with a Lorentzian factor $\gamma = 2000\,\mathrm{cm}^{-1}$) and oscillator strengths (sticks) of Ada-py on the (TD-)B3LYP/TZVP level.

The vibronic peaks of the absorption spectrum are dominated by vibrations in the excited state, while for emission, they are determined by ground state vibrations. To assign possible modes to these peaks, we note that the vibronic peak spacing 0.164 eV for absorption translates to a wavenumber of $1323\,\mathrm{cm}^{-1}$, and the vibronic emission peak spacing 0.163 eV is equivalent to $1317\,\mathrm{cm}^{-1}$. Further, we observe that the excited state geometry changes little in the adamantane cage compared with the pyrene structure. For example, the C-C bond lengths of the adamantane cage change less than 0.01 Å, and for C-C-C bond angles, the changes in value are less than 0.1°. For the pyrene structure, however, whereas most of the C-C bonds in the two "wings" (the two side subrings connected to the adamantane cage via sp^3 carbon atoms) are elongated by about 0.01 Å, the C-C bonds of the two middle subrings are shortened or elongated by $0.02 \sim 0.04$ Å; furthermore, the C-C-C bond angles can change by up to 2°. In the neighborhood of $1323\,\mathrm{cm}^{-1}$, we found 4 modes in the excited state with wavenumbers $1226\,\mathrm{cm}^{-1}$, $1314\,\mathrm{cm}^{-1}$, $1318\,\mathrm{cm}^{-1}$, and $1340\,\mathrm{cm}^{-1}$, respectively, which feature significant C-C stretching and C-H bending in the pyrene subrings. These modes or some of them should dominate the vibronic structure in the absorption spectrum. In the vicinity of $1317\,\mathrm{cm}^{-1}$, the modes in the ground state with wavenumber $1313\,\mathrm{cm}^{-1}$, $1317\,\mathrm{cm}^{-1}$, $1321\,\mathrm{cm}^{-1}$, and $1323\,\mathrm{cm}^{-1}$, respectively, are closest to $1317\,\mathrm{cm}^{-1}$, and they involve C-C stretching, CH_2 and CH vibrations in the adamantane cage and the connection units joining adamantane and the pyrene. These seem to dominate the vibronic emission spectrum. However, since the recurrences in the absorption (and emission, not shown) correlation function are not as well separated as they are in the case of pristine lower diamondoids, and the vibronic peaks are not sharply defined as they are in the vibronic spectra of pristine lower diamondoids [79], there could be a relatively large error when reading the recurrence time and vibronic peak spacing, therefore we cannot tell with equal confidence that these modes dominate the vibronic absorption (and emission) spectrum. In fact, there are many other modes in the region which could also contribute.

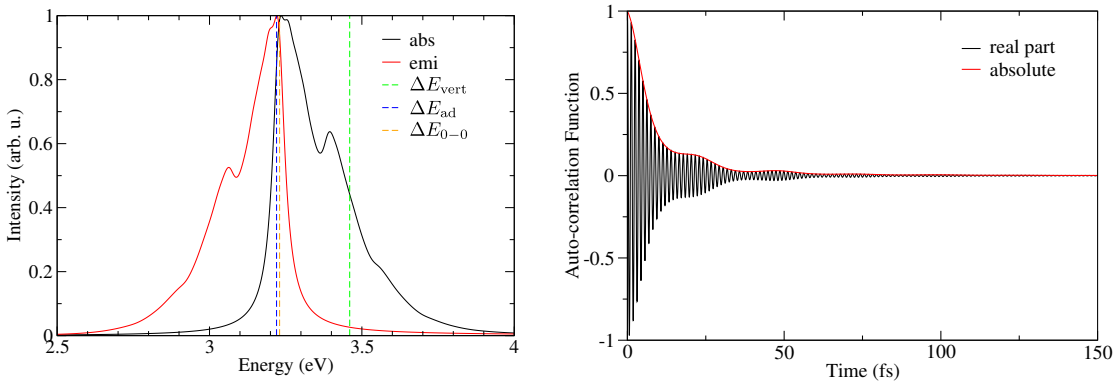

Figure 5.3: Left: Vibronic absorption and emission spectra for the first excited state of Ada-py using B3LYP/TZVP/IMDHOFAD. The maximal intensities are normalized to 1. A Lorentzian broadening factor $\Gamma = 200\,\mathrm{cm}^{-1}$ was included. Right: The real part and absolute value of the absorption correlation function.

To get more insight into this problem, we seek information provided by resonance Raman spectra.

5.3.2 Raman and resonance Raman spectra

The (off-resonance) normal Raman spectrum of Ada-py was calculated using Gaussian 09 (Fig. 5.4, upper panel). Most signals of frequencies lower than $1200\,\mathrm{cm}^{-1}$ are quite weak. The maximal intensity is found at $1300\,\mathrm{cm}^{-1}$, and a few more medium signals are located between $1400\,\mathrm{cm}^{-1}$ and $1700\,\mathrm{cm}^{-1}$.

The resonance Raman spectra of Ada-py calculated at three different excitation energies, 3.23 eV, 3.37 eV, and 3.81 eV, are shown in Fig. 5.4, lower panel. At excitation energy 3.23 eV, which is roughly the 0-0 transition energy, all modes in principle start to be in resonance. At 3.37 and 3.81 eV, the relative intensities are blue shifted to modes of frequencies higher than $1200\,\mathrm{cm}^{-1}$, or more specifically, the ones at around $1318\,\mathrm{cm}^{-1}$, $1344\,\mathrm{cm}^{-1}$, and $1472\,\mathrm{cm}^{-1}$.

For the rR spectrum (excitation energy 3.81 eV), the signal at $1472\,\mathrm{cm}^{-1}$ is significantly enhanced, whereas almost all the others are quenched with respect to the normal Raman spectrum. Based on the theoretical observation that resonance Raman spectra often give strong signals for modes contributing most to the vibronic emission spectra, and the signals are likely to be enhanced with respect to normal Raman spectra, at least for pristine lower diamondoids [79], we also attribute the $1344\,\mathrm{cm}^{-1}$ and $1472\,\mathrm{cm}^{-1}$ modes among the most probable contributors for the vibronic emission spectrum. A careful examination of the vibrations suggests that the latter should actually be the mode with vibrational frequency $1454\,\mathrm{cm}^{-1}$ that involves mainly the stretching of the three "horizon-

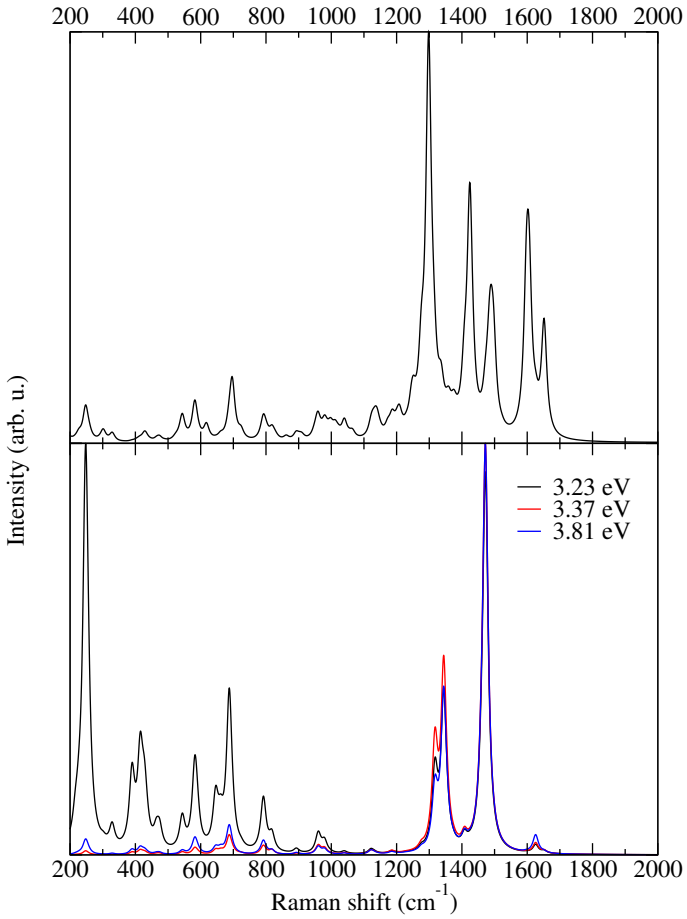

Figure 5.4: Upper: The (off-resonance) normal Raman spectrum of Ada-py calculated with Gaussian 09. Lower: The resonance Raman spectra of Ada-py using B3LYP/TZVP/IMDHOFAD for different excitation energies. A Lorentzian broadening factor $\Gamma = 10\,\mathrm{cm}^{-1}$ was included.

tal" C-C bonds (parallel to the paper) in the two middle subrings of the pyrene moiety, and these C-C stretching vibrations conform to the major changes in geometry when the molecule is excited to the S_1 state. The former should be the mode with vibrational frequency $1341\,\mathrm{cm}^{-1}$, which involves mainly the stretching of the rest eight C-C bonds in the same two subrings of pyrene.

5.3.3 Comparision with experiment [78, 80]

The experimental vibronic absorption and emission spectra [78] for Ada-py in cyclohexane solvent are given in Fig. 5.5. The absorption spectrum shown there corresponds to the $S_0 \rightarrow S_1$ transition. In experiment, much more intense absorption peaks are also found in

the region below 350 nm (not shown), indicating transitions to higher states than S_1 as also expected from our analysis in Table 5.1.

The experimental absorption maximum for the $S_0 \rightarrow S_1$ transition occurs at 383 nm (3.237 eV) and the vibrational progression is about 0.082 eV ($661\,\mathrm{cm}^{-1}$), which is one half of the theoretical value 0.164 eV. There is a mode of vibrational frequency $669\,\mathrm{cm}^{-1}$ which features C-C-C scissoring and C-H bending in the pyrene subrings, consistent with the geometrical changes upon excitation to S_1. This mode which "accidentally" has half of the frequency for the theoretical vibrational progression 0.164 eV is not resolved in the theoretical spectrum. The 0-0 peak appears to be at 406 nm (3.054 eV) where the absorption and emission spectral curves cross. However, it is more appropriate to assign the peak at 403 nm (3.077 eV, which is only 0.023 eV away from 3.054 eV) to the 0-0 transition, because the gap between this peak and the maximum peak is almost 0.164 eV, i.e. twice the experimental vibrational progression.

Considering we were simulating the gas phase spectra, the experimental absorption spectrum is probably red-shifted by about 0.16 eV. The "0-2" peak, i.e. the maximum absorption peak, in the experiment now coincides with the 0-0 peak at 3.23 eV in the simulated absorption spectrum, and the maximal intensity is shifted from the 0-0 to the higher energy "0-2" peak due to solvent effect, similar to what we have observed for the simulated absorption spectra of the (aza)perylene molecules (Fig. 4.5).

The experimental emission profile is somewhat similar to absorption, but the vibronic structure is not well resolved.

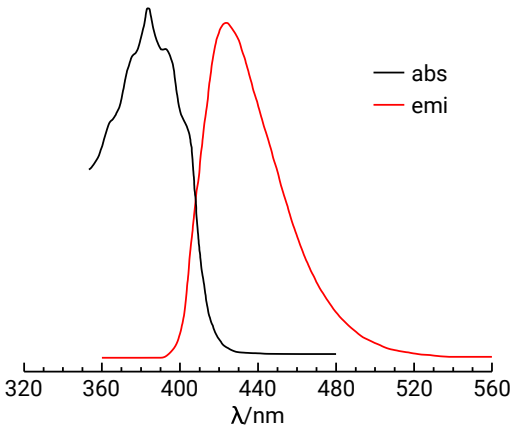

Figure 5.5: The vibronic absorption and emission spectra of Ada-py measured in cyclohexane, adapted from Ref. [78]. The intensities are in arbitrary units.

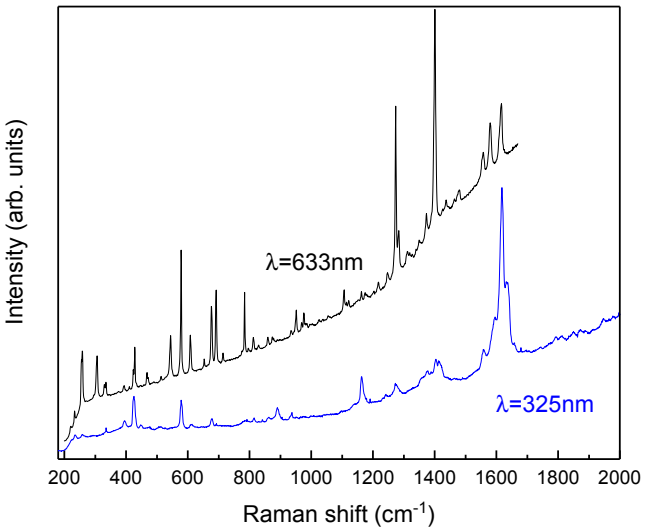

Figure 5.6: The (off-resonance, excitation wavelength $\lambda = 633\,\text{nm}$ or $1.96\,\text{eV}$) normal Raman and resonance (excitation wavelength $\lambda = 325\,\text{nm}$ or $3.81\,\text{eV}$) Raman spectra of Ada-py measured in crystal [80]. The intensities are in arbitrary units.

The experimental (off-resonance) normal Raman spectrum excited at wavelength 633 nm (1.96 eV) and resonance Raman spectrum excited at 325 nm (3.81 eV) are shown in Fig. 5.6. The former features a series of medium to strong signals from low frequency modes, and strong signals at about $1280\,\text{cm}^{-1}$ and $1400\,\text{cm}^{-1}$ are observed. Also, three medium signals at $1550\,\text{cm}^{-1} \sim 1600\,\text{cm}^{-1}$ are found. For the latter most signals in the lower frequency region extending to $1500\,\text{cm}^{-1}$ are quenched with respect to the normal Raman spectrum, but notably, the modes centered around $1600\,\text{cm}^{-1}$ are significantly enhanced.

For the simulated (off-resonance) normal Raman spectrum, the strong signals are mostly in the region $1200 \sim 1700\,\text{cm}^{-1}$, in qualitative agreement with the experimental Raman spectrum. For the simulated rR spectrum (excitation energy 3.81 eV), almost all observable signals except one is quenched with respect to the normal Raman spectrum as is the case for the experiment, but instead of the $1600\,\text{cm}^{-1}$ modes in the experimental rR spectrum, it is the mode around $1472\,\text{cm}^{-1}$ that is significantly enhanced. This mode should be the mode with vibrational frequency $1454\,\text{cm}^{-1}$, as we mentioned in Section 5.3.2. The frequency difference between the most enhanced modes in simulation and experiment might have something to do with the crystal environment of the Ada-py molecules.

Chapter 6

Vibrationally resolved photoelectron spectra of lower diamondoids [81]

6.1 Overview

Diamondoids form a family of H-terminated, saturated diamond-like molecules [82, 83, 84]. The simplest member is adamantane ($C_{10}H_{16}$, see Fig. 6.1 below, left), followed by the next homologues, diamantane ($C_{14}H_{20}$, Fig. 6.1, middle), triamantane, tetramantane, and so forth, formally with two, three, four ... adamantane cage units. Many diamondoids can be extracted from petroleum or are obtained from chemical synthesis [85]. Diamondoids can also be chemically modified by "doping" or functionalization [86, 87, 88], e.g. N-substitution of the four CH groups of adamantane leads to urotropine ($C_6N_4H_{12}$, Fig. 6.1, right).

Diamondoids are mechanically hard, chemically stable but versatile, and thermally conductive species, similar to their parent material diamond [89]. They are wide band gap semiconductors with negative electron affinity [90] as well as strong UV absorption and emission bands [91, 92], and are also monochromatic photoelectron emitters [90]. Because of these physico-chemical, optical and electronic properties on the one hand, and their chemical flexibility on the other (which can be used to tune properties), diamondoids and their derivatives are interesting not only for applications [83, 88, 89], but also as subjects of basic research [91, 92, 93, 79]. In contrast, diamondoid *cations* are much less studied, although small diamond-like molecules and their cations have been discussed as possible

species in interstellar media. Therefore, diamondoid cations are of significance for astrophysics [94], and possibly as reactive intermediates in general.

Molecular spectroscopies involving electronically excited states, i.e. absorption and fluorescence, have been shown to be powerful tools to characterize neutral and, for a few examples, also cationic diamondoids. Often (but not always) a rich vibrational fine-structure can be observed, serving as vibrational fingerprints. For instance, Möller and co-workers reported vibrationally resolved absorption and luminescence spectra of various neutral diamondoids (including urotropine [91, 92, 93]) and partially interpreted them on the basis of DFT in combination with normal mode analysis and stationary Franck-Condon methodology [92]. A time-dependent approach employing correlation functions [3, 4] was used in Refs. [79, 95] instead, for absorption, luminescence and resonance Raman spectra of pristine and artificially functionalized diamondoids, respectively.

Experimentally, also for photoelectron spectra of diamondoids vibrational fine-structure has been observed. A "classical" example is vibrational progressions in PES spectra of adamantane found by Schmidt [96]. More recent examples covering a wider range of natural and artificial diamondoids can be found in Ref. [97]. In recent theoretical work, PES spectra of adamantane, diamantane and urotropine were determined by Gali *et al.* [98]. They convincingly emphasized the role of electron-vibration coupling beyond the Born-Oppenheimer approximation, to explain satellite peaks in the high-energy portions of PES bands of these molecules. However, almost no account of the purely vibrational (Born-Oppenheimer related) fine-structure was made in their work.

In this chapter we present theoretical simulations of vibrationally resolved PES spectra of adamantane, diamantane and urotropine. Our focus is on the vibrational fine-structure of the lowest-energy bands of the PES spectra. The analysis rests on the time-dependent correlation function approach within the Born-Oppenheimer and harmonic approximations (Section 2.4).

6.2 Methods

The time-dependent correlation function method to calculate vibrationally resolved absorption spectra (Eq. (2.92)) hinges on the calculation of an autocorrelation function, which is the overlap between the initial state ϕ_0^{g} and its time evolution under the influence of the field-free, final excited state nuclear Hamiltonian, $\hat{H}_{\mathrm{f}} = \hat{H}_{\mathrm{e}}$ (Eq. (2.91)). In previous work on diamondoids [79, 99], this expression was used within the IMDHOFAD model, given that the ground and excited state molecular structures and the corresponding vibrational frequencies are computed using DFT and TD-DFT in the linear response formalism, respectively, to obtain vibrationally resolved optical absorption spectra [79, 99].

Now we employ an analogous approach for the calculation of vibrationally resolved photoelectron spectra, focusing on the lowest-lying ionized states. In this case, the initial state is the electronic ground state of the neutral molecule, the final state is the electronic ground state of the cation, and ω_{I} becomes the corresponding ionization energy (Eq. (2.92)). This approach neglects the kinetic-energy continuum of the emitted electron and transitions to higher PES bands (which could be included if desired) and is further based on the harmonic and Born-Oppenheimer approximations.

Neutral and cationic ground states are determined by the B3LYP functional with the TZVP basis set, using the quantum chemical package Gaussian09. Neutral adamantane, diamantane, and urotropine were treated by ordinary (restricted) B3LYP, and the open-shell (doublet) cations by the unrestricted B3LYP (UB3LYP) scheme. The adiabatic energy separation ΔE_{ad} is calculated by the Δ B3LYP method, as the difference between the energies of geometry-optimized cationic and neutral states, respectively. The Gaussian09 output of the B3LYP/TZVP calculations is imported to the home-built program Zzzap to calculate correlation functions and spectra. The correlation functions are computed on time grids with timesteps $\Delta t = 0.02\,\mathrm{fs}$, for a total propagation time of about 4 ps. A damping factor $\Gamma = 300\,\mathrm{cm}^{-1}$ is used to account for homogeneous broadening.

For diamondoids, several G_0W_0 calculations for ionization potentials have been reported in the literature [100, 101], however, with conflicting results as further discussed below. Therefore, in this work, we demonstrate that the IPs of diamondoids as derived from G_0W_0 depend strongly on the size of the employed basis set as well as the DFT starting point. For these calculations, the FHIaims code has been used [102].

6.3 Results and discussion

We consider the lowest-energy bands in the photoelectron spectra of adamantane, diamantane and urotropine, obtained with the methods just mentioned and compared to experimental data [96, 97, 98]. The ground state geometry of the three molecules, optimized on the B3LYP/TZVP level of theory, are shown in Fig. 6.1. Selected bondlengths and angles are denoted in the figure for later reference.

6.3.1 Adamantane

Geometries

Considering adamantane (henceforth also denoted as Ada) first, several geometric parameters (as defined in Fig. 6.1) are provided in Table 6.1. There we also give the analogous information for the adamantane radical cation (henceforth Ada^+), optimized on the

UB3LYP/TZVP level of theory. For adamantane, all C-H bondlengths of the CH units (r_1, r_3) are 1.094 Å, and those of the CH_2 units (r_2, r_4, r_5) are 1.095 Å. All C-C bonds (R_1, R_2, R_3) have the same bondlength, 1.540 Å. Each C-C-C angle with a tertiary C atom in the center (α_2, α_4) makes an angle of about 109.4°, while those C-C-C angles with secondary C atoms in the middle (α_3, α_5) have an angle of about 109.7°. These results are consistent with the well-known tetrahedral symmetry (T_d) of adamantane and experimental bondlengths and angles [103, 104].

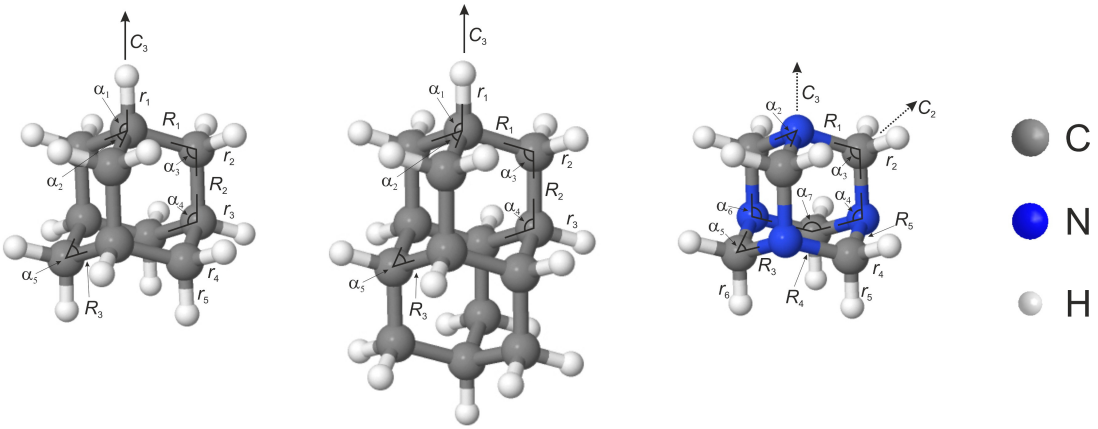

Figure 6.1: The ground state molecular structures of (left to right) adamantane, diamantane, and urotropine, obtained on the B3LYP/TZVP level of theory without symmetry constraints. r, R, and α refer to C-H bonds, C-C bonds, and bond angles, respectively. C_3 and C_2 denote relevant symmetry axes (see the text for details).

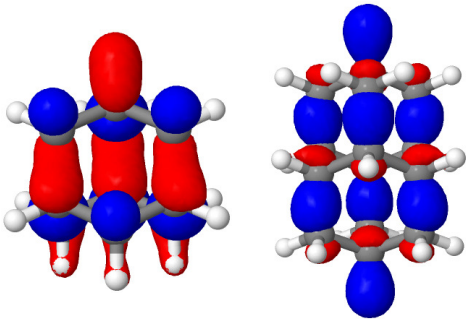

Figure 6.2: The HOMO of (left to right) adamantane and diamantane, obtained on the B3LYP/TZVP level of theory. Both orbitals are of bonding character in the region of the "vertical" C-C bonds.

For Ada^+, the symmetry equivalence of geometric parameters is partially removed with respect to the neutral molecule. The geometry changes upon ionization make previously equivalent bondlengths, e.g. r_1 and r_3, and R_2 and R_3, unequal. Most changes are small, with one notable exception: From the relative changes of geometric parameters k,

Table 6.1: Selected bond distances r (C-H) and R (C-C) (in Å) and angles α (in degrees) of neutral and cationic adamantane. Δ denotes the difference of the respective coordinates, and values in brackets the relative percentage change after ionization.

Bond parameters	Ada (T_d)	Ada^+ (C_{3v})	Δ	
r_1	1.094	1.125	+0.031	(+2.8 %)
r_2	1.095	1.090	-0.005	(-0.5 %)
r_3	1.094	1.092	-0.002	(-0.2 %)
r_4	1.095	1.092	-0.003	(-0.3 %)
r_5	1.095	1.100	+0.005	(+0.5 %)
R_1	1.540	1.513	-0.027	(-1.8 %)
R_2	1.540	1.612	+0.072	(+4.7 %)
R_3	1.540	1.522	-0.018	(-1.2 %)
α_1	109.6	105.7	-3.9	(-3.6 %)
α_2	109.4	113.0	+3.6	(+3.3 %)
α_3	109.7	105.4	-4.3	(-3.9 %)
α_4	109.4	107.2	-2.2	(-2.0 %)
α_5	109.7	111.1	+1.4	(+1.3 %)

defined as $(k(\mathrm{Ada}^+) - k(\mathrm{Ada}))/k(\mathrm{Ada})$, we see that in particular the three "vertical" C-C bondlengths of the adamantane cage (those parallel to the indicated C_3 axis), denoted as R_2 are substantially elongated, to 1.612 Å, or by close to 5 %. These results are consistent with the symmetry of the cation being reduced to C_{3v}, caused by the removal of an electron from the fully occupied triply degenerate HOMO of adamantane (t_2 symmetry). The HOMOs (Fig. 6.2) are bonding with respect to the mentioned three "vertical" C-C bonds, which explains the bond elongation. Altogether, the symmetry reduction is a manifestation of the Jahn-Teller effect, as recently directly verified by infrared spectroscopy in Ref. [104]. Despite the distortion, a pictorial representation of Ada^+ is hardly distinguishable from the geometry of the neutral molecule shown in Fig. 6.1. The same is true for diamantane and urotropine cations. While apparently small, the geometry distortion plays a crucial role in the explanation of both the Born-Oppenheimer related and of non-Born-Oppenheimer related vibronic fine-structure of the PES band to be presented below.

Table 6.2: Ionization potentials and contributions to them, computed for different molecules and with different methods. Also, experimental values for the adiabatic IP_a are given, and errors of the theoretical IP_a^{ZPE} values with respect to experiment. All quantities are in eV.

Property (method)	Ada	Dia	Uro
IP_a (exp.[a])	9.24	8.80	8.26
E_{rel} (B3LYP/TZVP)	0.40	0.51	0.34
ΔZPE (B3LYP/TZVP)	-0.23	-0.18	-0.03
IP_v (Δ B3LYP/TZVP)	9.47	9.08	8.13
IP_a^{ZPE} (Δ B3LYP/TZVP)[b]	8.84	8.39	7.76
error (IP_a) (Δ B3LYP/TZVP)	-0.40	-0.41	-0.50
IP_v (G_0W_0@B3LYP)[c]	10.13	9.56	8.49
IP_a^{ZPE} (G_0W_0@B3LYP)[d]	9.50	8.87	8.12
error (IP_a) (G_0W_0@B3LYP)	+0.26	+0.07	-0.14
IP_v (G_0W_0@PBE)[e]	9.86	9.28	8.17
IP_a^{ZPE} (G_0W_0@PBE)[f]	9.23	8.99	7.80
error (IP_a) (G_0W_0@PBE)	-0.01	+0.19	-0.46

[a] From Ref. [97]. [b] From Eq. (2.102). [c] 2-point CBS-extrapolated value, at B3LYP/TZVP geometry (see text). [d] From Eq. (2.102), with IP_v taken from extrapolated G_0W_0@B3LYP and E_{rel} and ΔZPE from B3LYP/TZVP. [e] 3-point CBS-extrapolated value, at B3LYP/TZVP geometry (see text). [f] From Eq. (2.102), with IP_v taken from extrapolated G_0W_0@PBE and E_{rel} and ΔZPE from B3LYP/TZVP.

Ionization potentials

For the discussion of ionization potentials, it may be helpful to refer to Eqs. (2.100)-(2.102).

As shown in Table 6.2, second column, the ZPE-corrected, adiabatic ionization potential IP_a^{ZPE} of adamantane is 8.84 eV on the Δ B3LYP/TZVP level of theory. In the table, also the vertical ionization potential IP_v (without ZPE corrections), as well as the relaxation energies and ZPE corrections in Eq. (2.102) are listed. The theoretical value for IP_a^{ZPE} is in accord with previous Δ B3LYP calculations (with different basis sets) [94, 105], and somewhat different from results obtained with a different functional (M06-

2X/cc-pVDZ), 9.32 eV, however without ZPE corrections [97]. According to experiment, the (ZPE-corrected) adiabatic ionization potential $\mathrm{IP_a^{ZPE}}$ of adamantane is 9.24 eV [97]. In the literature, also vertical ionization potentials $\mathrm{IP_v}$ for adamantane have been reported, most of them clustered around 9.75 eV [106]. Using Δ B3LYP/TZVP, we find a value $\mathrm{IP_v} = 9.46\,\mathrm{eV}$ without zero-point corrections. In summary, when we accept the experimental value for the adiabatic $\mathrm{IP_a^{ZPE}} = 9.24\,\mathrm{eV}$, the respective Δ B3LYP/TZVP result derived from Eq. (2.102) is redshifted by ~ 0.4 eV (Table 6.2).

The significant underestimation of the vertical IP derived by Δ B3LYP is in line with previous results for the calculation of IPs using global hybrid functionals [35]. In an attempt to go beyond the single-particle picture, Yin *et al.* [100] recently used G_0W_0 at a PBE reference together with a double-zeta basis with polarization and an extra set of diffuse functions, finding an ionization potential of 9.17 eV for adamantane. Since no relaxation effects and ZPE corrections were reported in that paper, this should be the vertical ionization potential $\mathrm{IP_v}$. Compared to the experimental reference of ~ 9.75 eV, this value is too low by more than half an eV. On the other hand, Demján *et al.* reported for the *adiabatic* IP of adamantane already a rather accurate value of $\mathrm{IP_a} = 9.11$ eV, when using G_0W_0 for a LDA Kohn-Sham reference and by including relaxation and ZPE effects as in Eq. (2.102) [101].

In order to shed more light on these somewhat conflicting *GW* results, we have calculated the vertical IPs of adamantane, diamantane, and urotropine using two different DFT starting points, i.e. the semilocal functional PBE [39] and the global hybrid functional B3LYP. In addition, we tested the convergence of the G_0W_0 derived IP with the size of the basis set. First of all, it turns out that G_0W_0 calculations depend strongly on the basis set, in contrast to ordinary KS-DFT (SCF) calculations. This is demonstrated in Fig. 6.3, where we show the HOMO energy as well as the vertical IP of adamantane, as a function of basis set for G_0W_0@PBE. The HOMO energy results from the respective KS calculation, whereas for the $\mathrm{IP_v}$ values the G_0W_0 correction was applied. In all cases, the geometry of the neutral molecule obtained from B3LYP/TZVP (Fig. 6.1, left) was adopted for simplicity.

From the figure, it can be seen that the *GW*-derived ionization potentials converge comparatively slowly with basis set size, while the HOMO energies are much less dependent on the basis set, at least for bases better than DZVP. The DZVP basis (a double-zeta valence split basis with polarization functions [107]) is the smallest basis set used here and gives $\mathrm{IP_v(DZVP)} = 9.05\,\mathrm{eV}$, while with the best basis, cc-pV6Z+diff (a correlation-consistent hextuple-valence split basis [48] with an extra set of diffuse functions [100]), we get $\mathrm{IP_v}$(cc-pV6Z+diff) = 9.80 eV. This large basis set effect could explain the too low ionization potential in Ref. [100], where a basis comparable to DZVP+diff was used for G_0W_0@PBE analogous to here. Note that according to Fig. 6.3, the extra diffuse functions have only a small effect on IPs (in contrast to excitation energies and electron affinities), and the largest angular momentum in the basis set is more decisive. Using cc-pVTZ+diff,

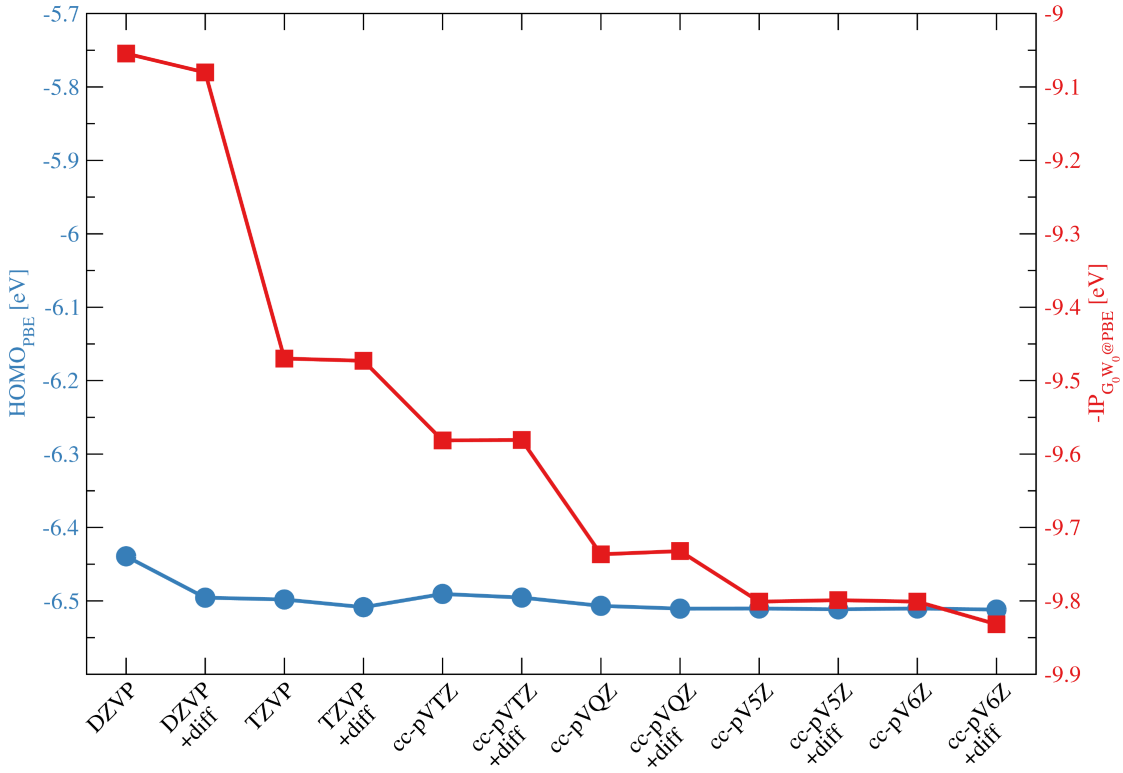

Figure 6.3: PBE HOMO energies (blue, left scale), as well as vertical ionization potentials (red, right scale) of adamantane obtained on the G_0W_0@PBE level, as a function of basis set. In all cases, the B3LYP/TZVP optimized geometry of the neutral species was used. DZVP=Double Zeta Valence with Polarization functions [107], TZVP=Triple Zeta Valence with Polarization [18], cc-pVXZ = correlation consistent polarized Valence X Zeta (X= T (Triple) [45], Q (Quadruple) [46], 5 (Quintuple) [47], 6 (Hextuple) [48]). "diff" denotes a set of diffuse Gaussian functions added at the center of the molecule as in Ref. [100].

cc-pVQZ+diff, and cc-pV5Z+diff G_0W_0@PBE values, we did a basis set extrapolation of the vertical IP values according to Ref. [108]

$$\mathrm{IP_v}(X) = \mathrm{IP_v}(\mathrm{CBS}) + A\ X^{-3} \quad , \tag{6.1}$$

where X is the cardinal number in the respective cc-pVXZ basis set (X=3, 4, 5 for T, Q, 5), and CBS denotes the complete basis set limit. A fit of the data gives $A = 7.49 \pm 0.25$ eV and an extrapolated, complete basis set value of $\mathrm{IP_v}(\mathrm{CBS}) = 9.86$ eV for G_0W_0@PBE. Adding to this value relaxation energies and ZPE corrections approximated from our B3LYP/TZVP normal mode analyses (Table 6.2), on this level of theory we obtain $\mathrm{IP_a^{ZPE}}(G_0W_0\text{@PBE}) = 9.23\,\mathrm{eV}$, in quantitative agreement with experiment (Table 6.2)

It is a well known fact that, due to its non-SCF implementation, the G_0W_0 approach leads to a significant dependence of the derived IPs from the DFT starting point

[109, 110, 111, 112, 113]. The dependence of G_0W_0 calculations on the DFT starting point is a well-known problem, and a number of solutions to this problem have been proposed, among them the quasiparticle self-consistent GW method [114]. For the IPs of molecular systems, one typically finds a significant underestimation by several tenths of an eV when using a semilocal starting point such as PBE for G_0W_0 [109, 113, 35, 38]. Therefore, the very nice agreement of the calculated adiabatic IP (9.23 eV) with the experiment (9.24 eV) is unexpected and may well be caused by a cancellation of errors in both experiment and theory. Generally speaking, hybrid functionals such as B3LYP have been found to yield better starting points for G_0W_0 calculations [109, 113, 35, 38], which is why we also employed the G_0W_0@B3LYP approach for comparison. Due to the additional computation costs when using a hybrid functional starting point, we in this case only used a 2-point basis set extrapolation with cc-pVTZ+diff and cc-pVQZ+diff basis sets, when extrapolating the G_0W_0@B3LYP IP to the basis set limit. Doing this, we obtain from G_0W_0@B3LYP a vertical IP of 10.13 eV at the CBS limit for adamantane. This is in very good agreement with Quantum Monte Carlo calculations [98], which found a vertical IP of 10.15 eV. Again, the adiabatic IP can be calculated from Eq. (2.102) by taking into account the B3LYP/TZPV relaxation energy and ZPE corrections, leading to $\mathrm{IP}_\mathrm{a}^\mathrm{ZPE}(G_0W_0@\mathrm{B3LYP}) = 9.50\,\mathrm{eV}$.

In summary, the G_0W_0 IPs are in slightly better agreement with experiment than those derived from Δ Kohn-Sham calculations. The Δ B3LYP values are red-, the G_0W_0@B3LYP slightly blueshifted, while G_0W_0@PBE probably accidentally, is right on top of experiment. We could use the many-body corrected IP values for the calculation of PES spectra, however, for simplicity we empirically shift the theoretical spectra to energies fitting the measured spectrum below as needed. In this context, one should also note that in Ref. [98] it has been found that the renormalization of the quasi-particle energy levels by electron-vibration interaction, which is neglected here, can give a lower-energy correction of the IPs in the order of about two tenths of an eV for small diamondoids.

Lowest-energy band of the photoelectron spectrum

The simulated first PES band of Ada is shown in Fig. 6.4, left panel. This band corresponds to ionization from the electronic ground state of the neutral molecule ($^1A_1$, $\mathrm{T_d}$) to the electronic ground state of the corresponding cation ($^2A_1$, $\mathrm{C_{3v}}$). To allow for a better visual comparison, the experimental and theoretical spectra are aligned along the first peak, which is found at 9.27 eV in the experiment. We identify this peak as the 0-0 transition between the neutral and cationic states. The center of the lowest experimental PES band has been given as 9.75 eV in Ref. [96], being close to the vertical $\mathrm{IP_v}$. Intensities in the figure have been arbitrarily adjusted in both data sets to coincide with each other in their maximal values. The theoretical spectrum has a FWHM of about 0.56 eV, and shows significant vibronic effects. A vibrational progression is found with a vibronic peak separation of about 0.159 eV. This separation stems from equidistant recurrences with a 26.1 fs recurrence time of the correlation function: On the scale of Fig. 6.4, middle panel, three such recurrences are seen. Assuming a single vibration to dominate, this

behaviour corresponds to an energy of 1280 cm^{-1}. The vibrational progression is a manifestation of vibrational energy levels in the final state [79]. Three normal modes are found in close vicinity of 1280 cm^{-1}, with wavenumbers of 1275 cm^{-1} and 1284 cm^{-1} (doubly degenerate), respectively. These modes are combinations of C-C stretching, C-H bending, CH_2 wagging and/or twisting in the cation, which seem to dominate the vibrational fine-structure of the simulated photoemission band. It should be noted that the vibrational mode with wavenumber 1275 cm^{-1} (Fig. 6.4, right) features besides vibrations involving large hydrogen movements, intense C-C stretching, all oriented along the principal axis C_3 (Fig. 6.1) of the cation. The corresponding C-C distance was identified above as the most affected geometric parameter of adamantane, when ionizing the neutral molecule (R_2, Table 6.1). The role of a very similar (albeit shifted ground state) mode with about the same frequency, had already been discussed in Ref. [98] in the contexts of the dynamic Jahn-Teller nature of Ada^+ and the main (non-satellite) signal in the PES of Ada.

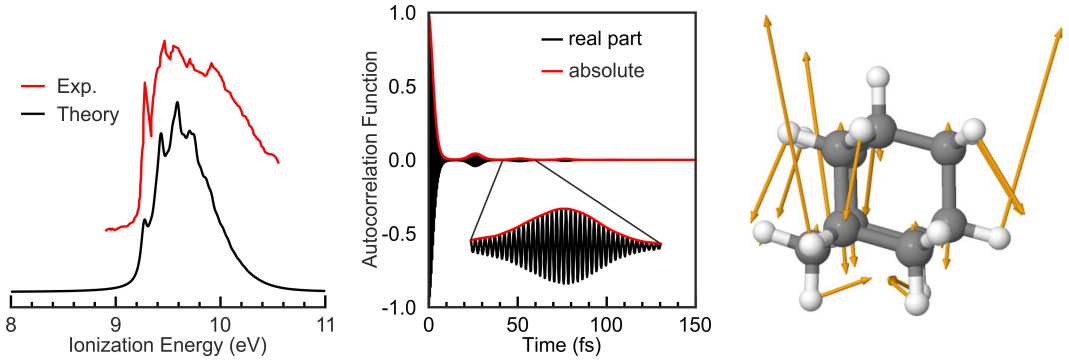

Figure 6.4: Left: The lowest-energy band of the simulated and experimental PES for adamantane. The experimental information is adapted from Ref. [96]. Middle: The absolute value and real part of the corresponding correlation function for the simulated band, showing recurrences. One of the recurrences is enlarged, exhibiting an underlying high-frequency oscillation which reflects the energy difference between cation and neutral molecule. Right: The vibrational mode of the adamantane cation with wavenumber 1275 cm^{-1} featuring by arrows, intense "vertical" C-C stretching – besides H motion which dominates due to its low atomic mass. This mode is suggested to make a major contribution to the vibrational progression in the first PES band of adamantane.

In general, the theoretical spectrum reproduces most of the fine-structure in the first photoemission band. However, the experimental spectrum appears to be broader: The intensity of the experimental spectrum at energies above 9.8 eV decreases much slower than in the simulation, and most notably an experimentally observed feature around 9.9 eV is not reproduced within our current model. As said, this has been claimed to be a consequence of the neglect of the coupling between the electrons and nuclei due to the Born-Oppenheimer approximation [98]. Indeed, a treatment of the PES of adamantane beyond the Born-Oppenheimer approximation which accounts for the electron-nuclear

coupling, produces satellite-type structures in the high-energy region of the band which help to better describe the spectrum around and above energies of 10 eV [98]. To be more specific, it was shown that the satellite peak at about 10 eV mainly originates from the coupling of the HOMO of Ada to a low-frequency (78.2 meV, 630 cm^{-1}) vibration. In passing we note that temperature effects on PES spectra seem to be minor: A test calculation, using a time-independent appraoch based on the IMDHO model at 300 K shows only small differences to a spectrum computed at 0 K (not shown).

6.3.2 Diamantane

The ground state geometry of diamantane (Dia) is shown in Fig. 6.1, middle, and relevant geometric parameters are listed both for Dia and the cation, Dia^+, in Table 6.3. For diamantane, the C-H bondlengths (r_1, r_2, r_3) fall in the range of $1.094 \sim 1.096$ Å. The C-C bonds (R_1, R_2, R_3) are 1.538 Å, 1.536 Å and 1.547 Å long. Relevant bond angles (α_1, α_2, α_3, α_4, α_5) are 107.7°, 111.2°, 107.6°, 108.9° and 110.1°, respectively. All of this is consistent with the D_{3d} point group symmetry of the molecule [79].

Variations of geometric parameters of the diamantane radical cation with respect to the neutral molecule (Table 6.3) show a similar trend to what was found for adamantane (Table 6.1). Namely, the corresponding parameters (with the same labels) change in the same direction, e.g. the "vertical" C-H (r_1) and C-C (R_2) bonds are elongated for both cations, while C-H (r_2, r_3) and C-C (R_1, R_3) bonds are shortened. Similar to adamantane, the most significant geometric parameter change of Dia^+ in comparison with neutral diamantane occurs for the six "vertical" C-C (R_2) bonds, which are elongated by 0.050 Å (or 3.2 %). While the elongation of the vertical C-C bonds of the adamantane radical cation reduces the high symmetry T_d of adamantane to C_{3v}, in the diamantane radical cation the point group symmetry D_{3d} is preserved [79]. Contrary to adamantane, the diamantane radical cation is not subject to a Jahn-Teller effect because the HOMO of neutral Dia is nondegenerate [105], a_{1g}. Instead, the similar geometry distortion to that of adamantane is due to a so-called pseudo Jahn-Teller effect [98]. The dominant C-C bond elongations are a consequence of the C-C bonding character of that orbital (Fig. 6.2).

The vertical IP for diamantane using the Δ B3LYP method is 9.08 eV as shown in Table 6.2, third column. The ZPE-corrected, adiabatic IP is $IP_a^{ZPE} = 8.39$ eV on the same level of theory. On this level, the adiabatic IP_a^{ZPE} is 0.41 eV lower than the experimental value of 8.80 eV [97] – similar to what was found for adamantane. Also for diamantane we carried out G_0W_0@B3LYP calculations at the B3LYP/TZVP geometry of the neutral molecule, and performed a 2-point CBS-extrapolation based on cc-pVTZ+diff and cc-pVQZ+diff IP_v values. Using Eq. (2.102) and B3LYP/TZVP relaxation energies and ZPE correction, we end up with $IP_a^{ZPE} = 8.87$ eV, in excellent agreement with experiment: The theoretical value is blueshifted by only 0.07 eV. The corresponding G_0W_0@PBE, 3-point extrapolated ionization potential $IP_a^{ZPE} = 8.99$ eV is now in slightly less good agreement

Table 6.3: Selected bond distances r (C-H) and R (C-C) (in Å) and angles α (in degrees) of neutral and cationic diamantane. Δ denotes the difference of the respective coordinates, and values in brackets the relative percentage change after ionization.

Bond parameters	Dia (D_{3d})	Dia^+ (D_{3d})	Δ	
r_1	1.094	1.108	+0.014	(+1.3 %)
r_2	1.095	1.091	-0.004	(-0.4 %)
r_3	1.096	1.093	-0.003	(-0.3 %)
R_1	1.538	1.520	-0.018	(+1.3 %)
R_2	1.536	1.586	+0.050	(+3.2 %)
R_3	1.547	1.526	-0.021	(-1.4 %)
α_1	109.7	107.7	-2.0	(-1.9 %)
α_2	109.2	111.2	+2.0	(+1.8 %)
α_3	109.8	107.6	-2.2	(-2.0 %)
α_4	110.5	108.9	-1.6	(-1.5 %)
α_5	108.4	110.1	+1.7	(+1.5 %)

with experiment: the error is +0.19 eV in this case. On every level, theory also confirms that the larger diamondoid(s) show(s) the well-known trend of decreasing IP with increasing size of the molecule [97].

The simulated first PES band of diamantane is shown in Fig. 6.5, left panel. Similar as for adamantane, the experimental and theoretical spectra are aligned along the first peak at 8.84 eV, which again can be identified as the 0-0 transition. Also here, a clear vibrational progression is observed: The vibronic peak separation of about 0.164 eV stems from a 25.1 fs recurrence time of the correlation function (Fig. 6.5, middle), and corresponds to a $\sim 1330\,\mathrm{cm}^{-1}$ wavenumber. Six normal modes are found around that wavenumber (from $1315\,\mathrm{cm}^{-1}$ to $1345\,\mathrm{cm}^{-1}$) and can be described as a combination of C-C stretching, C-H bending and CH_2 wagging and/or twisting. They are most probably the dominating modes for the first photoemission band. In particular, a vibrational mode of wavenumber $1315\,\mathrm{cm}^{-1}$ (Fig. 6.5, right panel) features intense C-C stretching along the principal axis C_3 (Fig. 6.1) of the diamantane cation. This conforms to the most significant geometric parameter change of Dia^+ with respect to neutral diamantane that occurs for the C-C bonds R_2 (Table 6.3), which are also along the principal axis C_3. All of this is quite analogous to adamantane. An analog of the $1315\,\mathrm{cm}^{-1}$ mode has also been found and analyzed in Ref. [98] in terms of the pseudo Jahn-Teller effect and for its role in the PES of diamantane. We note that compared to adamantane, however, the recurrences of diamantane are

more pronounced: four of them are seen on the scale of Fig. 6.5, rather than three. As a consequence, the vibrational fine-structure of diamantane shows a stronger contrast and more vibrational peaks become visible. We attribute this behaviour to the fact that the overall geometric changes in diamantane are less pronounced than in admantane, giving rise to a correlation function with more recurrences.

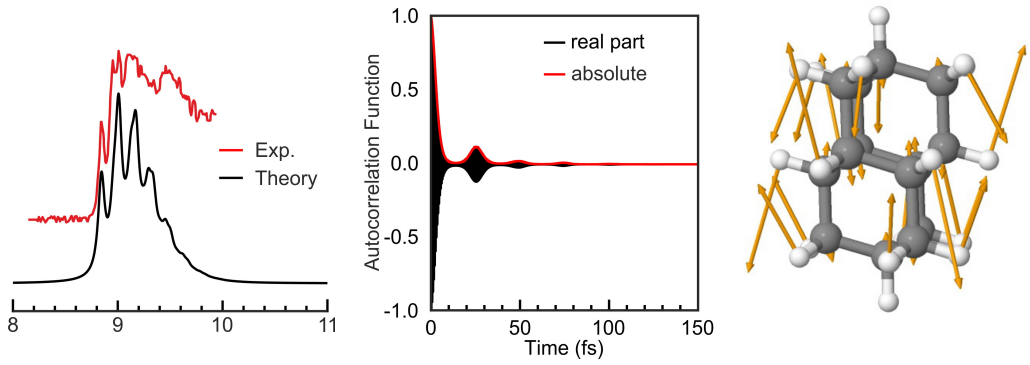

Figure 6.5: Left: The lowest-energy band of the simulated and experimental PES for diamantane. The experimental information is adapted from Ref. [97]. Middle: The absolute value and real part of the corresponding correlation function for the simulated band, showing recurrences. Right: The vibrational mode of diamantane cation with wavenumber $1315\,\mathrm{cm}^{-1}$, which features intense vertical C-C stretching (besides the dominating H motions). This mode is suggested to make a major contribution to the vibrational progression in the first PES band of diamantane.

The overall agreement between theoretical and experimental PES spectra of diamantane is reasonably good. It should be noted that, as for adamantane, features at the high-energy wing of diamantane's PES are not reproduced either. Again, attempts have been made to remedy this discrepancy by going beyond the Born-Oppenheimer picture [98].

6.3.3 Urotropine

Finally, we analyze the lowest-energy PES peak of urotropine. The ground state geometry of neutral urotropine (Uro) is shown in Fig. 6.1, right, and relevant geometric parameters for both Uro and Uro^+ are given in Table 6.4. For urotropine, all C-H bonds (r_2, r_4 and r_5) are about 1.092 Å, and all C-N bonds (R_1, R_3, R_4 and R_5) are about 1.470 Å on the B3LYP/TZVP level. All N-C-N angles (α_3, α_5, α_7) are about 112.4°, and all C-N-C angles (α_2, α_4, α_6) are about 108.0°. Substitution of tertiary C-H units of adamantane by N does not break the $\mathrm{T_d}$ symmetry.

Upon ionization, C-H bonds (r_2, r_4, r_5, r_6) are shortened by about $0.003 \sim 0.005$ Å. The C-N bonds R_1 and R_4 are elongated, while the C-N bonds R_3 and R_5 are shortened,

Table 6.4: Selected bond distances r (C-H) and R (N-C) (in Å) and angles α (in degrees) of neutral and cationic urotropine. Δ denotes the difference of the respective coordinates, and values in brackets the relative percentage change after ionization.

Bond parameters	Uro (T_d)	Uro$^+$ (C_{2v})	Δ	
r_2	1.092	1.089	-0.003	(-0.3 %)
r_4	1.092	1.089	-0.003	(-0.3 %)
r_5	1.092	1.089	-0.003	(-0.3 %)
r_6	1.092	1.087	-0.005	(+0.5 %)
R_1	1.474	1.479	+0.005	(+0.3 %)
R_3	1.474	1.470	-0.004	(-0.3 %)
R_4	1.474	1.481	+0.007	(+0.5 %)
R_5	1.475	1.469	-0.006	(-0.4 %)
α_2	108.0	105.9	-2.1	(-1.9 %)
α_3	112.4	112.2	-0.2	(-0.2 %)
α_4	108.0	109.2	+1.2	(+1.1 %)
α_5	112.4	100.5	-11.9	(-10.6 %)
α_6	108.0	110.5	+2.5	(+2.3 %)
α_7	112.4	109.0	-3.4	(-3.0 %)

the change (absolute value) in bond length being in the range of $0.004 \sim 0.007$ Å. Altogether, compared to adamantane and diamantane, the bondlength changes are small, never exceeding 0.5 %. The most significant changes are in bond angles. In particular, one of the N-C-N angles (α_5) decreases by about 11.9° (or close to 11 %). As in the case of the adamantane radical cation, the Jahn-Teller distortion is also in effect, resulting in a C_{2v} geometry due to the removal of an electron from the HOMO of t_2 symmetry.

The vertical IP for urotropine using Δ B3LYP is 8.13 eV according to Table 6.2, last column, and the corresponding ZPE-corrected, adiabatic IP is $IP_a^{ZPE} = 7.76$ eV. On this level, the adiabatic IP_a^{ZPE} is now 0.50 eV lower than the experimental value of 8.26 eV [97]. For urotropine, the 2-point basis set extrapolated G_0W_0@B3LYP calculations predict a vertical IP of 8.49 eV. With the help of Eq. (2.102), this translates to an adiabatic IP of 8.12 eV, which is in very good agreement with experiment, showing only a small redshift of 0.14 eV. With a PBE reference (G_0W_0@PBE), the corresponding 3-point extrapolation gives $IP_a^{ZPE} = 7.80$ eV, with an error of -0.46 eV compared to experiment. All of this shows that generally, a good reference (e.g. B3LYP) is needed in combination with a good basis

set, to arrive at accurate ionization potentials for diamondoids. In passing we note that a G_0W_0@LDA approach with a smaller basis set used in Ref. [101] resulted in an adiabatic IP of 8.18 eV – a (probably accidentally) very good value compared to experiment.

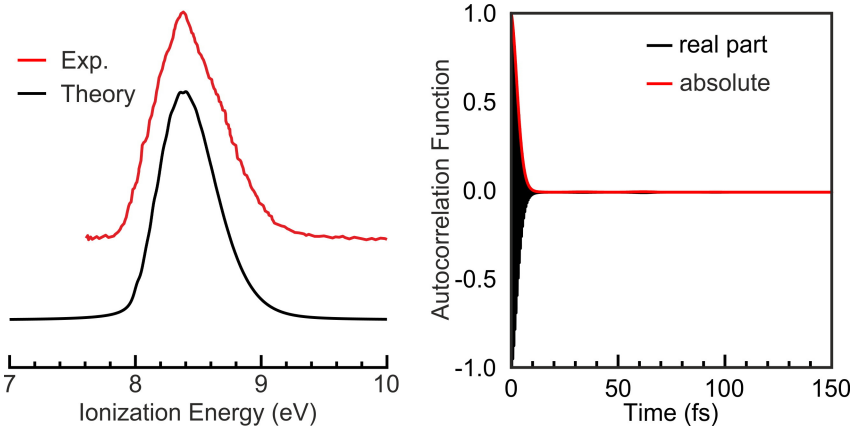

Figure 6.6: Left: The lowest-energy bands of the simulated and experimental PES for urotropine. The experimental information is adapted from Ref. [96]. Right: The absolute value and real part of the corresponding correlation function for the simulated band, showing only very weak recurrences.

The simulated and experimental first PES band of urotropine are shown in Fig. 6.6 (left). Again, the experimental and theoretical spectra have been aligned. Unlike for adamantane and diamantane, no vibrational fine-structure is present in the simulated first photoemission band, and also not in experiment. The lack of vibrational fine-structure is a consequence of the rapid decay of the recurrence pattern and the relatively long recurrence time, 32.0 fs. In fact, only two very weak recurrences are seen at Fig. 6.6, right, at $t \sim 32$ and 64 fs, respectively. Similar phenomena have also been observed in the experimental and theoretical UV absorption spectra of neutral urotropine, which are also unstructured [93, 95]. Note that upon ionization there is no significant elongation of the "vertical" C-N bonds in contrast to the elongated "vertical" C-C bonds for adamantane and diamantane. Instead, the N-C-N angle α_5 is decreased by about 12° as mentioned above. A recurrence time of 32 fs corresponds to a vibrational energy of about 1040 cm^{-1}, and indeed there are several "soft" vibrational motions around this energy that involve the N-C-N (α_5) scissoring. Such "soft" vibrations are also found in Ref. [98], one of which is a fully symmetric A_1 0.129 eV (1140 cm^{-1}) mode, in agreement with our findings here. However, this N-C-N (α_5) scissoring motion is strongly mixed with other components (not shown). Further, the vibrational density of states around 1000 cm^{-1} and below is found to be comparatively large. This suggest that several modes with some N-C-N scissoring components could be excited after ionization, and these modes may (beyond the normal mode picture) efficiently couple to other, energetically nearby modes. Tentatively, we therefore attribute the lack of a clear vibrational progression in the PES of urotropine, to the fact that not a single, isolated mode is excited after

ionization. As a consequence, the correlation function decays rapidly and no vibrational fine-structure is seen. Generally, the substitution of the four CH units by N atoms has a considerable impact on the electronic structure of the urotropine cation, which in turn alters its vibrational motion and ultimately also in the PES of urotropine.

Chapter 7

Vibrationally resolved absorption, emission, resonance Raman and photoelectron spectra of radicals and cations derived from adamantane

7.1 Overview

As mentioned in Section 6.1, diamondoids have been intriguing subjects of study for decades due to their favorable properties for the design of optical and electronic devices. Various species of the diamondoid family, pristine and modified, naturally occurring and artificial, have been prepared and measured optically. Theoretical investigations from the perspective of molecular spectroscopy involving electronic transitions also constitute an area of continued research. Publications on derivatives such as radicals and cations of diamondoids, however, are relatively less available, probably because of the more difficult conditions to prepare them. On the other hand, these diamond-like materials are expected to abound in the interstellar medium and contribute to interstellar absorption bands. In regions of space where radiation is strong, small diamondoid cations may be efficiently produced from their neutral parent molecules [94]. Thus study of these cationic species is

helpful for the interpretation of absorption under astrophysical conditions.

In this chapter, we focus on the investigation of the vibronic absorption, emission, resonance Raman and photoelectron spectra involving a few radicals and cations derived from adamantane (Ada): 1-adamantyl and 2-adamantyl radicals (1-Ada$^\bullet$ and 2-Ada$^\bullet$) and cations (1-Ada$^+$ and 2-Ada$^+$). Following Ref. [94], we show in Fig. 7.1 a diagram illustrating the ((U)B3LYP/TZVP) energetics for the formation of radical and cationic species to be considered in this work. The prefix "1" or "2" is in accord with whether the hydrogen atom involved is removed from a CH or CH_2 group. In the following, the radical/formal charge site will be denoted as $C^\bullet/C^+$, carbon atoms next to or still further away from $C^\bullet/C^+$ will be referred to as C_α, C_β, C_γ, ..., and so on.

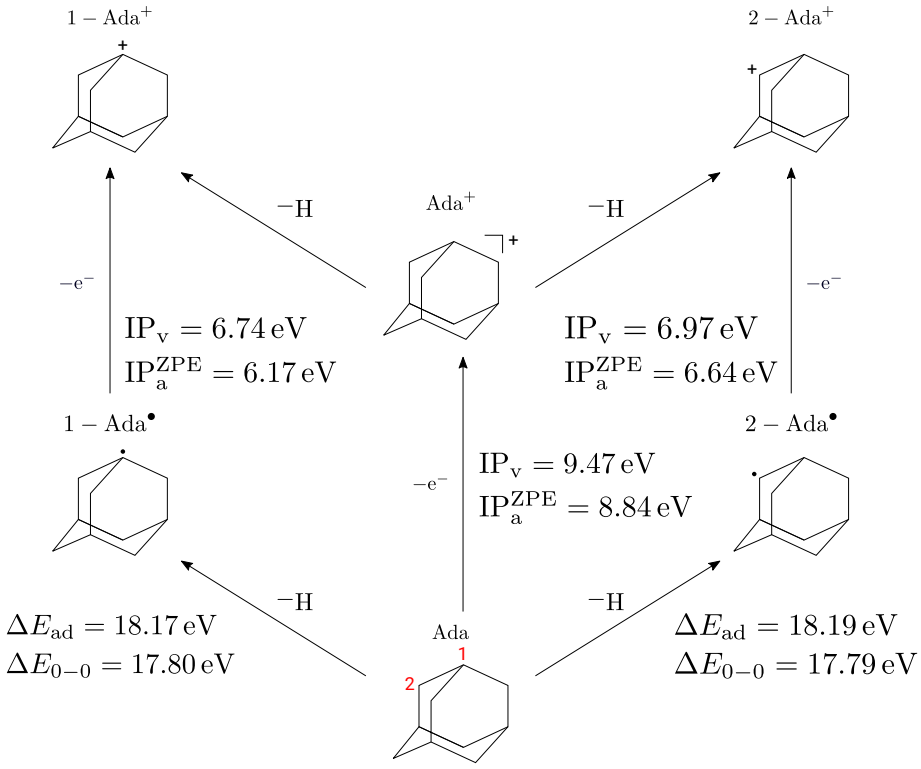

Figure 7.1: A schematic diagram of adamantane (Ada), 1-adamantyl and 2-adamantyl radicals (1-Ada$^\bullet$ and 2-Ada$^\bullet$) and cations (1-Ada$^+$ and 2-Ada$^+$). The numbers "1" and "2" in red attached to adamantane label the two types of carbon atoms, from which hydrogen atoms can be removed, leading to the corresponding 1-adamantyl and 2-adamantyl structures, respectively. $\Delta E_{\rm ad}$ is the adiabatic energy difference between species differing in one hydrogen atom, ΔE_{0-0} the corresponding 0-0 energy difference; $\mathrm{IP_v}$ is the vertical ionization potential and $\mathrm{IP_a^{ZPE}}$ the ZPE-corrected adiabatic ionization potential, for ionization processes. The energies are obtained on the B3LYP/TZVP (for closed-shell species) or UB3LYP/TZVP (for open-shell species) level of theory.

7.2 Methods

Geometry optimization and normal mode analysis were performed for the ground state and relevant excited states on the (U)B3LYP/TZVP DFT and TD-DFT levels following the standard procedure as described in previous chapters. The data for the ground and excited states of the cations were used as input for the program Zzzap to generate the corresponding spectra. For PES, the data for the ground state of the neutral radicals and the ground or excited states of the corresponding cations were used instead. All calculations were done within the IMDHOFAD model. For vertical absorption spectra, the Lorentzian broadening factor $\gamma = 3000\,\mathrm{cm}^{-1}$ was chosen. For vibronic absorption and emission spectra $\Gamma = 200\,\mathrm{cm}^{-1}$, for resonance Raman spectra $\tilde{\Gamma} = 10\,\mathrm{cm}^{-1}$, for REP $\Gamma = 200\,\mathrm{cm}^{-1}$, and for PES $\Gamma = 200\,\mathrm{cm}^{-1}$.

7.3 Results and discussion

7.3.1 Geometries

The optimized ground state structures of 1-Ada$^\bullet$ and 2-Ada$^\bullet$ radicals are shown in Fig. 7.2, with the optimized structural parameters given in Tables 7.1 and 7.2, respectively. 1-Ada$^\bullet$ and 2-Ada$^\bullet$ possess C_{3v} and C_s symmetry, respectively. For the former, the C_3 principal axis is in the "vertical" direction; and for the latter, the σ symmetry plane bisects the C_α-C$^\bullet$-C_α angle, and is also in the "vertical" direction.

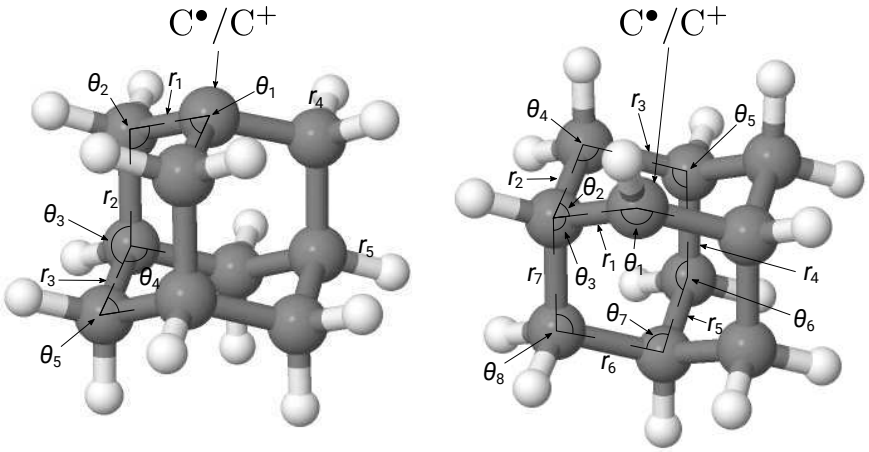

Figure 7.2: The ground state molecular structures of (left) 1-adamantyl and (right) 2-adamantyl radicals/cations, obtained on the (U)B3LYP/TZVP level of theory without symmetry constraints. r and θ refer to bond lengths and bond angles, respectively. The radical/formal charge site is denoted C$^\bullet$/C$^+$, carbon atoms one atom away from (i.e. next to) C$^\bullet$/C$^+$ are referred to as C_α, those two atoms away C_β, ..., and so on, in the text.

Compared with adamantane, the most noticeable structural changes of 1-Ada$^\bullet$ occur at/near the radical site. The C$^\bullet$-C$_\alpha$ bonds r_1 are shortened by 0.038 Å, the "vertical" C$_\alpha$-C$_\beta$ bonds r_2 are elongated by 0.021 Å, the C$_\alpha$-C$^\bullet$-C$_\alpha$ angles θ_1 are increased by 3.6°, and the C$^\bullet$-C$_\alpha$-C$_\beta$ angles θ_2 are decreased by 3.6°. The other bond lengths change by about 0.001 Å, and the other bond angles by less than 0.5°.

Table 7.1: Selected bond distances r (in Å) and angles θ (in degrees) of neutral 1-Ada$^\bullet$ and cationic 1-Ada$^+$ for the specified electronic states, obtained on the (TD-)B3LYP/TZVP level of theory.

bond	1-Ada$^\bullet$	1-Ada$^+$		
parameter	ground state	S_0	S_1	S_3
r_1	1.502	1.453	1.491	1.506
r_2	1.561	1.628	1.558	1.540
r_3	1.541	1.531	1.552	1.536
r_4	1.094	1.088	1.097	1.092
r_5	1.095	1.090	1.090	1.091
θ_1	113.0	117.8	114.2	109.4
θ_2	106.1	98.9	104.9	106.8
θ_3	108.9	108.1	110.2	109.7
θ_4	109.6	111.5	107.0	109.1
θ_5	110.1	109.8	108.4	109.4

For 2-Ada$^\bullet$, the situation is quite similar, i.e., the most significant geometric changes in comparison with adamantane occur at the radical site: the C$^\bullet$-C$_\alpha$ bonds r_1 are shortened by 0.043 Å, and the C$_\alpha$-C$^\bullet$-C$_\alpha$ angle θ_1 is increased by 4.5°. The changes of the other parameters are relatively small.

The optimized ground and relevant excited states structural parameters of 1-Ada$^+$ and 2-Ada$^+$ cations are given in Tables 7.1 and 7.2, respectively. The labeling for the bond parameters is the same as that for the corresponding radicals (Fig. 7.2). The ground state of 1-Ada$^+$ is of C_{3v} symmetry, the first (S_1) and third (S_3) excited singlet states possess C_1 and C_s symmetry, respectively. The ground, first (S_1) and third (S_3) excited singlet states of 2-Ada$^+$ are all of C_s symmetry.

Consider the ground state S_0 of 1-Ada$^+$ and 2-Ada$^+$. The most significant geomet-

ric changes of 1-Ada$^+$ with respect to 1-Ada$^\bullet$ are found at/near the formal charge site, hereafter referred to as C^+, which is the radical site before ionization. The C^+-C_α bonds r_1 are shortened by 0.049 Å, and the C_α-C_β bonds r_2 are elongated by 0.067 Å; the C_α-C^+-C_α angle θ_1 is increased by 4.8°, and the C^+-C_α-C_β angles θ_2 are decreased by 7.2°. For 2-Ada$^+$, the general trend is quite similar, i.e. C^+ is the location at/near which the geometry changes most. The C^+-C_α bonds r_1 are shortened by 0.062 Å, and the C_α-C_β bonds r_2 are elongated by 0.087 Å; the C_α-C^+-C_α angle θ_1 is increased by 5.8°, and the C^+-C_α-C_β angles θ_2 are decreased by 10.5°.

Table 7.2: Selected bond distances r (in Å) and angles θ (in degrees) of neutral 2-Ada$^\bullet$ and cationic 2-Ada$^+$ for the specified electronic states, obtained on the (TD-)(U)B3LYP/TZVP level of theory.

bond	2-Ada$^\bullet$	2-Ada$^+$		
parameter	ground state	S_0	S_1	S_3
r_1	1.497	1.435	1.508	1.508
r_2	1.556	1.643	1.525	1.534
r_3	1.541	1.523	1.519	1.546
r_4	1.540	1.539	1.771	1.539
r_5	1.540	1.539	1.499	1.772
r_6	1.540	1.536	1.546	1.518
r_7	1.549	1.542	1.534	1.525
r_8	1.083	1.089	1.080	1.080
θ_1	114.2	120.0	113.9	113.9
θ_2	108.3	97.8	106.7	110.6
θ_3	109.0	114.8	110.6	106.7
θ_4	109.4	108.1	112.3	108.8
θ_5	109.4	111.1	102.6	111.3
θ_6	109.6	109.8	107.0	107.0
θ_7	109.4	109.8	111.2	115.1
θ_8	109.6	109.9	108.8	112.3

The above results are in reasonable agreement with previous theoretical data obtained

by Yan et al. [115] with the same functional, B3LYP, but a different basis set, DZP++.

Now we consider the excited states of 1-Ada$^+$ and 2-Ada$^+$. The S_1 state of 1-Ada$^+$, in comparison to its ground state S_0, deforms substantially, as the symmetry is totally lost. The C^+-C_α bonds, r_1 in Table 7.1 and the other two not shown in the table, are elongated by at least 0.038 Å, the C_α-C^+-C_α angles are decreased by at least 3.6°, and the C^+-C_α-C_β angles are increased by at least 6°, resulting in a less flat bridgehead "pyramidal" top (C_3C^+). Furthermore, one of the C_β-C_γ bonds in the bottom ring is elongated by an unusual 0.314 Å. The S_3 state of 1-Ada$^+$ changes slightly less in geometry than the S_1 state, but the "pyramidal" top (C_3C^+) is also less flat.

For 2-Ada$^+$, the changes in the geometry of the excited states S_1 and S_3 relative to the ground state S_0 are also large (Table 7.2). The C^+-C_α bond length r_1 is elongated by 0.073 Å and the C_α-C^+-C_α angle θ_1 is decreased by 6.1° for both excited states. The bond length r_2 is decreased by about 0.11 Å, and r_4 (r_5) increased by 0.23 Å for S_1 (S_3). The bond angle α_2 is increased by 8.9° (12.8°) for S_1 (S_3).

A comparison can also be made between the geometries of the S_1 state of the cation and the ground state of the corresponding neutral radical. It is found that for 1-Ada$^\bullet$ the bond r_3 and bond angle θ_4 change the most upon ionization to S_1, by 0.011 Å and −2.6°, respectively, and similarly for 2-Ada$^\bullet$ the geometric parameters (with the largest values of change) are the bond r_4 (0.231 Å) and the bond angle θ_5 (−6.6°).

7.3.2 Vertical absorption spectra

The vertical excitation energies of the first 20 excited states of 1-Ada$^+$ and 2-Ada$^+$ are presented in Table 7.3, and the broadened vertical absorption spectra with a Lorentzian width of 3000 cm^{-1} are shown in Fig. 7.3. It is easily observed that several (nearly) degenerate states occur in the case of 1-Ada$^+$, in contrast to 2-Ada$^+$. This is due to the higher symmetry of 1-Ada$^+$, giving rise to more degenerate excited states. Both cations feature a weakly allowed transition at about 4 eV, followed by several relatively intense transitions at higher energies. The absorption peaks of 2-Ada$^+$ are overall red shifted with respect to those of 1-Ada$^+$ by about 1 eV.

The qualitative features of the spectra are in quite good agreement with simulations performed in Ref. [94], where they also measured the spectrum of FUV-irradiated adamantane in Ne matrix. Under experimental conditions, both cations were produced and estimated to be about 1:1 in ratio. In the experiment, besides a strong peak at 223.5 nm (5.55 eV), three weak features extending from 250 to 350 nm (4.96 to 3.54 eV) were also observed. The former was assigned to the $S_0 \rightarrow S_2$ transition (transition from S_0 to the doubly degenerate S_3 in our calculation) for 1-Ada$^+$, and the latter were assumed to be contributions from the $S_0 \rightarrow S_1$ transition for 1-Ada$^+$ and transitions to the first four

Table 7.3: Vertical excitation energies ΔE_{vert} and oscillator strengths f of 1-Ada$^+$ and 2-Ada$^+$, for the first 20 transitions, on the TD-B3LYP/TZVP level of theory. Energies are in eV.

State	1-Ada$^+$		2-Ada$^+$	
	ΔE_{vert}	f	ΔE_{vert}	f
1	4.3480	0.0012	3.7390	0.0082
2	4.3488	0.0012	3.9190	0.0001
3	5.1987	0.0463	3.9636	0.0145
4	5.1991	0.0463	4.6950	0.0304
5	5.5990	0.0000	4.9375	0.0125
6	5.9392	0.0058	5.0853	0.0045
7	5.9399	0.0058	5.3522	0.0006
8	6.2410	0.0921	6.2371	0.0598
9	7.2560	0.0580	6.6141	0.0186
10	7.2565	0.0579	6.7974	0.0013
11	7.4932	0.0000	6.9007	0.0421
12	7.5377	0.0009	6.9615	0.0033
13	7.5381	0.0009	7.4783	0.0224
14	8.4878	0.0349	8.0229	0.0006
15	8.6928	0.0023	8.2215	0.0585
16	8.6938	0.0023	8.2728	0.0007
17	8.9254	0.0235	8.3369	0.0080
18	9.0034	0.0025	8.3871	0.0156
19	9.0035	0.0025	8.5352	0.0046
20	9.2684	0.0000	8.5809	0.0115

excited states for 2-Ada$^+$ (transitions to the doubly degenerate first two excited states for 1-Ada$^+$ and transitions to the first three excited states for 2-Ada$^+$ in our case). The quantitative differences in energies and oscillator strengths between our results and those in Ref. [94] can be attributed to the theoretical models used. The evaluation of the ratio of both cations produced can possibly also be facilitated by their resonance Raman spectra, which will be discussed in Section 7.3.4.

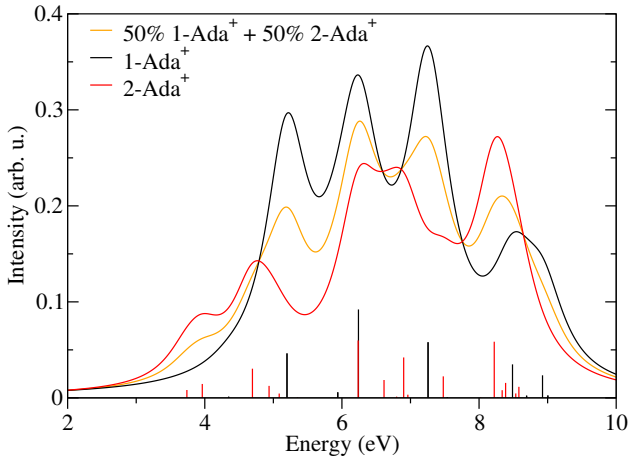

Figure 7.3: The vertical absorption spectra broadened with a Lorentzian width of 3000 cm^{-1} for 1-Ada$^+$ and 2-Ada$^+$, and corresponding oscillator strength sticks.

7.3.3 Vibronic absorption and emission spectra

The vibronic spectra for the first excited state S_1 of 1-Ada$^+$ and 2-Ada$^+$ are shown in Fig. 7.4, together with their absorption correlation functions. A common feature is that these spectra are broad peaks without clear vibrational structure. This phenomenon is often observed if the structure of the excited state involved is largely different from the ground state geometry. This is indeed the case, as the difference between the geometry of the S_1 and the ground states for each cation is nontrivial. For instance, the bond r_2 decreases by 0.07 Å(4.3%) and the bond angle θ_2 increases by 6° (6.1%), with respect to the ground state of 1-Ada$^+$. For 2-Ada$^+$, the observation is similar.

From the perspective of the absorption correlation function, we can get more insight into the broad and smooth feature of the vibronic spectra of the cations. The correlation functions decay very fast initially, with no obvious recurrences. The fast initial decay determines the overall width of the spectrum according to the relation $\Delta E \sim 1/\tau$ (up to a constant), i.e. the faster it takes for the absolute value of the correlation function to

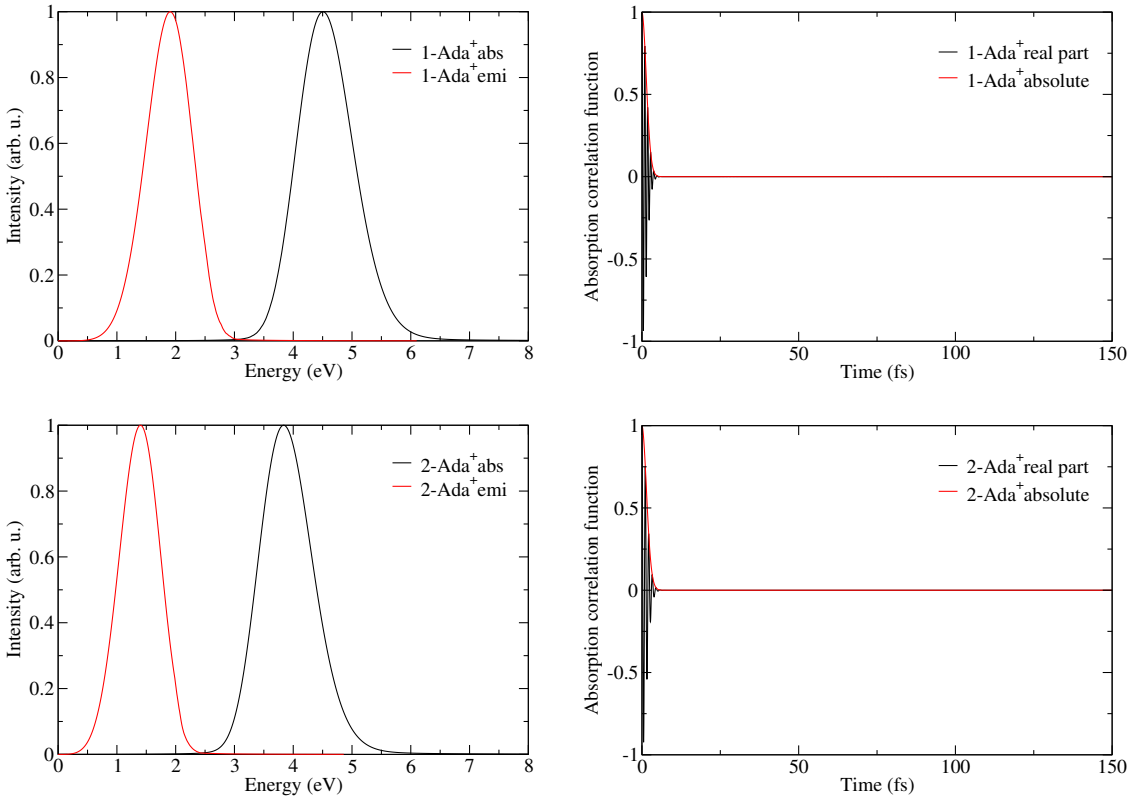

Figure 7.4: Upper left: vibronic absorption and emission spectra of 1-Ada$^+$ for S_1 state. Upper right: absorption correlation function for upper left. Lower left: vibronic absorption and emission spectra of 2-Ada$^+$ for S_1 state. Lower right: absorption correlation function for lower left.

decrease to $1/e$ for the first time, the larger the width of the envelop of the spectrum. The period of fast oscillations in the correlation functions reflects the energy difference between the ground and excited states, which determines the main peak position. For example, the period of fast oscillations for S_1 of 1-Ada$^+$ is about 0.90 fs, which corresponds to about 4.6 eV where the main peak lies. The vertical transition energy for the first excited state S_1 (Table 7.3) is 0.25 eV lower than the maximum peak position. In principle, the period of recurrences determines the spacing of the vibrational fine structures in the spectrum. Since there are no obvious fine structures in the spectra of both the cations, we do not analyse them further. The emission spectra can be analysed similarly, and they are nearly mirror images of the absorption spectra with respect to the point of overlap.

When the absorption correlation functions are locally enlarged in the region near the x-axis, recurrences which do not show up in Fig. 7.4 do appear but with complicated patterns. For example, in the absroption correlation function of 1-Ada$^+$ (Fig. 7.5), it seems that there are more than one pattern of recurrences, i.e. recurrences with different

periods occur which corresponds to different modes. This means there is not only one single mode contributing to the absorption spectrum, but several modes make somewhat balanced contributions to the spectrum, explaining the smoothness of the spectrum.

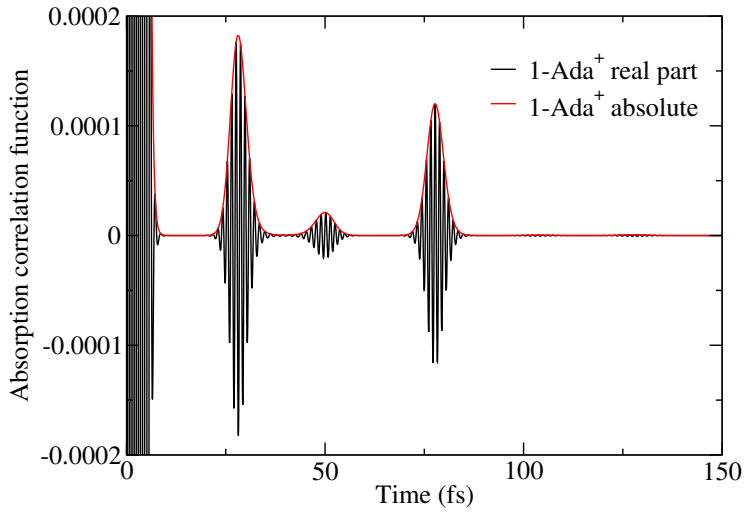

Figure 7.5: A close-up of the absorption correlation function for the S_1 state of 1-Ada$^+$.

7.3.4 Resonance Raman spectra

The resonance Raman spectra involving S_0 and S_1 states for 1-Ada$^+$ and 2-Ada$^+$ are shown in Fig. 7.6. The peaks for 1-Ada$^+$ are overall red-shifted with respect to 2-Ada$^+$. The spectra of both cations show little dependence on the excitation energy, i.e. the relative intensities of the peaks do not change as the excitation energy changes, although the absolute intensities do change. This observation is also clearly seen in the REP (Fig. 7.6). For 1-Ada$^+$, modes 1, 36 and 41 increase or decrease "at the same pace" and all attain the maximum intensity at around 4.65 eV. Other modes behave similarly. Similar statements hold for 2-Ada$^+$. Therefore, the resonance Raman spectra of 1-Ada$^+$ and 2-Ada$^+$ can be considered as their "fingerprints" and used to distinguish them or determine their ratio if they exist in a mixture.

7.3.5 Photoelectron spectra

The simulated lowest-energy band of the PES spectra for 1-Ada$^\bullet$ and 2-Ada$^\bullet$ are shown in Fig. 7.7, along with the corresponding experimental spectra [116]. For 1-Ada$^\bullet$, the simulated ZPE-corrected adiabatic IP is 6.17 eV, which is 0.04 eV smaller than the experimentally determined value of 6.21 eV. For comparison both the spectra have been aligned at the experimental adiabatic IP. The simulated vertical IP, however, is 6.74 eV and larger than the experimental value of 6.36 eV by 0.38 eV. For 2-Ada$^\bullet$, both the IP_a^{ZPE} (6.64 eV)

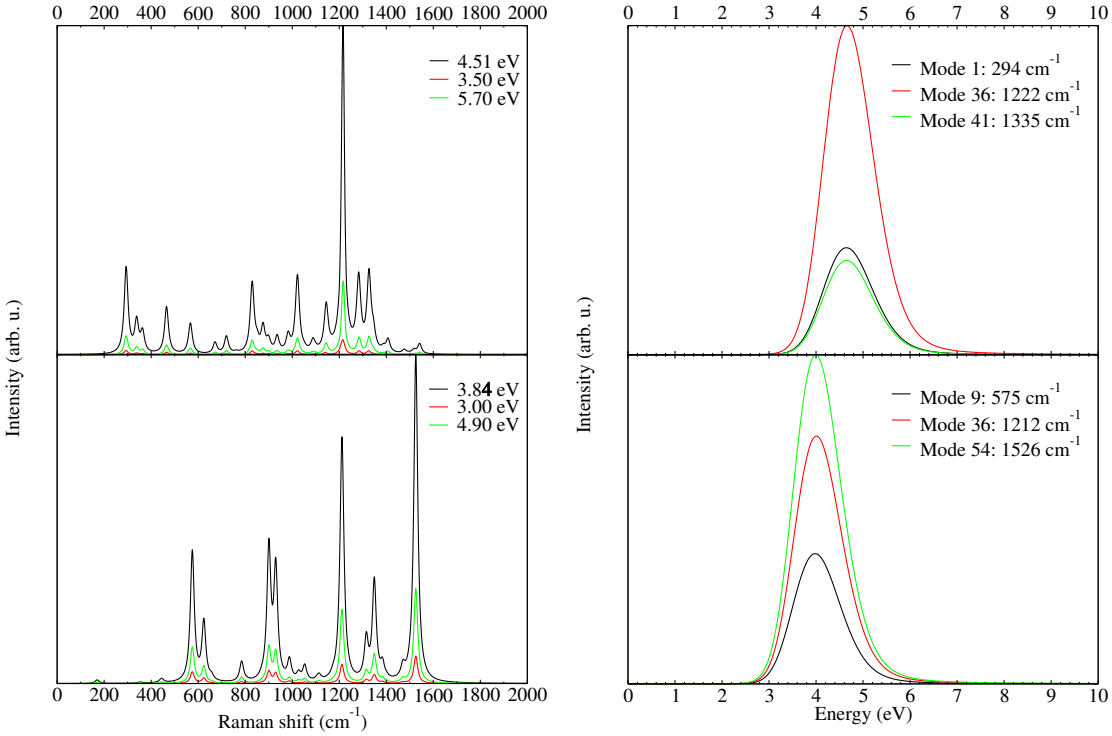

Figure 7.6: The resonance Raman spectra for three different excitation energies involving the S_1 state of (upper left) 1-Ada$^+$ and (lower left) 2-Ada$^+$, broadened with a Lorentzian factor of $10\,\mathrm{cm}^{-1}$, and the Raman excitation profile for three different modes involving the S_1 state of (upper right) 1-Ada$^+$ and (lower right) 2-Ada$^+$, broadened with a Lorentzian factor of $200\,\mathrm{cm}^{-1}$.

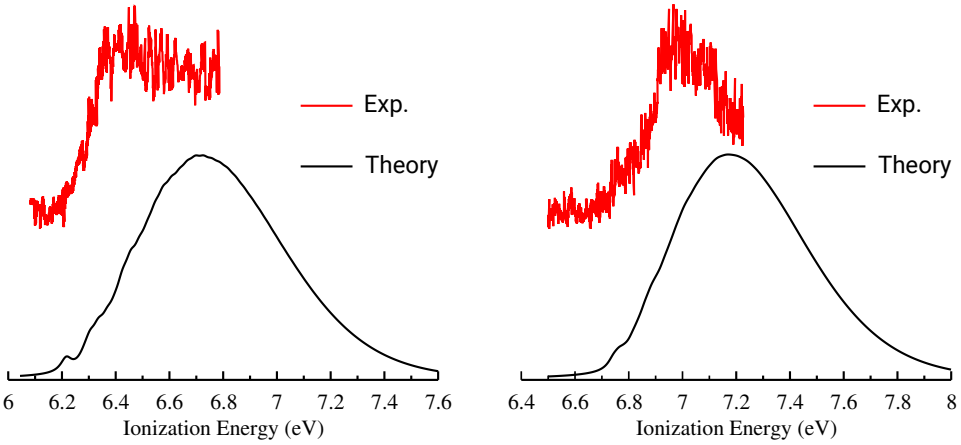

Figure 7.7: The lowest-energy PES band of (left) 1-Ada$^\bullet$ and (right) 2-Ada$^\bullet$. The experimental data is adapted from Ref. [116].

and IP_v (6.97 eV) agree quite well with the corresponding experimental values, 6.73 eV and 6.99 eV, respectively, with an underestimation of less than 0.1 eV. The first PES band for both radicals is rather structureless. It should be noted that under the experimental conditions, a portion of the 1-Ada$^\bullet$ radicals decomposes to smaller radicals which have slightly higher adiabatic ionization potentials [116]. The higher energy portion (≥ 6.5 eV) of the experimental PES band may be complicated by these thermal decomposition product radicals.

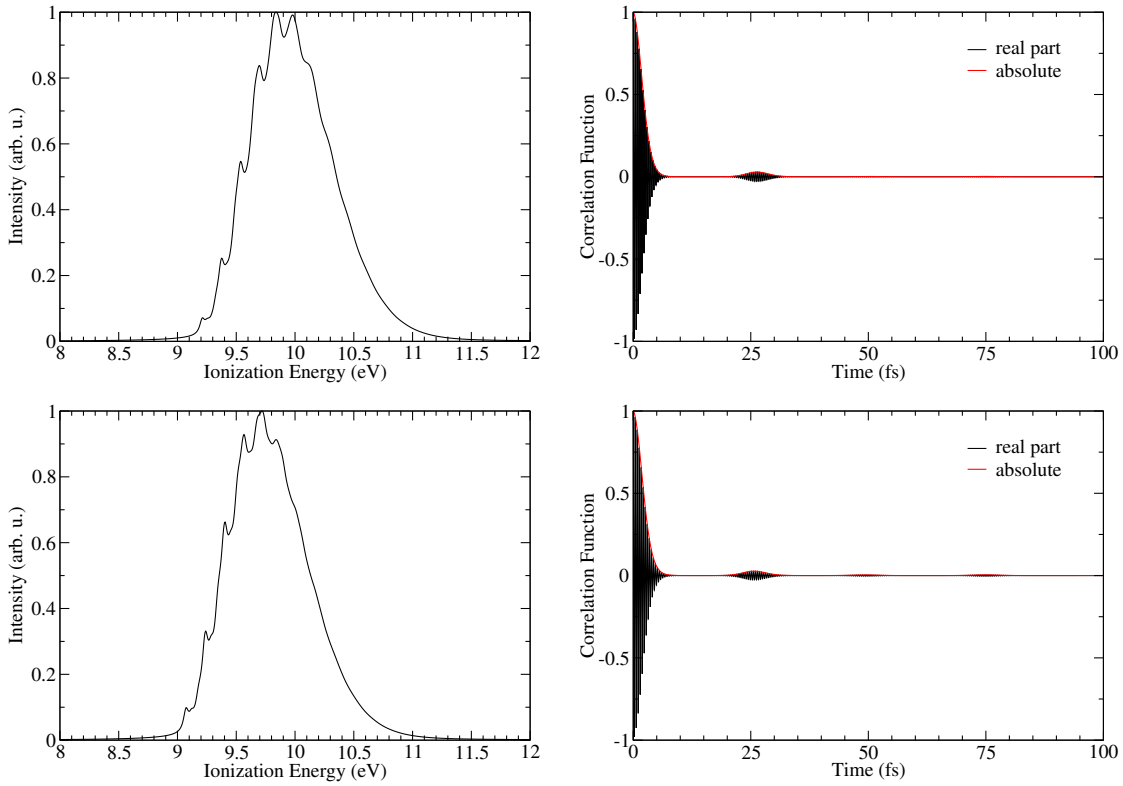

Figure 7.8: Upper left: the simulated second PES band of 1-Ada$^\bullet$; Upper right: the corresponding correlation function of 1-Ada$^\bullet$. Lower left: the simulated second PES band of 2-Ada$^\bullet$; Lower right: the corresponding correlation function of 2-Ada$^\bullet$.

Now consider the second PES band for 1-Ada$^\bullet$ and 2-Ada$^\bullet$ in Fig. 7.8. The ZPE-corrected adiabatic IP is determined to be 9.21 eV for 1-Ada$^\bullet$ and 9.07 eV for 2-Ada$^\bullet$, and the vertical IP is 9.81 eV for 1-Ada$^\bullet$ and 9.63 eV for 2-Ada$^\bullet$. For the second PES band, there is a clear vibrational progression, ~ 1323.67 cm^{-1} for 1-Ada$^\bullet$ and ~ 1338.01 cm^{-1} for 2-Ada$^\bullet$, corresponding to a recurrence time of ~ 25.20 fs and ~ 24.93 fs, respectively. Relevant normal modes can be found in the region $\sim 1323.67 \pm 100$ cm^{-1} for 1-Ada$^+$ (S_1) and $\sim 1338.01 \pm 100$ cm^{-1} for 2-Ada$^+$ (S_1) that facilitate the geometric deformation. In particular, in the regions mention above, the modes with frequencies 1226.53 cm^{-1} (featuring C^+-C_α, i.e. r_1, bond stretching, and the θ_4 bond angle scissoring), 1308.08

cm^{-1} (featuring the r_1 and r_3 bond stretching), and 1363.44 cm^{-1} (featuring the r_1 bond stretching and the θ_4 bond angle scissoring) conform to the geometric change for 1-Ada$^{\bullet}$, while the modes with frequencies 1221.06 cm^{-1} (the $\mathrm{C}\overset{r_4}{-}\mathrm{C}\overset{r_5}{-}\mathrm{C}$ asymmetric stretching) and 1240.26 cm^{-1} (a vibration involving the angle θ_5 changing) play a major role in inducing the geometric change for 2-Ada$^{\bullet}$.

Chapter 8

Summary and outlook

8.1 Summary

The Heller-type time-dependent correlation function approach in combination with linear-response, time-dependent density functional theory, within the framework of the harmonic and Condon approximations, was applied to investigate the vibrationally resolved absorption, emission, resonance Raman, and photoelectron spectra of selected organic molecules, associated radicals and cations. A two-state model was also adopted to simplify the calculations. Two sets of normal modes can be obtained, one for the electronic ground and the other for the electronically excited state. Three models within the harmonic approximation exist to related both sets of normal modes. The most complete of them, the IMDHOFAD model was used throughout this work. A home-built program, Zzzap, was developed to facilitate the calculations of spectra from the optimized geometries of molecules and the corresponding normal modes obtained from Gaussian 09.

This approach was used to study the molar absorptivities and vibronic absorption and emission spectra of perylene and several of its N-derivatives (azaperylenes). Lowest-energy absorption and emission bands are due to allowed $\pi \leftrightarrow \pi^*$ transitions, which change the bonding/antibonding character between C-C and C-N bonds in the center of the molecule. The corresponding geometric changes cause prominent vibronic fine-structures in absorption and emission bands, which can be traced back to C-C (C-N) vibrations in the molecular centers. It was found that the presence of nitrogen atom(s) has a negligible impact on the structure of the molecules, while the spectra are influenced by, in particular, the number of nitrogen atoms rather than their position. This implies that N-substitution can be used to fine-tune the optical properties of these perylene-based molecules. Solvent effects were studied by comparing gas phase to solvent (MeCN) calculations, using linear-response and state-specific PCM models. The polar solvent is predicted to red-shift

the lowest bright excitation by a value in the order of 10 nm for all molecules, except for perylene, which is largely unaffected. Furthermore, for one azaperylene, **1,6-A** (for which experiment hints at a clear red-shift/broadening of spectra [62, 63]), the effect of a possible dimer formation on spectral features was studied. Using simple dispersion-corrected TD-DFT methods, several stacked dimers of similar energy were found whose vertical absorption spectra are red-shifted in their onset with respect to the monomer, and also broadened, due to excitonic effects. We expect dimer formation to be important when the concentration of chromophores in solution is high.

The same approach was used to simulate the gas phase vibronic absorption, emission and resonance Raman spectra of a novel molecule (denoted Ada-py for convenience) consisting of adamantane bridged to pyrene, for the lowest bright transition $S_0 \rightarrow S_1$. The absorption and emission spectral forms are in fairly good agreement with experimental data obtained in cyclohexane solvent, though in experiment the absorption and emission peaks are red-shifted and the maximum intensity for absorption is shifted from the 0-0 to a higher-energy subpeak, which were attributed to solvent effects. Raman and resonance Raman spectra were calculated. The former is in very good agreement with the experimental spectrum. For the latter, the intensities of simulated peaks in the low frequency region closely resemble the experimental data, however, the peak which is predicted to be enhanced most is red-shifted by $\sim 100\,\mathrm{cm}^{-1}$ with respect to the experimental counterpart. The difference was attributed to the possible influence of the crystal environment for the experiment.

Then the approach for vibronic absorption spectra was extended to study ionization processes for three lower (pristine and modified) diamondoids. The simulated lowest-energy band of the vibronic photoelectron spectra for these species agree quite well with experimental spectra, except for some high-energy satellite peaks, which were attributed to the many body effects beyond the Born-Oppenheimer approximation in Ref. [98]. The relation between the geometric distortions and Jahn-Teller effect was also discussed. The Heller-type correlation function approach to photoelectron spectroscopy was shown to be promising.

Finally, all of the above procedures were applied to investigate the optical properties of a few adamantane-derived radicals and cations. In particular, we simulated higher-energy bands of the vibronic photoelectron spectra for the radicals. It was found that the vibronic absorption and emission of the cations are structureless. The lowest-energy bands for the photoelectron spectra of the radicals are rather smooth, in qualitative agreement with experimental data, though the ionization potentials differ by a few tenths of an eV. The second bands in the photoelectron spectra are much more "regular", and the contributing modes are discussed. The study can be used for predicative purposes.

The work presented in Chapters 5 and 7 are being prepared for possible publication.

8.2 Outlook

Though the Heller formalism has been shown to be quite reliable in most cases, it has more capabilities than was shown. For example, the nonradiative intersystem crossing (ISC) processes can be conveniently treated in the time-dependent correlation function approach [117]. Another type of radiationless processes, internal conversion (IC), can be dealt with similarly [118]. More specifically, the IC rate coupling two electronic states in the Condon approximation and in the IMDHOFAD model is expressed as

$$k_{\mathrm{ic}} = \sum_{k,l=1}^{3N-6} k_{\mathrm{ic},kl}, \tag{8.1}$$

where

$$k_{\mathrm{ic},kl} = \frac{1}{\hbar^2} R_{kl} \int_{-\infty}^{\infty} [\exp(i\Delta E_{\mathrm{ad}} t) Z_{\mathrm{i}\nu}^{-1} \rho_{\mathrm{ic},kl}(t,T)]\, dt. \tag{8.2}$$

The indices k, l denote normal modes, R_{kl} are the non-adiabatic coupling matrix elements between the initial and final electronic states, ΔE_{ad} is the adiabatic minimum energy separation, $Z_{\mathrm{i}\nu}$ is the thermal partition function, and $\rho_{\mathrm{ic},kl}$ is the thermal vibration correlation function. The expressions for all these quantities can be found in Ref. [118] and references therein. In the future, it is desirable to implement both of these processes in Zzzap. In fact, the IC implementation is already done for diatomic molecules, and generalization to polyatomic molecules is under way.

Besides, the approximations we have made in this work are quite ideal, i.e. we have neglected the temperature effects, the anharmonicity, and the coordinate dependence of the transition dipole moment. Our toolkit can be improved by, for example, including the linear term in the Taylor expansion of the transition dipole moment with respect to the coordinate, which is known as the Herzberg-Teller term.

Acknowledgement

This PhD work is finished under the supervision of Prof. Peter Saalfrank and Dr. Thomas Körzdörfer. I am sincerely thankful for the knowledge and patience of Prof. Saalfrank in guiding me in research, and much more beyond work. Dr. Körzdörfer did constructive collaboration with me. Also, this work could not have finished without the help of and discussion with other members from the Saalfrank group. Dr. Foudhil Bouakline is always a good choice for fruitful discussions, and the PhD students are willing to share their knowledge and help each other out.

I also appreciate the financial support from Deutsche Forschungsgemeinschaft (DFG) through the Cluster of Excellence 314 Unifying Concepts in Catalysis, coordinated by the Technical University of Berlin.

Last but not least, my family is a constant source of support. No words can describe my gratitude.

Appendix A

Analytical expressions for absorption, emission and resonance Raman correlation functions in the IMDHOFAD model

A.1 Absorption auto-correlation function

The absorption auto-correlation function in the IMDHOFAD model at $T = 0\,\mathrm{K}$ can be expressed as

$$\mathrm{C}_{\mathrm{abs}}^{\mathrm{IMDHOFAD}}(t) = \left(\frac{1}{2}\right)^{1/2} \sqrt{\frac{1}{\det \underline{\underline{A}}}} \exp[-\underline{p}^{\mathrm{T}} \cdot (\underline{\underline{A}}^{-1}/4) \cdot \underline{p}] \exp(i\gamma), \tag{A.1}$$

where

$$\underline{\underline{A}} = \underline{\underline{A}}_0 + \underline{\underline{A}}_t, \tag{A.2}$$

$$\underline{p} = \underline{p}_t - 2i\underline{\underline{A}}_t \cdot \underline{q}_t, \tag{A.3}$$

$$\gamma = i\underline{q}_t^{\mathrm{T}} \cdot \underline{\underline{A}}_t \cdot \underline{q}_t - \underline{p}_t^{\mathrm{T}} \cdot \underline{q}_t + \gamma_t, \tag{A.4}$$

$$\underline{\underline{A}}_t = \frac{1}{2i}\underline{\underline{P}}_Z \cdot \underline{\underline{Z}}^{-1}, \tag{A.5}$$

$$\underline{\underline{A}}_0 = \frac{1}{2}, \tag{A.6}$$

$$\underline{p}_t = (\underline{\underline{J}}^{-1})^{\mathrm{T}} \cdot \underline{\underline{S}} \cdot \underline{\underline{J}}^{-1} \cdot \underline{\Delta}, \tag{A.7}$$

$$\underline{q}_t = -\underline{\underline{J}} \cdot \underline{\underline{C}} \cdot \underline{\underline{J}}^{-1} \cdot \underline{\Delta} + \underline{\Delta}, \tag{A.8}$$

$$\gamma_t = \frac{i}{2}\ln(\det\underline{\underline{Z}}) + \frac{1}{2}\underline{p}_t^{\mathrm{T}} \cdot (\underline{q}_t - \underline{\Delta}), \tag{A.9}$$

$$\underline{\underline{Z}} = \underline{\underline{J}}(i\underline{\underline{S}} \cdot \underline{\underline{J}}^{\mathrm{T}} + \underline{\underline{C}} \cdot \underline{\underline{J}}^{-1}). \tag{A.10}$$

Here $\underline{\underline{C}}$ and $\underline{\underline{S}}$ are diagonal matrices with diagonal elements $\cos(\omega_m^{\mathrm{f}} t)$ and $\sin(\omega_m^{\mathrm{f}} t)$, respectively, and ω_m^{f} is the vibrational frequency of the m^{th} normal mode in the final electronic state, $\underline{\underline{J}}$ is the Duschinsky matrix, $\underline{\Delta}$ is the dimensionless origin shift.

A.2 Emission auto-correlation function

The expressions for emission are similar to those for absorption in Section A.1, but it should be noted that the initial and final electronic states now are the excited state and the ground state, respectively, opposite to absorption.

A.3 Resonance Raman cross-correlation function

The cross-correlation function for the $0 \rightarrow 1$ resonance Raman scattering in the IMDHO-FAD model is

$$\underline{\mathrm{C}}_{\mathrm{rR}}^{\mathrm{IMDHOFAD}}(t) = \left(\frac{1}{2}\right)^{1/2} \sqrt{\frac{1}{\det\underline{\underline{A}}}} \exp[-\underline{p}^{\mathrm{T}} \cdot (\underline{\underline{A}}^{-1}/4) \cdot \underline{p}] \exp(i\gamma)(\frac{\underline{\underline{A}}^{-1} \cdot \underline{p}}{i}), \tag{A.11}$$

where all the necessary quantities have been defined in Section A.1.

As in the case of absorption, we have assumed that the temperature is absolute zero, and the final vibrational state after photon scattering is higher in energy than the vibrational ground state by one quantum, i.e. we are treating the $0_1 0_2 \cdots 0_m \cdots 0_{3N-6} \rightarrow 0_1 0_2 \cdots 1_m \cdots 0_{3N-6}$ scattering, where m denotes the mode scattering the photon. It should be noted that due to the presence of the vector $\frac{\underline{\underline{A}}^{-1} \cdot \underline{p}}{i}$ in the above expression, the resonance Raman cross-correlation function is actually a vector. Therefore, resonance Raman scattering intensity is not only a function of the incident light frequency, but also depends on the frequency of the modes (or equivalently, the frequency of the scattered

light). Keeping the excitation frequency fixed, we can compute the resonance Raman spectrum, i.e. the Raman intensity as a function of vibrational mode. Alternatively, Fourier transforming the components of the vector $\underline{C}_{\mathrm{rR}}^{\mathrm{IMDHOFAD}}(t)$ gives rise to the Raman excitation profile, i.e. a collection of spectra, one for each mode as a function of the excitation frequency.

Appendix B

Higher vertical excitation energies for the perylene series

In what follows, we list higher excitation energies for the perylene series in gas phase and in MeCN (LR-PCM), and for the **1,6-A** dimers.

Table B.1: Vertical excitation energies ΔE_{vert} and oscillator strengths f of the perylene series in the gas phase, for the first 20 transitions, on the TD-B3LYP/TZVP level of theory. Energies are in eV.

State	**P**		**1-A**		**1,6-A**		**1,7-A**		**1,12-A**		**1,6,7-A**		**1,6,7,12-A**	
	ΔE_{vert}	f	ΔE_{vert}	f	ΔE_{vert}	f	ΔE_{vert}	f	ΔE_{vert}	f	ΔE_{vert}	f	ΔE_{vert}	f
1	2.82	0.35	2.86	0.36	2.93	0.36	2.89	0.36	2.91	0.36	2.97	0.37	2.80	0.00
2	3.62	0.00	3.69	0.01	3.41	0.00	3.53	0.00	3.16	0.00	3.05	0.00	3.05	0.37
3	3.96	0.00	3.70	0.00	3.69	0.02	3.74	0.00	3.53	0.00	3.41	0.00	3.18	0.00
4	4.01	0.01	3.96	0.00	3.93	0.00	3.75	0.00	3.76	0.00	3.72	0.00	3.49	0.00
5	4.05	0.00	4.05	0.01	4.03	0.02	3.98	0.00	3.99	0.00	3.85	0.00	3.66	0.00
6	4.20	0.00	4.12	0.00	4.05	0.00	4.14	0.00	4.11	0.00	4.04	0.00	3.72	0.00
7	4.51	0.00	4.20	0.00	4.21	0.00	4.15	0.00	4.18	0.00	4.11	0.00	4.07	0.00
8	4.53	0.00	4.58	0.00	4.29	0.01	4.24	0.00	4.25	0.00	4.19	0.00	4.17	0.00
9	4.84	0.31	4.65	0.02	4.63	0.00	4.65	0.00	4.65	0.00	4.43	0.00	4.28	0.00
10	5.37	0.01	4.90	0.25	4.70	0.00	4.73	0.00	4.66	0.00	4.48	0.00	4.35	0.00
11	5.52	0.08	5.02	0.00	4.82	0.08	4.91	0.26	4.74	0.00	4.78	0.01	4.58	0.00
12	5.56	0.04	5.38	0.07	5.01	0.11	5.01	0.00	4.90	0.00	4.87	0.00	4.60	0.00
13	5.69	0.00	5.46	0.00	5.23	0.05	5.16	0.00	4.94	0.25	4.90	0.02	4.93	0.00
14	5.70	0.00	5.47	0.00	5.27	0.00	5.40	0.00	5.07	0.00	5.00	0.18	4.95	0.00
15	5.74	0.00	5.58	0.08	5.31	0.00	5.42	0.13	5.25	0.00	5.06	0.00	5.02	0.00
16	5.74	0.00	5.68	0.10	5.37	0.06	5.56	0.00	5.35	0.00	5.16	0.00	5.02	0.00
17	5.75	0.00	5.69	0.00	5.56	0.00	5.58	0.13	5.42	0.14	5.24	0.00	5.04	0.00
18	5.77	0.00	5.75	0.00	5.61	0.10	5.65	0.00	5.47	0.00	5.30	0.00	5.04	0.19
19	5.84	0.08	5.75	0.00	5.61	0.09	5.66	0.00	5.60	0.01	5.36	0.17	5.04	0.00
20	5.92	0.00	5.86	0.00	5.70	0.00	5.71	0.00	5.60	0.12	5.44	0.00	5.27	0.00

Table B.2: Vertical excitation energies ΔE_{vert} and oscillator strengths f of the perylene series in MeCN (LR-PCM), for the first 20 transitions, on the TD-B3LYP/TZVP level of theory. Energies are in eV.

State	**P**		**1-A**		**1,6-A**		**1,7-A**		**1,12-A**		**1,6,7-A**		**1,6,7,12-A**	
	ΔE_{vert}	f	ΔE_{vert}	f	ΔE_{vert}	f	ΔE_{vert}	f	ΔE_{vert}	f	ΔE_{vert}	f	ΔE_{vert}	f
1	2.82	0.35	2.85	0.35	2.92	0.36	2.87	0.36	2.85	0.34	2.93	0.36	3.00	0.36
2	3.61	0.00	3.69	0.01	3.50	0.00	3.62	0.00	3.42	0.00	3.22	0.00	2.96	0.00
3	3.94	0.00	3.83	0.00	3.68	0.02	3.74	0.00	3.74	0.00	3.63	0.00	3.37	0.00
4	4.02	0.01	3.96	0.00	3.92	0.00	3.84	0.00	3.83	0.00	3.69	0.00	3.61	0.00
5	4.07	0.00	4.05	0.01	4.03	0.02	3.96	0.00	3.98	0.00	3.96	0.00	3.66	0.00
6	4.20	0.00	4.11	0.00	4.13	0.00	4.13	0.00	4.12	0.00	4.01	0.01	3.90	0.00
7	4.52	0.00	4.20	0.00	4.19	0.00	4.15	0.00	4.14	0.00	4.09	0.00	4.01	0.00
8	4.53	0.00	4.58	0.00	4.29	0.01	4.24	0.00	4.25	0.02	4.17	0.00	4.14	0.00
9	4.84	0.31	4.64	0.02	4.71	0.00	4.65	0.00	4.64	0.01	4.42	0.01	4.28	0.00
10	5.37	0.00	4.89	0.25	4.71	0.00	4.74	0.00	4.73	0.00	4.64	0.00	4.52	0.00
11	5.52	0.08	5.15	0.00	4.81	0.09	4.90	0.26	4.91	0.26	4.77	0.02	4.61	0.00
12	5.56	0.04	5.38	0.07	5.01	0.09	5.09	0.00	4.93	0.00	4.89	0.03	4.77	0.00
13	5.68	0.00	5.46	0.00	5.21	0.05	5.25	0.00	5.20	0.00	4.98	0.16	4.95	0.00
14	5.69	0.00	5.59	0.09	5.35	0.00	5.40	0.15	5.39	0.00	5.10	0.00	5.00	0.00
15	5.71	0.00	5.61	0.00	5.35	0.06	5.49	0.00	5.42	0.15	5.26	0.00	5.01	0.18
16	5.73	0.00	5.66	0.00	5.40	0.00	5.57	0.14	5.55	0.00	5.31	0.00	5.14	0.00
17	5.75	0.00	5.68	0.10	5.60	0.11	5.60	0.00	5.60	0.13	5.33	0.18	5.21	0.00
18	5.83	0.08	5.75	0.00	5.61	0.09	5.67	0.00	5.65	0.00	5.44	0.00	5.22	0.00
19	5.93	0.00	5.89	0.00	5.66	0.00	5.72	0.01	5.71	0.00	5.49	0.00	5.23	0.00
20	5.93	0.00	5.90	0.00	5.68	0.00	5.76	0.00	5.73	0.01	5.56	0.13	5.32	0.23

Table B.3: Vertical excitation energies ΔE_{vert} and oscillator strengths f of the dimers of **1,6-A** in the gas phase, for the first 20 transitions, on the TD-B3LYP/TZVP level of theory. Energies are in eV (nm).

State	Dimer a		Dimer b		Dimer c	
	ΔE_{vert}	f	ΔE_{vert}	f	ΔE_{vert}	f
1	2.4472 (506.63)	0.0432	2.5373 (488.65)	0.0021	2.4562 (504.77)	0.0612
2	2.4872 (498.49)	0.0229	2.5582 (484.65)	0.0008	2.4779 (500.36)	0.0002
3	2.8410 (436.42)	0.0008	2.8086 (441.45)	0.0725	2.8249 (438.90)	0.0015
4	3.0657 (404.43)	0.4713	2.9322 (422.83)	0.3967	3.0642 (404.62)	0.4708
5	3.3008 (375.62)	0.0026	3.3923 (365.49)	0.0016	3.3632 (368.65)	0.0000
6	3.3571 (369.32)	0.0010	3.4319 (361.27)	0.0010	3.3668 (368.25)	0.0023
7	3.3844 (366.34)	0.0002	3.6189 (342.60)	0.0161	3.4739 (356.90)	0.0017
8	3.6313 (341.43)	0.0086	3.6217 (342.34)	0.0063	3.5305 (351.18)	0.0100
9	3.7415 (331.37)	0.0065	3.7462 (330.96)	0.0034	3.6869 (336.28)	0.0006
10	3.7822 (327.81)	0.0006	3.7563 (330.07)	0.0034	3.7760 (328.34)	0.0004
11	3.8047 (325.87)	0.0060	3.7964 (326.58)	0.0014	3.7913 (327.02)	0.0137
12	3.8300 (323.72)	0.0019	3.8582 (321.35)	0.0002	3.8440 (322.54)	0.0034
13	3.8898 (318.74)	0.0010	3.8739 (320.05)	0.0002	3.8663 (320.68)	0.0005
14	3.8940 (318.40)	0.0034	3.8888 (318.83)	0.0042	3.8686 (320.49)	0.0001
15	3.9046 (317.53)	0.0036	3.9059 (317.43)	0.0045	3.8999 (317.91)	0.0000
16	3.9252 (315.87)	0.0038	3.9324 (315.29)	0.0014	3.9192 (316.35)	0.0007
17	3.9343 (315.14)	0.0011	3.9523 (313.70)	0.0089	3.9485 (314.01)	0.0016
18	3.9572 (313.31)	0.0017	4.0032 (309.71)	0.0111	3.9921 (310.58)	0.0010
19	3.9948 (310.37)	0.0001	4.0359 (307.20)	0.0015	3.9924 (310.55)	0.0108
20	4.0072 (309.41)	0.0028	4.0394 (306.94)	0.0047	4.0276 (307.83)	0.0006

Bibliography

[1] H. A. Kramers and W. Heisenberg. Über die Streuung von Strahlung durch Atome. *Zeitschrift fur Physik*, 31:681–708, February 1925.

[2] P. A. M. Dirac. The Quantum Theory of Dispersion. *Proceedings of the Royal Society of London Series A*, 114:710–728, May 1927.

[3] E. J. Heller. Quantum corrections to classical photodissociation models. *J. Chem. Phys.*, 68:2066–2075, 1978.

[4] D. J. Tannor and E. J. Heller. Polyatomic Raman scattering for general harmonic potentials. *J. Chem. Phys.*, 77(1):202–218, 1982.

[5] M. Schmitt and J. Popp. Raman spectroscopy at the beginning of the twentyfirst century. *J. Raman Spectrosc.*, 37(13):20–28, 2006.

[6] K. Xiong. UV Resonance Raman Spectroscopy: A Highly Sensitive, Selective and Fast Technique for Environmental Analysis. *Journal of Environmental Analytical Chemistry*, 02, 01 2014.

[7] E. G. Rodgers and W. L. Peticolas. Selective ultraviolet resonance Raman excitation of individual chromophores in nicotinamide adenine dinucleotide. *J. Raman Spectrosc.*, 9(6):372–375, 1980.

[8] M. J. Frisch, G. W. Trucks, H. B. Schlegel, G. E. Scuseria, M. A. Robb, J. R. Cheeseman, G. Scalmani, V. Barone, B. Mennucci, G. A. Petersson, H. Nakatsuji, M. Caricato, X. Li, H. P. Hratchian, A. F. Izmaylov, J. Bloino, G. Zheng, J. L. Sonnenberg, M. Hada, M. Ehara, K. Toyota, R. Fukuda, J. Hasegawa, M. Ishida, T. Nakajima, Y. Honda, O. Kitao, H. Nakai, T. Vreven, J. A. Montgomery, Jr., J. E. Peralta, F. Ogliaro, M. Bearpark, J. J. Heyd, E. Brothers, K. N. Kudin, V. N. Staroverov, R. Kobayashi, J. Normand, K. Raghavachari, A. Rendell, J. C. Burant, S. S. Iyengar, J. Tomasi, M. Cossi, N. Rega, J. M. Millam, M. Klene, J. E. Knox, J. B. Cross, V. Bakken, C. Adamo, J. Jaramillo, R. Gomperts, R. E. Stratmann, O. Yazyev, A. J. Austin, R. Cammi, C. Pomelli, J. W. Ochterski, R. L. Martin, K. Morokuma, V. G. Zakrzewski, G. A. Voth, P. Salvador, J. J. Dannenberg,

S. Dapprich, A. D. Daniels, Ö. Farkas, J. B. Foresman, J. V. Ortiz, J. Cioslowski, and D. J. Fox. Gaussian 09 Revision D.01. Gaussian Inc. Wallingford CT 2013.

[9] E. Schrödinger. An undulatory theory of the mechanics of atoms and molecules. *Phys. Rev.*, 28:1049–1070, Dec 1926.

[10] M. Born and R. Oppenheimer. Zur Quantentheorie der Molekeln. *Annalen der Physik*, 389(20):457–484.

[11] F. Jensen. *Introduction to Computational Chemistry*. Wiley, 2007.

[12] D. R. Hartree. The Wave Mechanics of an Atom with a non-Coulomb Central Field. Part III. Term Values and Intensities in Series in Optical Spectra. *Mathematical Proceedings of the Cambridge Philosophical Society*, 24(3):426–437, 1928.

[13] V. Fock. Näherungsmethode zur Lösung des quantenmechanischen Mehrkörperproblems. *Zeitschrift fur Physik*, 61:126–148, Jan 1930.

[14] A. Szabo and N. S. Ostlund. *Modern Quantum Chemistry: Introduction to Advanced Electronic Structure Theory*. Dover Books on Chemistry. Dover Publications, 1989.

[15] E. R. Davidson and D. Feller. Basis set selection for molecular calculations. *Chem. Rev.*, 86(4):681–696, 1986.

[16] J. C. Slater. Atomic shielding constants. *Phys. Rev.*, 36:57–64, Jul 1930.

[17] R. Ditchfield, W. J. Hehre, and J. A. Pople. SelfConsistent MolecularOrbital Methods. IX. An Extended GaussianType Basis for MolecularOrbital Studies of Organic Molecules. *J. Chem. Phys.*, 54(2):724–728, 1971.

[18] A. Schäfer, C. Huber, and R. Ahlrichs. Fully optimized contracted Gaussian basis sets of triple zeta valence quality for atoms Li to Kr. *J. Chem. Phys.*, 100:5829–5835, 1994.

[19] P. Hohenberg and W. Kohn. Inhomogeneous electron gas. *Phys. Rev.*, 136:B864–B871, Nov 1964.

[20] W. Kohn and L. J. Sham. Self-Consistent Equations Including Exchange and Correlation Effects. *Phys. Rev.*, 140:A1133–A1138, Nov 1965.

[21] J. P. Perdew and Y. Wang. Accurate and simple analytic representation of the electron-gas correlation energy. *Phys. Rev. B*, 45:13244–13249, Jun 1992.

[22] J. P. Perdew and W. Yue. Accurate and simple density functional for the electronic exchange energy: Generalized gradient approximation. *Phys. Rev. B*, 33:8800–8802, Jun 1986.

[23] A. D. Becke. Density-functional exchange-energy approximation with correct asymptotic behavior. *Phys. Rev. A*, 38:3098–3100, Sep 1988.

[24] S. H. Vosko, L. Wilk, and M. Nusair. Accurate spin-dependent electron liquid correlation energies for local spin density calculations: a critical analysis. *Can. J. Phys.*, 58:1200, Aug 1980.

[25] C. Lee, W. Yang, and R. G. Parr. Development of the Colle-Salvetti correlation-energy formula into a functional of the electron density. *Phys. Rev. B*, 37:785–789, Jan 1988.

[26] E. Runge and E. K. U. Gross. Density-Functional Theory for Time-Dependent Systems. *Phys. Rev. Lett.*, 52:997–1000, Mar 1984.

[27] M. Petersilka, U. J. Gossmann, and E. K. U. Gross. Excitation Energies from Time-Dependent Density-Functional Theory. *Phys. Rev. Lett.*, 76:1212–1215, Feb 1996.

[28] A. Dreuw and M. Head-Gordon. Single-Reference ab Initio Methods for the Calculation of Excited States of Large Molecules. *Chem. Rev.*, 105(11):4009–4037, 2005.

[29] S. Mertuš, E. Scrocco, and J. Tomasi. Electrostatic interaction of a solute with a continuum. A direct utilizaion of AB initio molecular potentials for the prevision of solvent effects. *Chemical Physics*, 55(1):117–129, 1981.

[30] R. Cammi, B. Mennucci, and J. Tomasi. Fast Evaluation of Geometries and Properties of Excited Molecules in Solution: A Tamm-Dancoff Model with Application to 4-Dimethylaminobenzonitrile. *J. Phys. Chem. A*, 104(23):5631–5637, 2000.

[31] M. Cossi and V. Barone. Time-dependent density functional theory for molecules in liquid solutions. *J. Chem. Phys.*, 115(10):4708–4714, 2001.

[32] R. Improta, V. Barone, G. Scalmani, and M. J. Frisch. A state-specific polarizable continuum model time dependent density functional method for excited state calculations in solution. *J. Chem. Phys.*, 125:054103:1–9, 2006.

[33] R. Improta, G. Scalmani, M. J. Frisch, and V. Barone. Toward effective and reliable fluorescence energies in solution by a new State Specific Polarizable Continuum Model Time Dependent Density Functional Theory Approach. *J. Chem. Phys.*, 127:074504:1–9, 2007.

[34] T. Petrenko and F. Neese. Analysis and prediction of absorption band shapes, fluorescence band shapes, resonance Raman intensities, and excitation profiles using the time-dependent theory of electronic spectroscopy. *J. Chem. Phys.*, 127(16):164319, 2007.

[35] J. W. Knight, X. P. Wang, L. Gallandi, O. Dolgounitcheva, X. G. Ren, J. V. Ortiz, P. Rinke, T. Körzdörfer, and N. Marom. Accurate Ionization Potentials and Electron Affinities of Acceptor Molecules III: A Benchmark of GW Methods. *J. Chem. Theor. Comput.*, 12(2):615–626, 2016.

[36] L. Hedin. New Method for Calculating the One-Particle Green's Function with Application to the Electron-Gas Problem. *Phys. Rev.*, 139:A796–A823, Aug 1965.

[37] M. S. Hybertsen and S. G. Louie. Electron correlation in semiconductors and insulators: Band gaps and quasiparticle energies. *Phys. Rev. B*, 34:5390–5413, Oct 1986.

[38] L. Gallandi, N. Marom, P. Rinke, and T. Körzdörfer. Accurate Ionization Potentials and Electron Affinities of Acceptor Molecules II: Non-Empirically Tuned Long-Range Corrected Hybrid Functionals. *J. Chem. Theor. Comput.*, 12(2):605–614, 2016.

[39] J. P. Perdew, K. Burke, and M. Ernzerhof. Generalized Gradient Approximation Made Simple. *Phys. Rev. Lett.*, 77:3865–3868, Oct 1996.

[40] J. Heyd, G. E. Scuseria, and M. Ernzerhof. Hybrid functionals based on a screened Coulomb potential. *J. Chem. Phys.*, 118(18):8207–8215, 2003.

[41] J. Heyd and G. E. Scuseria. Assessment and validation of a screened Coulomb hybrid density functional. *J. Chem. Phys.*, 120(16):7274–7280, 2004.

[42] J. F. Janak. Proof that $\frac{\partial E}{\partial n_i} = \epsilon$ in density-functional theory. *Phys. Rev. B*, 18:7165–7168, Dec 1978.

[43] J. P. Perdew, R. G. Parr, M. Levy, and J. L. Balduz. Density-Functional Theory for Fractional Particle Number: Derivative Discontinuities of the Energy. *Phys. Rev. Lett.*, 49:1691–1694, Dec 1982.

[44] T. H. Dunning. Gaussian basis sets for use in correlated molecular calculations. I. The atoms boron through neon and hydrogen. *J. Chem. Phys.*, 90:1007–1023, 1989.

[45] R. A. Kendall, T. H. Dunning Jr., and R. J. Harrison. Electron affinities of the first-row atoms revisited. Systematic basis sets and wave functions,. *J. Chem. Phys.*, 96:6796–6802, 1992.

[46] D. E. Woon and T. H. Dunning Jr. Gaussian-basis sets for use in correlated molecular calculations. 3. The atoms aluminum through argon. *J. Chem. Phys.*, 98:1358–1371, 1993.

[47] K. A. Peterson, D. E. Woon, and T. H. Dunning Jr. Benchmark calculations with correlated molecular wave functions. IV. The classical barrier height of the H+H_2 H_2+H reaction. *J. Chem. Phys.*, 100:7410–7415, 1994.

[48] A. K. Wilson, T. van Mourik, and T. H. Dunning Jr. Gaussian Basis Sets for use in Correlated Molecular Calculations. VI. Sextuple zeta correlation consistent basis sets for boron through neon. *J. Mol. Struct. (Theochem)*, 338:339–349, 1996.

[49] D. Feller, K. A. Peterson, and J. G. Hill. On the effectiveness of CCSD(T) complete basis set extrapolations for atomization energies. *J. Chem. Phys.*, 135(4):044102, 2011.

[50] A. J. C. Varandas. Extrapolating to the one-electron basis-set limit in electronic structure calculations. *J. Chem. Phys.*, 126(24):244105, 2007.

[51] F. Santoro. "FCclasses, a FORTRAN 77 code": please visit http://village.ipcf.cnr.it.

[52] Jörg Tatchen and Eli Pollak. Ab initio spectroscopy and photoinduced cooling of the trans-stilbene molecule. *J. Chem. Phys.*, 128(16):164303, 2008.

[53] T. Xiong, R. Włodarczyk, and P. Saalfrank. Accepted by *Chemical Physics*.

[54] D. Jariwala, V. K. Sangwan, L. J. Lauhon, T. J. Marks, and M. C. Hersam. Carbon nanomaterials for electronics, optoelectronics, photovoltaics, and sensing. *Chem. Soc. Rev.*, 42:2824–2860, 2013.

[55] Z. Iqbal, D. M. Ivory, J. Marti, J. L. Brédas, and R. H. Baughman. The Synthesis, Properties and Structure of Poly(Peri-Naphthalene): A Conducting, Undoped Organic Polymer. *Molecular Crystals and Liquid Crystals*, 118:103–109, 1985.

[56] J. L. Brédas and R. H. Baughman. Theoretical study of the electronic properties and crystal structure of poly(perinaphthalene): On the origin of high observed conductivities. *J. Chem. Phys.*, 83:1316–1322, 1985.

[57] J. Chen, J. J Zhang, Y. Zou, W. Xu, and D. Zhu. PPN (poly-peri-naphthalene) film as a narrow-bandgap organic thermoelectric material. *J. Mater. Chem. A*, 5:9891–9896, 2017.

[58] I. Deperasińska, D. T. Gryko, E. Karpiuk, B. Kozankiewicz, A. Makarewicz, and J. Piechowska. 12-Hydroxy-1-azaperylene-Limiting Case of the ESIPT System: Enol-Keto Tautomerization in S_0 and S_1 States. *J. Phys. Chem. A*, 116:2109–2116, 2012.

[59] L. Ryderfors, E. Mukhtar, and L. B.-Å. Johansson. Excited-State Symmetry and Reorientation Dynamics of Perylenes in Liquid Solutions: Time-Resolved Fluorescence Depolarization Studies Using One- and Two-Photon Excitation. *J. Phys. Chem. A*, 112:5794–5803, 2008.

[60] T. Sander, H.-G. Löhmannsröben, and H. Langhals. Photophysical and fluorescence quenching properties of 1,7-diazaperylene in solution. *J. Photochem. Photobiol. A: Chemistry*, 86:103 – 108, 1995.

[61] T. Brietzke, W. Mickler, A. Kelling, and H.-J. Holdt. Mono- and dinuclear ruthenium(II) 1,6,7,12-tetraazaperylene complexes. *Dalton Trans.*, 41:2788–2797, 2012.

[62] T. Hasobe, Keio University, Yokohama, Japan, private communication.

[63] T. Hasobe and coworkers, to be published.

[64] X. C. Wang, K. Maeda, A. Thomas, K. Takanabe, G. Xin, J. M. Carlsson, K. Domen, and M. Antonietti. A metal-free polymeric photocatalyst for hydrogen production from water under visible light. *Nat. Mater.*, 8:76–80, 2009.

[65] J. Wirth, R. Neumann, M. Antonietti, and P. Saalfrank. Adsorption and photocatalytic splitting of water on graphitic carbon nitride: a combined first principles and semiempirical study. *Phys. Chem. Chem. Phys.*, 16:15917–15926, 2014.

[66] K. Zenichowski, M. Gothe, and P. Saalfrank. Exciting flavins: Absorption spectra and spin-orbit coupling in light-oxygen-voltage (LOV) domains. *J. Photochem. Photobiol. A: Chemistry*, 190:290–300, 2007.

[67] S. Grimme, J. Antony, S. Ehrlich, and H. Krieg. A consistent and accurate ab initio parametrization of density functional dispersion correction (DFT-D) for the 94 elements H-Pu. *J. Chem. Phys.*, 132:154104:1–19, 2010.

[68] A. Camerman and J. Trotter. The Crystal and Molecular Structure of Perylene. *Proceedings of the Royal Society of London A: Mathematical, Physical and Engineering Sciences*, 279:129–146, 1964.

[69] M. J. G. Peach, E. I. Tellgren, P. Sałek, T. Helgaker, and D. J. Tozer. Structural and Electronic Properties of Polyacetylene and Polyyne from Hybrid and Coulomb-Attenuated Density Functionals. *J. Phys. Chem. A*, 111:11930–11935, 2007.

[70] R. Katoh, S. Sinha, S. Murata, and M. Tachiya. Origin of the stabilization energy of perylene excimer as studied by fluorescence and near-IR transient absorption spectroscopy. *J. Photochem. Photobiol. A: Chemistry*, 145:23 – 34, 2001.

[71] J. Ferguson. Absorption and Emission Spectra of the Perylene Dimer. *J. Chem. Phys.*, 44(7):2677–2683, 1966.

[72] R. E. Cook, B. T. Phelan, R. J. Kamire, M. B. Majewski, R. M. Young, and M. R. Wasielewski. Excimer Formation and Symmetry-Breaking Charge Transfer in Cofacial Perylene Dimers. *J. Phys. Chem. A*, 121:1607–1615, 2017.

[73] D. Casanova. Theoretical investigations of the perylene electronic structure: Monomer, dimers, and excimers. *Int. J. Quant. Chem.*, 115:442–452, 2015.

[74] A. S. Davydov. The Theory of Molecular Excitons. *Sov. Phys. Usp.*, 7:145–178, 1964.

[75] M. Kasha, H. R. Rawls, and M. A. El-Bayoumi. The Exciton Model in Molecular Spectroscopy. *Pure Appl. Chem.*, 11:371–392, 1965.

[76] J. C. Randel, F. C. Niestemski, A. R. Botello-Mendez, W. Mar, G. Ndabashimiye, S. Melinte, J. E. P. Dahl, R. M. K. Carlson, E. D. Butova, A. A. Fokin, P. R. Schreiner, J.-C. Charlier, and H. C. Manoharan. Unconventional molecule-resolved current rectification in diamondoidfullerene hybrids. *Nat. Commun.*, 5, 2014.

[77] R. Lemmerz, M. Nieger, and F. Vögtle. New highly strained adamantanophanes. *J. Chem. Soc., Chem. Commun.*, pages 1168–1170, 1993.

[78] P. Kahl, J. P. Wagner, C. Balestrieri, J. Becker, H. Hausmann, G. J. Bodwell, and P. R. Schreiner. [2](1,3)Adamantano[2](2,7)pyrenophane: A Hydrocarbon with a Large Dipole Moment. *Angew. Chem.*, 128(32):9423–9427.

[79] S. Banerjee and P. Saalfrank. Vibrationally resolved absorption, emission and resonance Raman spectra of diamondoids: a study based on time-dependent correlation functions. *Phys. Chem. Chem. Phys.*, 16:144–158, 2014.

[80] C. Tyborski, TU Berlin, Berlin, Germany, private communication.

[81] T. Xiong, R. Włodarczyk, L. Gallandi, T. Körzdörfer, and P. Saalfrank. Vibrationally resolved photoelectron spectra of lower diamondoids: A time-dependent approach. *J. Chem. Phys.*, 148(4):044310, 2018.

[82] R. C. Fort and P. v. R. Schleyer. Adamantane: Consequences of the Diamondoid Structure. *Chem. Rev.*, 64(3):277–300, 1964.

[83] J. E. Dahl, S. G. Liu, and R. M. K. Carlson. Isolation and Structure of Higher Diamondoids, Nanometer-Sized Diamond Molecules. *Science*, 299(5603):96–99, 2003.

[84] J. E. P. Dahl, J. M. Moldowan, Z. B. Wei, P. A. Lipton, P. Denisevich, R. Gat, S. G. Liu, P. R. Schreiner, and R. M. K. Carlson. Synthesis of Higher Diamondoids and Implications for Their Formation in Petroleum. *Angew. Chem. Int. Ed.*, 49(51):9881–9885, 2010.

[85] V. Z. Williams, P. von Ragué Schleyer, G. J. Gleicher, and L. B. Rodewald. Triamantane. *J. Am. Chem. Soc.*, 88(16):3862–3863, 1966.

[86] A. A. Fokin, E. D. Butova, L. V. Chernish, N. A. Fokina, J. E. P. Dahl, R. M. K. Carlson, and P. R. Schreiner. Simple Preparation of Diamondoid 1,3-Dienes via Oxetane Ring Opening. *Org. Lett.*, 9(13):2541–2544, 2007.

[87] H. Schwertfeger, C. Würtele, M. Serafin, H. Hausmann, R. M. K. Carlson, J. E. P. Dahl, and P. R. Schreiner. Monoprotection of Diols as a Key Step for the Selective Synthesis of Unequally Disubstituted Diamondoids (Nanodiamonds). *J. Org. Chem.*, 73(19):7789–7792, 2008.

[88] A. A. Fokin and P. R. Schreiner. Selective Alkane Transformations via Radicals and Radical Cations: Insights into the Activation Step from Experiment and Theory. *Chem. Rev.*, 102(5):1551–1594, 2002.

[89] H. Schwertfeger, A. A. Fokin, and P. R. Schreiner. Diamonds are a Chemist's Best Friend: Diamondoid Chemistry Beyond Adamantane. *Angew. Chem. Int. Ed.*, 47(6):1022–1036, 2008.

[90] W. L. Yang, J. D. Fabbri, T. M. Willey, J. R. I. Lee, J. E. Dahl, R. M. K. Carlson, P. R. Schreiner, A. A. Fokin, B. A. Tkachenko, N. A. Fokina, W. Meevasana, N. Mannella, K. Tanaka, X. J. Zhou, T. van Buuren, M. A. Kelly, Z. Hussain, N. A.

Melosh, and Z.-X. Shen. Monochromatic Electron Photoemission from Diamondoid Monolayers. *Science*, 316(5830):1460–1462, 2007.

[91] L. Landt, K. Klünder, J. E. Dahl, R. M. K. Carlson, T. Möller, and C. Bostedt. Optical Response of Diamond Nanocrystals as a Function of Particle Size, Shape, and Symmetry. *Phys. Rev. Lett.*, 103:047402, Jul 2009.

[92] R. Richter, M. I. S. Röhr, T. Zimmermann, J. Petersen, C. Heidrich, R. Rahner, T. Möller, J. E. Dahl, R. M. K. Carlson, R. Mitric, T. Rander, and A. Merli. Laser-induced fluorescence of free diamondoid molecules. *Phys. Chem. Chem. Phys.*, 17:4739–4749, 2015.

[93] L. Landt, W. Kielich, D. Wolter, M. Staiger, A. Ehresmann, T. Möller, and C. Bostedt. Intrinsic photoluminescence of adamantane in the ultraviolet spectral region. *Phys. Rev. B*, 80:205323, Nov 2009.

[94] M. Steglich, F. Huisken, J. E. Dahl, R. M. K. Carlson, and Th. Henning. Electronic Spectroscopy of FUV-irradiated Diamondoids: A Combined Experimental and Theoretical Study. *Astrophys. J.*, 729(2):91, 2011.

[95] S. Banerjee, T. Stüker, and P. Saalfrank. Vibrationally resolved optical spectra of modified diamondoids obtained from time-dependent correlation function methods. *Phys. Chem. Chem. Phys.*, 17:19656–19669, 2015.

[96] W. Schmidt. Photoelectron spectra of diamondoid molecules. *Tetrahedron*, 29(14):2129 – 2134, 1973.

[97] T. Zimmermann, R. Richter, A. Knecht, A. A. Fokin, T. V. Koso, L. V. Chernish, P. A. Gunchenko, P. R. Schreiner, T. Möller, and T. Rander. Exploring covalently bonded diamondoid particles with valence photoelectron spectroscopy. *J. Chem. Phys.*, 139(8):084310, 2013.

[98] A. Gali, T. Demjn, M. Vörös, G. Thiering, E. Cannuccia, and A. Marini. Electron-vibration coupling induced renormalization in the photoemission spectrum of diamondoids. *Nat. Commun.*, 7:11327, 2016.

[99] S. Banerjee, D. Kröner, and P. Saalfrank. Resonance Raman and vibronic absorption spectra with Duschinsky rotation from a time-dependent perspective: Application to β-carotene. *J. Chem. Phys.*, 137:22A534:1–9, 2012.

[100] H. Yin, Y. Ma, X. Hao, J. Mu, C. Liu, and Z. Yi. Quasiparticle electronic structure and optical absorption of diamond nanoparticles from ab initio many-body perturbation theory. *J. Chem. Phys.*, 140:214315–1–5, 2014.

[101] T. Demján, M. Vörvös, M. Palummo, and A. Gali. Electronic and optical properties of pure and modified diamondoids studied by many-body perturbation theory and time-dependent density functional theory. *J. Chem. Phys.*, 141:064308, 2014.

[102] V. Blum, R. Gehrke, F. Hanke, P. Havu, V. Havu, X. G. Ren, K. Reuter, and M. Scheffler. Ab initio molecular simulations with numeric atom-centered orbitals. *Comput. Phys. Commun.*, 180(11):2175–2196, 2009.

[103] W. Nowacki and K. W. Hedberg. An Electron Diffraction Investigation of the Structure of Adamantane. *J. Am. Chem. Soc.*, 70(4):1497–1500, 1948.

[104] A. Patzer, M. Schütz, T. Möller, and O. Dopfer. Infrared Spectrum and Structure of the Adamantane Cation: Direct Evidence for Jahn−Teller Distortion. *Angew. Chem. Int. Ed.*, 51(20):4925–4929, 2012.

[105] A. A. Fokin, B. A. Tkachenko, P. A. Gunchenko, D. V. Gusev, and P. R. Schreiner. Functionalized Nanodiamonds Part I. An Experimental Assessment of Diamantane and Computational Predictions for Higher Diamondoids. *Chem. Eur. J.*, 11(23):7091–7101, 2005.

[106] F. S. Jørgensen and J. P. Snyder. Search for a trans-disulfide: Structural analysis of di-tert-adamantyl disulfide by photoelectron spectroscopy. *J. Org. Chem.*, 45:1015–1020, 1980.

[107] A. Schäfer, H. Horn, and R. Ahlrichs. Fully Optimized Contracted Gaussian Basis Sets for Atoms Li to Kr. *J. Chem. Phys.*, 97:2571–2577, 1992.

[108] J. M. L. Martin. Ab initio total atomization energies of small molecules - towards the basis set limit. *Chem. Phys. Lett.*, 259:669–678, 1996.

[109] X. Blase, C. Attaccalite, and V. Olevano. First-principles GW calculations for fullerenes, porphyrins, phtalocyanine, and other molecules of interest for organic photovoltaic applications. *Phys. Rev. B*, 83:115103, Mar 2011.

[110] C. Faber, C. Attaccalite, V. Olevano, E. Runge, and X. Blase. First-principles GW calculations for DNA and RNA nucleobases. *Phys. Rev. B*, 83:115123, Mar 2011.

[111] N. Marom, F. Caruso, X. G. Ren, O. T. Hofmann, T. Körzdörfer, J. R. Chelikowsky, A. Rubio, M. Scheffler, and P. Rinke. Benchmark of GW methods for azabenzenes. *Phys. Rev. B*, 86:245127, Dec 2012.

[112] T. Körzdörfer and N. Marom. Strategy for finding a reliable starting point for G_0W_0 demonstrated for molecules. *Phys. Rev. B*, 86:041110, Jul 2012.

[113] F. Bruneval and M. A. L. Marques. Benchmarking the Starting Points of the GW Approximation for Molecules. *J. Chem. Theor. Comput.*, 9(1):324–329, 2013.

[114] M. van Schilfgaarde, T. Kotani, and S. Faleev. Quasiparticle Self-Consistent GW Theory. *Phys. Rev. Lett.*, 96:226402, Jun 2006.

[115] G. Yan, N. R. Brinkmann, and H. F. Schaefer. Energetics and Structures of Adamantane and the 1- and 2-Adamantyl Radicals, Cations, and Anions. *J. Phys. Chem. A*, 107(44):9479–9485, 2003.

[116] G. H. Kruppa and J. L. Beauchamp. Energetics and structure of the 1- and 2-adamantyl radicals and their corresponding carbonium ions by photoelectron spectroscopy. *J. Am. Chem. Soc.*, 108(9):2162–2169, 1986.

[117] M. Etinski, J. Tatchen, and C. M. Marian. Time-dependent approaches for the calculation of intersystem crossing rates. *J. Chem. Phys.*, 134(15):154105, 2011.

[118] Y. L. Niu, Q. Peng, C. M. Deng, X. Gao, and Z. G. Shuai. Theory of Excited State Decays and Optical Spectra: Application to Polyatomic Molecules. *J. Phys. Chem. A*, 114(30):7817–7831, 2010.

Erklärung

Hiermit versichere ich, dass die vorliegende Arbeit an keiner anderen Hochschule eingereicht sowie selbständig und ausschließlich mit den angegebenen Mitteln angefertigt worden ist.

Potsdam, June 2018